

ABSTRACT

Title of Dissertation: GEOCHEMICAL REACTION MODELING
OF CARBON DIOXIDE: THEORY

Mohammad Alizadeh Nomeli
Doctor of Philosophy, 2014

Thesis directed by: Dr. Amir Riaz
Department of Mechanical Engineering

Recently, the need to decrease CO₂ concentration in the atmosphere has been recognized because of the role of CO₂ as a greenhouse gas that contributes to global warming. Carbon Capture and Sequestration (CCS) is one of the most promising long term solutions for the reduction of CO₂ in the atmosphere. To this end, injection of CO₂ into saline aquifers has been proposed and investigated theoretically and experimentally in the last years. Modeling the storage of CO₂ in saline aquifers on a reservoir scale is very demanding with respect to computational cost. Long-term subsurface storage of CO₂ in saline aquifers may induce a range of chemical processes in response to disturbances in existing chemical equilibria that include, but are not limited to, dissolution of primary minerals and precipitation of secondary carbonates. CCS projects also can be done above the ground by injecting CO₂ into designated fractures. The work presented in this thesis focuses on developing a fundamental understanding and modeling approach for 3 basic aspects of sequestration: 1) the effect of CO₂ solubility on rates of geochemical reactions, 2) density of

brine after dissolution of CO₂, and 3) time dependent porosity variation of a single fracture due to precipitation of carbonates.

A new method is developed to determine the reaction rates of minerals, on the basis of transition state theory, in saline aquifers containing brine and a supercritical CO₂ phase. A general Arrhenius-type equation that depends explicitly on the pH of brine is employed to determine the reaction rates. The dependence of pH on the amount of aqueous CO₂ dissolved in brine is modeled in this study. An accurate pressure-volume-temperature-composition (PVTx) model is employed to determine the dissolution of supercritical CO₂ in brine for the temperature range of 50-100°C and pressures up to 600 bar. Solubility of CO₂ and dissolution rate of calcite predicted by the model are validated with experimental data available in the literature for specific thermodynamic and salinity conditions. The effects of CO₂ activity on pH and reaction rates are evaluated by means of four different models for the activity coefficient of dissolved CO₂. The results indicate that dissolution of CO₂ decreases the pH of the system but an increase in the temperature and salinity values limits the pH reduction. The rates of reactions are found to increase with pressure and temperature. The results suggest that among the available mineral compositions in deep saline aquifers, the dissolution rate of anorthite is the rate limiting factor. The significance of the pre-exponential factor and the reaction order associated with the modified Arrhenius equation is evaluated to determine the sensitivity of the reaction rates as a function of the system pH. We find that the transition state theory can reasonably reproduce experimental data with new parameters that we are obtained in this study on the basis of sensitivity analysis. Finally, we develop a long-term

geochemical modeling of CO₂ storage on a designated fracture above the ground to investigate the impacts of temperature, pressure, and salinity on the reaction rates and, subsequently, the critical time of blockage due to precipitation of carbonates.

With regards to the second focus of this thesis, the effect of CO₂ solubility on the density of binary H₂O-CO₂ and ternary H₂O-CO₂-NaCl solutions in saline aquifers is investigated. These solution densities as dispensable properties play pivotal roles in estimating the dynamic evolution of plume containing aqueous CO₂ and brine and also affect fracture dynamics in geologic media. An improved model is proposed to predict the density of saturated binary and ternary solutions as a function of pressure, temperature, and salinity. The model is based on an extended form of the Redlich-Kwong Equation of State that yields more representative values of the molar volumes of liquid CO₂. The extension involves finding new coefficients for the cubic Redlich-Kwong equation to match one of the solutions with the liquid molar volume deduced from experimentally measured density of binary solutions. The new coefficients are constrained to ensure that the solution branch corresponding to the molar volume in the gas phase remains unchanged. Due to variability in the experimentally measured density of binary solutions, an effective liquid molar volume is obtained with the help of a multi-parameter non-linear regression with respect to pressure and temperature. The proposed model is validated by comparing it with experimental data and is used to study the density-pressure-temperature-salinity relationship. It is found that the density of the saturated solution is proportional to the mole fraction of dissolved CO₂. In general, solution density is found to increase with pressure but decreases with an increase in temperature within the range of

50-100°C. It is also found that the solution density decreases monotonically with an increase in salinity.

Finally, a new model is presented to simulate a reactive fluid within a fracture. Permeability of a fracture controls the path of aqueous CO₂ migration, therefore aperture width of a fracture has a pivotal effect on solubility and mineral trapping of injected CO₂. This study investigates the impact of the formation of precipitates within fractures on CO₂ transport and storage capacity. The problem involves the flow of CO₂ between finite walls that represents a single fracture. Fluid convection, diffusion, and chemical reactions inside a finite space are solved as a simplified representation of natural mineral trapping. The model is composed of direct numerical simulation of incompressible flow and transport combined with the kinetics of corresponding chemical reactions. For each time step, transport and reactions are solved by means of a finite difference method using a sequential non-iterative approach. The purpose of the current study is to show the time evolution of the aperture shrinkage caused by precipitation of calcite. The current model predicts the actual efficiency of the mineral trapping mechanism by considering the physical properties of the fluid such as its density, pH, and the characteristics of the mineral compositions. It is found that for low Peclet numbers ($Pe \leq 100$), the critical time for a fracture blockage is insensitive to the Reynolds number and increases with the Peclet number. At a high Peclet number $Pe = 1000$, however, the critical time generally decreases with increasing Reynolds number.

REACTIVE TRANSPORT MODELING OF CARBON
DIOXIDE, CO₂, IN GEOLOGICAL FORMATIONS:
THEORY

by

Mohammad Alizadeh Nomeli

Dissertation submitted to the Faculty of the Graduate School of the
University of Maryland, College Park in partial fulfillment
of the requirements for the degree of
Doctor of Philosophy
2014

Advisory Committee:

Professor. Amir Riaz, Chair

Professor Philip A. Candela, Dean's representative

Professor Reinhard Radermacher

Professor Jeff Klauda

Professor Bao Yang

© Copyright by
Mohammad Alizadeh Nomeli
2014

Preface

The field of carbon dioxide sequestration within the Earth Sciences is a highly multidisciplinary area of research. The field encompasses a number of diverse disciplines including fluid mechanics, geochemistry, geology, physics, chemistry, hydrology, civil and environmental engineering. This is an attempt to some extent to bridge the gap between these different disciplines by bringing together ideas from different backgrounds. The systems including injected CO₂ can be viewed as open geochemical reactors where chemical change is driven by the interactions between migrating fluids, aqueous species and solid phases. The evolution of these systems involves diverse processes including thermodynamics, fluid flow, chemical reaction, and mass transport, each with differing characteristic time scales. This study focuses on methods to describe the extend and consequences of reactive flow and transport in a designated systems after injection of CO₂ which is also useful for general reactive transport in subsurface environments.

Foreword

I strongly commit to make the world a better place to live.

Dedication

I dedicate this dissertation to my wonderful family and all people around the world.

Acknowledgments

First and foremost, I would like to thank God, whose many blessings have made me who I am today.

I would like to express my sincere gratitude to my advisor, Dr. Amir Riaz for giving me an invaluable opportunity to work on challenging and extremely interesting projects over the past few years. He has always made himself available for help and advice and there has never been an occasion when I would knocked on his door and he hasn't given me time. It has been a pleasure to work with and learn from such an extraordinary individual. I am thankful for his continuous substantial advice and patience while supervising the gradual progress of this dissertation.

I owe my deepest thanks to my family who have always stood by my side and guided me through my career, and have pulled me through against impossible odds at times. Words cannot express the gratitude I owe them.

I wish to thank my wife Arezoo for her love, patience, support and faith in me.

I would also like to thank Professor Hamdi Tchelepi and Professor Gregory Jackson. Without their extraordinary supports, this dissertation would have been a distant dream. Thanks are due to Professor Philip A. Candela, Jeff Klauda, Reinhard Radermacher and Bao Yang for agreeing to serve on my thesis committee and for sparing their invaluable time reviewing the manuscript.

My colleagues, Don Daniel, Nils Tilton, Zhipeng Qin and Moon Soo Lee, have enriched my graduate life in many ways and deserve a special mention.

I am indebted to numerous people for their continuous support. I am very grateful to my friends for ideas, energy, criticism, advice, support and forgiveness. Their love keeps me going. It is impossible to remember all, and I apologize to those I've inadvertently left out.

I could not have completed my research without the support of all these wonderful people!

Lastly, thank you all.

Table of Contents

| | |
|---|-----|
| List of Tables | ix |
| List of Figures | x |
| List of Abbreviations | xiv |
| 1 Introduction | 1 |
| 1.1 Solubility and Kinetics | 2 |
| 1.2 Density | 8 |
| 1.3 Reactive Transport Modeling | 10 |
| 1.4 The outline of the study | 13 |
| 2 Problem Statement | 15 |
| 3 Effect of CO ₂ Solubility on the Dissolution Rates of Minerals in Saline Aquifers for the Temperature Range of 50-100°C and Pressures up to 600 Bar | 25 |
| 3.1 Introduction | 25 |
| 3.2 Model description | 30 |
| 3.3 Sensitivity analysis | 35 |
| 3.4 Conclusions | 43 |
| 4 Effect of CO ₂ Solubility on the Density of CO ₂ -H ₂ O and CO ₂ -H ₂ O-NaCl Solutions in Saline Aquifers | 45 |
| 4.1 Introduction | 45 |
| 4.2 Modeling approach | 50 |
| 4.3 Molar volume of H ₂ O and density ratio | 55 |
| 4.4 Saturated mole fraction of dissolved CO ₂ | 58 |
| 4.5 Partial molar volume of CO ₂ in saturated solutions | 61 |
| 4.6 Modified Redlich-Kwong EOS | 63 |
| 4.7 Density of ternary solutions | 66 |
| 4.8 Onset of buoyancy driven convection | 72 |
| 4.9 Conclusion | 80 |
| 5 Fracture simulation | 83 |
| 5.1 Introduction | 83 |
| 5.2 Model Description | 90 |
| 5.3 Reactive transport in a fracture | 97 |
| 5.3.1 Governing equations for flow and transport | 97 |
| 5.3.2 Governing equations for the growth rate of calcite | 101 |
| 5.3.3 Dimensionless critical time of blockage t_c for the fracture | 105 |
| 5.4 Conclusion | 115 |

| | | |
|-----|---|-----|
| 6 | Conclusions and future work | 117 |
| 6.1 | Conclusions | 117 |
| 6.2 | Future work | 121 |
| 7 | Appendix | 125 |
| A.1 | Solubility of CO ₂ as a function of pressure, temperature and salinity . | 125 |
| B.1 | Dependence of pH on pressure, temperature and salinity | 130 |

List of Tables

| | | |
|-----|--|-----|
| 2.1 | Experimental studies performed to determine the density of the CO ₂ -H ₂ O solution. The last column gives the range of concentrations, as mole fraction $x(\text{CO}_2)$, at which the density was determined. | 21 |
| 3.1 | Coefficients in Equation 3.12 | 39 |
| 4.1 | Coefficients in Equation 4.3 | 51 |
| 4.2 | Experimental studies performed to determine the density of the CO ₂ -H ₂ O solution. The last column gives the range of concentrations, as mole fraction $x(\text{CO}_2)$, at which the density was determined. | 52 |
| 4.3 | Residual sum of squares, RSS | 53 |
| 4.4 | Coefficients in Equation 4.10. | 63 |
| 4.5 | Coefficients in Equation 4.13 | 66 |
| 4.6 | Characteristics of CO ₂ injection into saline aquifers in western Canada. | 80 |
| 5.1 | Formal description of calcite structure. | 101 |
| 5.2 | Volumetric thermal expansion coefficients of carbonate minerals. | 103 |
| 5.3 | The effects of temperature, pressure and salinity on Damköhler and critical time of blockage t_c when $\text{Re} = 10$ and $\text{Pe} = 1000$ | 106 |
| 5.4 | Physical properties of a single fracture in Figure 5.6. | 107 |
| 5.5 | Physical properties of the single fracture in Figure 5.7. | 109 |
| 5.6 | The effects of temperature, pressure and salinity on Damköhler and critical time of blockage t_c | 113 |
| 1 | Values of the coefficients used in the Redlich-Kwong equation. | 128 |

List of Figures

| | | |
|-----|--|----|
| 2.1 | Schematic diagram illustrating the residual trapping of supercritical CO ₂ | 16 |
| 2.2 | Schematic diagram illustrating a CO ₂ injection site consisting of a saline aquifer. After injection CO ₂ spreads through the reservoir, displacing reservoir brine. | 18 |
| 2.3 | Dissolution of CO ₂ into saline formation at the interface. | 20 |
| 3.1 | Log of dissolution rate of calcite in pure water (m=0) computed at 25°C as a function pH: Comparison of the results for different reaction orders (solid lines $n=1$, $n=1.125$, $n=1.3$) with respect to the pH and experimental data (symbols). | 36 |
| 3.2 | (a) Calculated dissolution rate of calcite with pressure based on different reaction order values in pure water (m=0) computed at 50°C. (b) Calculated log of dissolution rate of calcite with respect to reaction order, n , in saline water computed at various values of the molality of NaCl, m , T= 50°C, P= 100 bar. The dissolution rates of calcite are found to decrease for higher value of reaction order and salinity. . | 38 |
| 3.3 | Calculated dissolution rate of calcite with pressure based on various activity coefficient models; Duan and Sun (2003) (solid lines), Rumpf et al. (1994) (crosses), Fournier (1985) (diamonds), Drummond (1981) (triangle) in saline water computed at (a) T= 50°C and pressures up to 600 bar, (b) P= 100 bar, various temperatures and molality of NaCl, m | 40 |
| 3.4 | Calculated dissolution rate of anorthite with pressure based on various activity coefficient models; Duan and Sun (2003) (solid lines), Rumpf et al. (1994) (crosses), Fournier (1985) (diamonds), Drummond (1981) (triangle) in saline water computed at (a) T= 50°C and pressures up to 600 bar, (b) P= 100 bar, various temperatures and molality of NaCl, m | 41 |
| 3.5 | Calculated dissolution rate of calcite from Eq. 3.12 with pressure and temperature based on activity coefficient model of Duan and Sun (2003) in (a) pure water, (b) saline water with molality of NaCl, $m=3$ | 42 |
| 3.6 | Calculated dissolution rate of anorthite from Eq. 3.12 with pressure and temperature based on activity coefficient model of Duan and Sun (2003) in (a) pure water, (b) saline water with molality of NaCl, $m=3$. | 43 |

| | | |
|-----|---|----|
| 4.1 | Experimental data for ρ_B reported by Teng et al. (1997) (crosses), Bando et al. (2004) (triangles), Song et al. (2005) (diamonds) and Li et al. (2011) (solid dots) for the temperatures (a) 25°C and (b) 65°C. Solid lines show ρ_B obtained from Eq. (4.3). Results from the model of Duan et al. (2008) are shown in panel (b) using a dash-dotted line. The dashed line in panel (b) shows our results obtained with linear regression. | 54 |
| 4.2 | (a) Density of pure water at T=65°C based on the EOS model of Kell (1975) (solid line) that is used in the current study. Density values reported by Li et al. (2004) and those recommended by NIST are shown with symbols, (diamonds) and (triangles), respectively. (b) Variation of H ₂ O density with temperature based on the EOS of Kell (1975) | 55 |
| 4.3 | (a) Relative density difference, $(\rho_B/\rho_1 - 1)$, as a function of pressure at 65°C. Lines indicate the relative density computed from the non-linear regression Eq. (4.3) (solid line), linear regression (dashed line) and the model of Duan et al. (2008) (dash-dotted line). Symbols represent $(\rho_B/\rho_1 - 1)$ based on the experimental data of Teng et al. (1997) (crosses), Bando et al. (2004) (triangles), Song et al. (2005) (diamonds) and Li et al. (2011) (circles). The density of pure water, ρ_1 , is based on the EOS of Kell (1975). (b) ρ_B based on the non-linear regression (solid line) and the model of Duan et al. (2008) (dash-dotted line) as a function of temperature at 150 bar. | 57 |
| 4.4 | (a) Density of the saturated binary solution, ρ_B , as a function of saturated mole fraction of dissolved CO ₂ . Symbols denote liquid molar volume based on experimental data for density noted in Fig. 4.1. The solid squares on the constant temperature lines correspond to the maximum mole fraction of CO ₂ at 600 bar. (b) Relative density of the saturated binary solution, ρ_B , with respect to the density of pure water, ρ_1 | 58 |
| 4.5 | (a) Partial molar volume of dissolved CO ₂ in the liquid phase | 61 |
| 4.6 | (a) Mole fraction of dissolved CO ₂ as a function of pressure at 100°C. The residual sum of squares of the difference between experimental data points and x_2 is 6.811×10^{-6} . The mole fraction x_2 , obtained from the modified Redlich-Kwong EOS agrees well with experimental data for saturated binary solutions. (b) The relationship between gas and liquid molar volumes as a function of temperature and pressure predicted by the modified Redlich-Kwong EOS. | 65 |
| 4.7 | Density of ternary solution ρ_T at (a) 60°C and (b) 100 bar for two different values of NaCl molality. Our calculations of ρ_T are based on the activity coefficient models of Duan and Sun (2003) (line), Fournier (1985) (diamonds), and Drummond (1981) (crosses), Rumpf et al. (1994) (triangles). We compare our calculations of ρ_T with data of Song et al. (2013) (squares), Akinfiev and Diamond (2010) (circles), and Li et al. (2011) (dashed lines). | 67 |

| | | |
|------|--|-----|
| 4.8 | The density ρ_T of a ternary solution as a function of NaCl molality for the constant temperature 50°C and pressure (a) 100 bar and (b) 600 bar. The symbols show the influence of different models for the activity coefficient: Duan and Sun (2003) (solid line), Fournier (1985) (diamonds), Drummond (1981) (crosses), and Rumpf et al. (1994) (triangles). | 68 |
| 4.9 | (a) Relative density difference between ρ_T and the density ρ_{ws} of H ₂ O-NaCl solutions at (a) 60°C and (b) 100 bar. Our calculations of $(\rho_T/\rho_{ws} - 1)$ are based on the activity coefficient models noted in Fig. 4.7. | 70 |
| 4.10 | (a) Density of ternary solutions and (b) the relative density difference as a function of mole fraction. Our calculations are based on the activity coefficient models noted in Fig. 4.7. | 71 |
| 4.11 | (a) Sketch (not to scale) of the homogeneous isotropic aquifer considered in Section 4.8. A layer of supercritical CO ₂ is situated below the upper cap rock and above the brine. Dissolution of CO ₂ forms a region of dense CO ₂ -rich brine (shaded dark gray) near $z = 0$. (b) The dashed line shows the temporal evolution of the flux j_d/J produced by the purely diffusive solution (4.15). The solid line shows the corresponding flux j/J produced a direct numerical simulation of buoyancy-driven convection (see Tilton and Riaz (2014) for details). The DNS was performed using the initial condition described in Eqs. 4.13–4.15 of Tilton and Riaz (2014) for ϵ^* . The solid dot shows the onset time of buoyancy-driven convection. | 73 |
| 4.12 | Onset time of buoyancy-driven convection t_{on} for H ₂ O-CO ₂ solutions, $m = 0$, as a function of (a) pressure when $T = 50$ (solid line) and 100°C (dashed line) and (b) temperature when $P = 100$ (solid line) and 600 bar (dashed line). | 76 |
| 4.13 | (a) The relationship between t_{on} and x_{CO_2} as a function of temperature and pressure, for salinities (a) $m = 0$ and (b) $m = 3$ | 77 |
| 4.14 | Wavelength λ_{on} for H ₂ O-CO ₂ solutions, $m = 0$, as a function of (a) pressure when $T = 50$ (solid line) and 100°C (dashed line) and (b) temperature when $P = 100$ (solid line) and 600 bar (dashed line). | 78 |
| 4.15 | (a) The relationship between λ_{on} and x_{CO_2} as a function of temperature and pressure for permeability, $\kappa = 10^{-12}$, and salinity values of (a) $m = 0$, (b) $m = 3$ | 79 |
| 5.1 | Schematic diagram illustrating the use of CO ₂ injection to Enhance Oil Recovery (EOR). | 84 |
| 5.2 | Schematic picture of precipitation and dissolution reaction in a single fracture. | 91 |
| 5.3 | Cell-centered finite difference discretization scheme in two dimensions. | 95 |
| 5.4 | The production of precipitates on the surface of the original solid phase. η points in a direction normal to the surface of the solid phase. | 102 |

| | | |
|-----|--|-----|
| 5.5 | Normalized u-component of the velocity vector, \mathbf{u} , for the entire grid inside the domain and also as a function of y for a few values of fixed x when (a) $t = 3.171$, (b) $t = 6.342$, (c) $t = 9.512$, and (d) $t = 12.683$. | 104 |
| 5.6 | Normalized concentration of the reactive component, aqueous species of dissolved CO_2 , with the streamlines at Reynolds number=10 and Peclet number=1000 inside a fracture blockage with smooth walls (b) $t_c = 5.437$, when $T = 50^\circ\text{C}$, $P = 200$, $m = 0$, $\text{Da} = 1.75 \times 10^{-2}$, (c) $t_c = 5.174$, when $T = 100^\circ\text{C}$, $P = 200$, $m = 0$, $\text{Da} = 4.20 \times 10^{-2}$. | 108 |
| 5.7 | Normalized concentration of the reactive component, aqueous species of dissolved CO_2 , inside the fracture with the streamlines when (b) $\text{Re}=10$, $\text{Pe}=10$, (c) $\text{Re}=10$, $\text{Pe}=1000$, (d) $\text{Re}=50$, $\text{Pe}=10$. $t = 0.81$ for (a), $t = 2.42$ for (b), (c) and, (d). | 110 |
| 5.8 | Critical time of blockage for the single fracture with pressure and temperature based on activity coefficient model of Duan and Sun (2003) in (a) pure water, $m=0$, (b) saline water with molality of NaCl , $m=5.8424$. | 111 |
| 5.9 | Critical times for a fracture blockage with smooth walls with respect to the changes in dimensionless numbers (a) $T = 50^\circ\text{C}$, $P = 100$, $m = 1$, $\text{Da} = 1.70 \times 10^{-2}$, (b) $T = 50^\circ\text{C}$, $P = 100$, $m = 3$, $\text{Da} = 1.67 \times 10^{-2}$ (c) $T = 50^\circ\text{C}$, $P = 400$, $m = 1$, $\text{Da} = 1.97 \times 10^{-2}$ (d) $T = 100^\circ\text{C}$, $P = 100$, $m = 1$, $\text{Da} = 3.87 \times 10^{-2}$. | 114 |
| 6.1 | Schematic representation of mineral trapping of CO_2 inside a porous media. | 122 |
| 1 | Activity coefficients for aqueous CO_2 at 1 bar pressure from various sources for 1 and 3 mol/kg NaCl aqueous solutions in the temperature range of $50\text{-}100^\circ\text{C}$. Activity coefficient of CO_2 increases with molality of NaCl , m , and decreases with temperature. | 126 |
| 2 | The calculated values of mole fraction of CO_2 by means of Eq. 2 based on various activity coefficient models; Duan and Sun (2003) (solid lines), Rumpf et al. (1994) (crosses), Fournier (1985) (diamonds), Drummond (1981) (triangle). (a) $T= 50^\circ\text{C}$ and (b) $P= 100$ bar. The solubility of CO_2 increases with pressure. Higher temperature and salinity values lower solubility. | 129 |
| 3 | The pH variation of binary solution, $\text{H}_2\text{O}\text{-CO}_2$, for different values of salinity based on various activity coefficient models; Duan and Sun (2003) (solid lines), Rumpf et al. (1994) (crosses), Fournier (1985) (diamonds), Drummond (1981) (triangle). Experimental data of Toews et al. (1995) for $m = 0$ is shown with circles. (a) $T= 50^\circ\text{C}$ and (b) $P= 100$ bar. | 131 |

List of Abbreviations: The following table shows the significant symbols used in this work. Local notations are explained in the text.

| | |
|---|--|
| CO ₂ | Carbon Dioxide |
| P | Pressure |
| f | Fugacity |
| ϕ | Fugacity coefficient |
| T | Temperature |
| SC | Super Critical |
| k | Reaction rate |
| ε | Error |
| SI | Saturation Index |
| u | Velocity vector |
| v | The molar volume |
| α | The experimental thermal expansion |
| NIST | National Institute of Standards and Technology |
| IAPWS | International Association for the Properties of Water and Steam |
| pH | The pH scale measures how acidic or basic a substance is |
| PD | Precipitation/Dissolution |
| A | Pre-exponential factor |
| R | Universal gas constant |
| E | Arrhenius activation energy (kJ mole ⁻¹) |
| n | The reaction order with respect to the concentration [H ⁺] |
| K _(a1) and K _(a2) | The first and the second dissociation constants, respectively |
| K _{eq} | The equilibrium constant |
| ΔH | The enthalpy of the reaction |
| ρ | The density of the solution |
| x_i | The mole fraction of the pure component i |
| M _{i} | Molar mass of the pure component i |
| V _{i} | Molar volume of the pure component i |
| m | The molality of NaCl |
| Q and S | The correcting factors |
| D | Diffusion coefficient |
| C _{i} | Concentration of a component i |
| V | Arbitrary volume |
| J _{i} | Solute flux of the i th species |
| R _{i} | Chemical reaction rates |
| t_{on} | the onset time of buoyancy-driven convection |
| λ_{on} | The wavelength |
| t_c | The critical time of blockage |
| Mw | Molecular weight |
| U | Characteristic velocity |
| H | Aperture width |
| Pe | Peclet number |
| Da | Damköhler number |
| Re | Reynolds number |
| CFL | Courant-Friedriches-Lewy |

Chapter 1

Introduction

It has been widely recognized that a significant reduction of current CO₂ emissions is necessary to maintain atmospheric greenhouse gas concentrations at around 450 ppm CO₂ equivalent, thus limiting climate change (Bernstein et al., 2008). Reduction targets of the European Union suggest a 30% reduction of 1990-levels by 2020 and even up to 80% by 2050 (Commission of the European Communities, 2007). One way of achieving these targets is through Carbon Capture and Storage (CCS) technologies, which includes CO₂ capture at the source, followed by long-term storage. Storage concepts involve the injection of liquid or supercritical carbon dioxide into saline aquifers, designated fractures above the ground, and depleted oil and gas reservoirs. The last one is particularly interesting and recognized as an important CCS method for countries with a major oil or natural gas production and transport infrastructure, such as the United States. In general, injection of CO₂ under supercritical conditions into geological formations such as saline (brine) aquifers has been proposed to sequester CO₂ over a long period of time (Bachu et al., 1994). If sequestration of CO₂ is to be a practicable large-scale disposal method, the CO₂ must remain safely underground (e.g. thousands of years), and not return to the atmosphere within relatively short timescales. The injection of a relatively reactive substance such as CO₂ into the saline aquifers will result in chemical disequilibra-

tion and the initiation of various chemical reactions. It is important to understand the direction, rate and, magnitude of such reactions, both in terms of their impact upon the ability of a host formation to contain the injected CO₂, and in terms of the longevity of CO₂ containment (Rochelle et al., 1999).

1.1 Solubility and Kinetics

Upon injection of CO₂ into saline aquifers, production of weak carbonic acid (H₂CO₃) results from the dissolution of supercritical CO₂ into aquifer brine. This process is referred to as solubility trapping. The subsequent increase in the acidity of the solution due to dissolution of CO₂ induces primary minerals to dissolve into the brine (Palandri, 2004). Precipitation of secondary carbonate minerals follows when aqueous species of dissolved CO₂ react with dissolved minerals (Bachu et al., 1994; Dufaud et al., 2009; Giammar et al., 2005; Guyot et al., 2011; Oelkers and Cole, 2008; Oelkers and Schott, 2005; Prigiobbe et al., 2009). The process known as mineral trapping. Solubility and mineral trapping are widely considered as the most promising long term solutions to geologic CO₂ sequestration (Metz et al., 2005). Both mechanisms are understood to play a vital role in the overall process of CO₂ sequestration in saline aquifers by facilitating enhanced dissolution through natural convection (Ennis-King et al., 2003; Rapaka et al., 2008; Riaz et al., 2006) and the formation of stable carbonate precipitates (Xu et al., 2002). Experimental data for the solubility of CO₂ in H₂O-NaCl solutions is available for various values of temperature and salinity (Barta and Bradley, 1985; Chou et al., 1989; Cramer,

1982; Drummond, 1981; He and Morse, 1993; Koschel et al., 2006; Nesbitt, 1984; Rumpf et al., 1994; Spycher and Pruess, 2010b).

Drummond (1981), Fournier (1985) and Rumpf (1994) provided equations for high salinity cases in the range of temperatures suitable for geologic sequestration of CO₂, but they are not pressure dependent. Duan and Sun (2003) consider the pressure dependence of the salting-out effect for aqueous CO₂ in NaCl solutions from which activity coefficients can be derived for various values of temperature, pressure, and salinity (Duan and Sun, 2003). However, the effects of pressure on the activity of CO₂ appear to be small.

The major concerns for reactive processes are long-term containment of CO₂ and maintenance of injectivity. This is because, when CO₂ dissolves in the formation fluid, the pH of the solution decreases, which can drive mineral dissolution. There may be subsequent precipitation involving the dissolved minerals. The speciation of aqueous CO₂ into carbonic acid, H₂CO₃, bicarbonate, HCO₃⁻ and carbonate, CO₃²⁻ is expected to be kinetically rapid (Kissinger, 1957). On the other hand, due to the relatively slow kinetics of CO₂-brine-mineral interactions, dissolution and precipitation rates of minerals are generally much slower (Gunter et al., 1997). Formation of secondary carbonates consumes aqueous CO₂ and adds it to the solid phase of the geologic environment. The resulting changes in the concentration of aqueous CO₂ and the porosity and permeability of the aquifer can significantly impact the overall sequestration dynamics. The knowledge of time scales for dissolution of primary minerals and precipitation of secondary carbonates is therefore important and requires an accurate determination of the associated reaction rates under aquifer

conditions (Alkan et al., 2010).

Although there are a growing number of experimental studies (Black and Haese, 2014; Carroll and Knauss, 2005; Daval et al., 2009), the investigation of geochemical reactions in the laboratory is difficult because of the (often) slow reaction rates of minerals (Gunter et al., 1997). It is therefore often more efficient to use modeling techniques to investigate geochemical reactions (Bethke, 2008; Parkhurst, 1995; Xu et al., 2004, 1999, 2006; Zhang et al., 2009). A general approach for describing the dissolution rates of minerals as a function of the composition and the saturation state of the aqueous solution is based on the transition state theory (Lasaga, 1981; Schott et al., 2009). Transition state theory is an approach to describe the temperature and concentration dependence of the rate law (Lasaga, 1981; Pechukas, 1981). Models based on this approach have been employed to predict mineral precipitation rates (Knauss et al., 2005; Liu et al., 2011; Steefel and MacQuarrie, 1996; Steefel and Maher, 2009). However, the lack of data over a wide range of temperatures may result in a large degree of uncertainty in the calculation of the Arrhenius activation energy (Zsakó and Arz, 1974), which is needed for determining the reaction rates. Therefore, the straight forward application of transition state theory to predict mineral precipitation rates on the basis of the apparent activation energies may involve inaccuracies (Pham et al., 2011). Moreover, the transition state theory is based on the implicit assumption that the reaction system will pass over the lowest energy saddle point on the potential energy surface (Laidler and King, 1983; Lasaga, 1992; Truhlar et al., 1996). This description is consistent for reactions occurring at relatively low temperatures. However, at high temperatures, molecules populate

higher energy vibrational modes such that their motion becomes more complex and collisions may lead to transition states that exist far from the lowest energy saddle point (Pineda and Schwartz, 2006).

The reaction rates for the precipitation of mineral compositions are generally determined on the basis of the standard temperature dependent Arrhenius equation (Aagaard and Helgeson, 1977, 1982; Rickard and Sjöberg, 1983; Shiraki et al., 2000; Sjöberg, 1978). However, this approach does not always lead to a good agreement with experimental data (Nielsen, 1964; Reddy and Gaillard, 1981; Rodriguez-Blanco et al., 2011). Saldi et al. (2012) also point to additional modeling errors that may arise due to compositional variation of synthetic samples, uncertainties in pH titration, and contact surface area. For synthetic mineral samples, there is a high degree of uncertainty in the experimentally determined values for the rates of dissolution and precipitation. For example, variation in composition, degree of cation disorder, degree of crystallization, as well as the frequency and distribution of crystal defects, contribute to these uncertainties. Precipitation of secondary minerals can act as a passivating layer to decrease the reactive surface area of mineral compositions, which inhibits further dissolution under dynamic conditions (Daval et al., 2009).

Phenomenological models that do not take the above mentioned factors into account may overestimate the amount of precipitate formed (Gaus et al., 2005; Haszeldine et al., 2005; Hellevang and Aagaard, 2010). To overcome some of these limitations, Palandri (2004) suggested an extension of the standard Arrhenius equation, where the logarithm of the reaction rate depends on the reaction order and pH as well as the activation energy and temperature. In this study, we employ

this new approach to find the rate of precipitation reaction. Moreover, the effect of pressure and salinity are also taken into account here in the calculation of the pH. This requires the determination of the pH of the aqueous phase as a function of the amount of CO₂ dissolved, which in turn depends on conditions of pressure, temperature, and salinity of brine. This is followed by a sensitivity analysis with respect to the dissolution rate of calcite to highlight the effect of the reaction order, n , on the reaction rate. Another important consideration in the modeling of reactions rates is the impact of dissolved salts on the solubility and reaction rates in non-ideal solutions. Mole fractions of dissolved CO₂ are modified by activity coefficient of CO₂ with respect to salinity of aqueous phase.

The first objective of the current study is to determine the association between the solubility of CO₂ and the kinetics of chemical reactions on the basis of the transition state theory. We characterize the rate of reactions on the basis of the solubility of supercritical CO₂ and the pH of the aqueous solution with respect to changes in pressure, temperature, and salinity. Our focus is on developing a basic understanding of how reaction kinetics of precipitate formation and dissolution are influenced by the thermodynamic basis for the solubility of CO₂ in liquid phase of different salinities. We show how activity coefficients based on various models affect solubility, pH and kinetics of chemical reactions. The significance of our study is that we perform sensitivity analysis with respect to the dissolution rate of calcite to highlight the effect of the reaction order, n , on available rate laws. The reaction order is treated as a free parameter in our model to obtain agreement with experimental data. The effect of temperature on the pre-exponential factors is also analyzed in this

study by this method. Thus, the sensitivity analysis of reaction rates with respect to the reaction order and pre-exponential factors help us obtain good agreement with experimental results. The application of sensitivity analysis will lead to an equation that can describe mineral dissolution rates as a function of temperature, pressure, salinity, and saturation state. Finally, we simulate precipitation buildup on the basis of the obtained reaction rates to investigate the impact of fractures on CO₂ transport and storage capacity.

In this study, the native aqueous phase in the aquifer is taken to be brine, which is assumed to be made up of H₂O and NaCl. Although the composition of the actual brine in saline aquifers may be more complex, our objective is to model the fundamental behavior under well characterized conditions for which experimental and modeling data is available. We thus seek to understand the complex kinetic modeling of key reactions only. The simplification of the complex kinetic model may, however, lead to deviation from reality. This discrepancy may arise due to the factors such as nucleation, surface complexation, hydrogen bond, hydration, chemical reaction, ionization, and reaction orders that could influence phase relations and reactions.

We assume that the solid phase of the geologic environment is anorthite, which provides the free calcium needed for calcite formation (Smith et al., 2011; Zhu et al., 1994). Anorthite is one of the two major solid-solution components of plagioclase feldspar (Zhu et al., 1994). We focus on calcite as one of the possible secondary carbonates due to the high fugacity of CO₂ under supercritical conditions (Berner et al., 1983; Flaathen et al., 2011; Marini, 2007; Weibel et al., 2011; Xu et al., 2004;

Xu and Pruess, 2001).

1.2 Density

The second objective of the current study is to determine the change in the density of brine upon dissolution of CO₂. When CO₂ dissolves in the liquid phase, the change of solution density depends on the mole fraction and the apparent liquid molar volume of dissolved CO₂. The mole fraction of dissolved CO₂, however, depends in turn on the molar volume of CO₂ in the gas phase. Both the liquid and the gas phase molar volumes are functions of temperature and pressure.

Equations of state (EOS) are an important tool for the correlation and prediction of thermodynamic properties and phase behavior of pure substances and mixtures. Therefore EOS are widely used in design, simulation and optimization of chemical processes. In particular, cubic EOS are routinely used to calculate mole fraction and thermophysical properties of CO₂. This approach proves to be simple and accurate for engineering calculations. However, when these equations are used with the classical van der Waals mixing rules they do not perform well for highly polar, asymmetric and/or associating mixtures. Consequently, numerous mixing rules have been proposed to extend the capabilities of cubic EOS. Recently, several mixing rules have been developed that contain excess Gibbs energy (G_{ex}) models (Escobedo-Alvarado et al., 2001).

To date, the molar volume of CO₂ in the gas phase has been characterized extensively by Spycher and Pruess (2005, 2010b) based on equating chemical po-

tentials and by using an improved Redlich-Kwong equation of state (RK-EOS) to express departure from ideal behavior. In this model the two correcting factors of RK-EOS are obtained from fitting of available data that lead to an accurate computation of the molar volumes of CO_2 in the gas phase as compared to the previous case where the correcting factors were constant and they were both derived from the critical point of CO_2 (Lemmon et al., 2003; Marini, 2007). These molar volumes of CO_2 in the gas phase are subsequently employed to calculate the mole fraction of dissolved CO_2 . Another method for finding the gas molar volume is used by Duan et al. (1992). Their approach is based on a virial-type equation of state which contains fifteen adjustable parameters and can only be used for vapor state. The RK-EOS formulation of Spycher and Pruess (2005) is computationally more efficient and Pruess and Spycher (2007) find it suitable for the numerical simulation of CO_2 -brine flow in porous media. Spycher and Pruess (2010b) refine their improved RK-EOS to compute the mutual solubility of CO_2 and H_2O at elevated temperatures ($> 100^\circ\text{C}$).

The novelty of the current approach is to determine the solution density on the basis of the molar volume of liquid CO_2 that is obtained directly from an improved RK-EOS. The advantage of this approach is to readily obtain both the mole fraction of dissolved CO_2 and the solution density of binary H_2O - CO_2 and ternary H_2O - CO_2 - NaCl solutions on the basis of a single equation of state under generalized pressure, temperature, and salinity conditions. To this end, we modify the current RK-EOS to yield improved estimates of the molar volume of liquid CO_2 as one of the solutions of the cubic equation. The correct solution branch associated with the gas molar

volume is retained. The new solution branch is constrained to coincide with the liquid molar volume that is obtained from experimental data for the density of the binary solution of CO_2 and H_2O . Due to a high degree of variation in experimental results, the densities of the binary solutions are obtained with the help of a multi-parameter nonlinear regression with respect to pressure and temperature. These density values of the binary solutions are used to find the partial molar volume of liquid CO_2 . The strength of this approach is combining accurate molar volume of CO_2 in the gas phase with the more representative characterization of the liquid molar volume within a single EOS. The results from this new approach are shown in this study to be more accurate compared with the prediction of Duan et al. (2008). Using the modified equation of state, we predict the density of saturated ternary solutions and find good agreement with experimental data. Finally, we use our model to investigate the effects of temperature, pressure, and salinity on the onset of buoyancy driven convection during CO_2 sequestration.

1.3 Reactive Transport Modeling

The third objective of the current study is to investigate the impact of fractures on CO_2 transport and storage capacity. Fluid convection, diffusion and chemical reactions inside a finite space will be carried out numerically as a simplified representation of natural mineral trapping. The current model predicts the actual efficiency of the mineral trapping mechanism by considering the physical properties of the fluid such as its density, its pH, as well as the characteristics of the mineral compositions

and physical properties of a fracture. This model may give information about the precipitation of calcite inside a fracture during sequestration of CO_2 .

The problem involves flow of dissolved CO_2 between finite walls that represents a single fracture. After injection into fractured rocks, CO_2 starts reacting with water molecules (H_2O) that produces carbonic acid (H_2CO_3). pH reduction due to the solubility of CO_2 induces rock mineral alteration (Nomeli and Riaz, 2014; Palandri, 2004). Aqueous H_2CO_3 dissociates to bicarbonate HCO_3^- and carbonate CO_3^{2-} ions and then reacts with free calcium Ca^{2+} which is provided with a certain rate and they eventually convert to the secondary mineral which is called calcite CaCO_3 . The sources of calcium Ca^{2+} and carbonate ions CO_3^{2-} required for continued precipitation are (1) transport of carbonate ion by fluid flow and (2) presence of calcium ions from the walls. Since carbonate ions are transported by fluid flow, an under-saturated solution becomes supersaturated when it goes through the fracture. Because of the slow movement of reactive fluid, the equilibrium is completely reached between the fracture surfaces in contact with that fluid.

Dissociation of carbonic acid to bicarbonate and carbonate ions is almost instantaneous and can be effectively considered at equilibrium. However, the chemical reaction leading to the production of calcite is kinetically slow (Jacobson and Langmuir, 1974; Mucci, 1983; Visconti et al., 2010). the highlighted sentence has been removed because this sentence will be said in a correct way (solubility product instead of dissociation constant) in the chapter 5. On a long time scale, however, CO_2 can be permanently trapped inside fractures as a form of calcite.

Reactive transport in pore network is a dynamic process that affects: mineral

composition and surface chemistry, porosity, permeability, and fluid flow. Fracture height can shrink or get larger as the chemical reactions proceed at the fracture surface. Mass conservation equation is applied for the aqueous species to find out how the fracture height changes with time. Laubach et al. (2000) observed that the same differential stresses control the behavior of both large and tiny fractures. The results of his studies show that mineralization of macro-fractures is similar to micro-fractures in numerous cases (Laubach, 2003). Therefore, macro-fractures study provides useful information about the fate of micro-fractures through mineral trapping of CO₂.

There are several different parameters that affect the calcite precipitation/dissolution such as reaction order, complexes, adsorption, convection, diffusion, and desorption. To date, because of lack of data on nucleation and precipitation of calcite under aquifer conditions, estimation of the amount of trapped CO₂ through mineral trapping after a specific period of time has been a critical unresolved problem. Recently, the solubility kinetics of calcite under aquifer conditions are investigated by Nomeli and Riaz (2014). Moreover, the fundamental issue in mineral trapping of CO₂ is to perceive how the fractures are filled with precipitates and cease to be fluid channels. To resolve such issues, reactive transport is carried out in the current study, transport and reactions are solved by means of a direct numerical solution of the Navier-Stokes equations. This interaction between fluid flow and chemical reactions is found to be significant and plays a pivotal role through mineral trapping of CO₂; however, a large computational penalty has to be paid if this is considered explicitly.

1.4 The outline of the study

This study is organized as follows. Chapter 2 is dedicated to problem statement. In chapter 3 the solubility of CO_2 is quantified at different temperature, pressure, and salinity values. Subsequently, the dependence of pH on the amount of dissolved CO_2 is investigated on the basis of the electro neutrality condition, and then the precipitation rate of calcite is predicted with the help of the transition state theory. Afterwards, the kinetics of the chemical reactions, after dissolution of CO_2 in the liquid phase, is described. This is followed by sensitivity analysis of the dissolution rate of calcite to obtain agreement with experimental data. Finally, the reactive transport in a designated fracture above the ground is simulated to investigate the impact of fractures on CO_2 transport and storage capacity.

In chapter 4 the current study is dedicated towards finding the partial molar volume of liquid CO_2 which are regressed from experimental data on the density of binary solution. This is followed by the modification of the two correcting factors of RK-EOS which yields the accurate molar volume of CO_2 in both the liquid and the gas phase simultaneously. The new correcting factors include the repulsive parameter, which is a measure of the volume of gas molecules and the intermolecular parameter, which describes the effects of molecular attraction. Afterwards, the influence of CO_2 and salinity on density of ternary solutions is analyzed at different temperature and pressure values.

In chapter 5, this study is dedicated toward predicting actual efficiency of the mineral trapping mechanism inside a fracture by considering physical properties of

fluid flow and characteristics of the mineral compositions. In this regard, the impact of fractures on CO₂ transport and storage capacity is investigated.

Chapter 2

Problem Statement

Several methods are currently being investigated to evaluate the sequestration potential of various methods, including injection of CO₂ into geological formations such as deep saline aquifers, depleted oil fields, and also under impermeable cap-rocks. Upon injection into saline aquifers, carbon dioxide is expected to be trapped by one or more of four processes; structural trapping, residual trapping, solubility trapping, or mineral trapping (Hitchon, 1996). First, CO₂ can be trapped as a gas or supercritical (SC) fluid under a low-permeability cap rock. This process will be in short term and commonly referred to as structural trapping. The potential for CO₂ leakage through fractures is the most critical concern in this method. Second, residual trapping happens very quickly when the injected SC-CO₂ displaces brine as it moves through the porous rock. Afterwards, fluid again replaces it, but some of the CO₂ will be left behind in the pore spaces which are immobile (see figure 2.1). Third, SC-CO₂ can dissolve into the groundwater, a process referred to as a solubility trapping. Due to the production of the weak carbonic acid (H₂CO₃) through the latter mechanism, the acidity of the groundwater increases and it subsequently induces the dissolution of primary mineral compositions in liquid phase. Fourth, dissolved CO₂ can react with minerals in a geologic formation, leading to the precipitation of secondary carbonate minerals such as calcite CaCO₃, dolomite

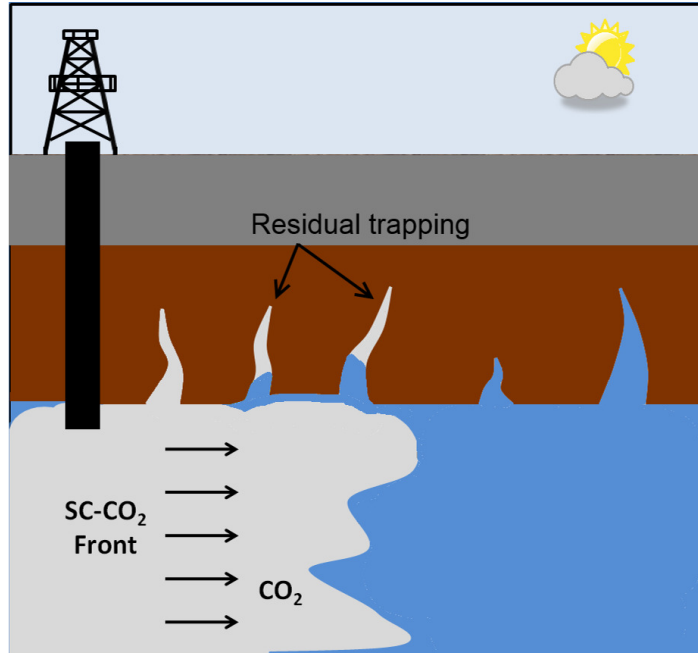


Figure 2.1: Schematic diagram illustrating the residual trapping of supercritical CO_2 .

$\text{CaMg}(\text{CO}_3)_2$, siderite FeCO_3 , and dawsonite $\text{NaAlCO}_3(\text{OH})_2$ by a series of reactions with aqueous ions available in the saline aquifer. This process is so-called mineral trapping of CO_2 (Bachu et al., 1994). Solubility and mineral trapping are the most promising long term solutions to CO_2 sequestration because they prevent its return to the atmosphere. To the best of our knowledge, up to now solubility and mineral trapping of CO_2 have not been connected with great consistency.

In order to find the reaction rates associated with mineral trapping of CO_2 , as a function of temperature and pH, it is necessary to first quantify the solubility of CO_2 with respect to brine. Let us suppose the high-pressure CO_2 is injected into a system made up of a relatively deep aquifer hosting an aqueous solution, most likely of high sodium chloride NaCl salinity. In order to find solubility of CO_2 , we have

first to evaluate temperature and pressure conditions that will depend on the depth of the aquifer as well as on the local geothermal gradient and pressure gradient. For economic reasons the depth of deep saline aquifers may be in the order of several kilometers. Taking a surface temperature of 20°C and average geothermal gradient of 30°C km⁻¹, temperature will be 50°C at 1 km and 110°C at 3 km. Assuming an hydrostatic gradient of 100 bar km⁻¹, pressure will be 101 bar at 1 km and 301 bar at 3 km. Therefore, to investigate the sequestration potential of deep saline aquifers we have to calculate, initially, the thermodynamic properties of H₂O-CO₂ mixtures up to temperatures slightly in excess of 100°C and pressures of several hundred bars.

Solubility depends, in addition to pressure and temperature, on the salinity in brine. Experimental data for the solubility of CO₂ in H₂O-NaCl solutions is available for various values of temperature and salinity (Barta and Bradley, 1985; Chou et al., 1989; Cramer, 1982; Drummond, 1981; He and Morse, 1993; Koschel et al., 2006; Nesbitt, 1984; Rumpf et al., 1994; Spycher and Pruess, 2010b). Prutton and Savage (1945) documented one of the earlier attempts to measure the solubility of CO₂ in calcium chloride-water solutions at 75, 100, 120°C and high pressures. Takenouchi and Kennedy (1965) reported solubility measurements of CO₂ in 6 and 20 weight percent NaCl solution up to 1400 bar pressure and up to temperatures of 450°C. Rumpf et al. (1994) measured the solubility of CO₂ in aqueous solutions of sodium chloride in the temperature range from 40 to 160°C, up to 6 mol/kg salt solutions and total pressures up to 10 MPa. More recently, Koschel et al. (2006) studied the dissolution of carbon dioxide in water and in aqueous solution of sodium chloride by measuring the heat of mixing of a supercritical gas with the liquid phase

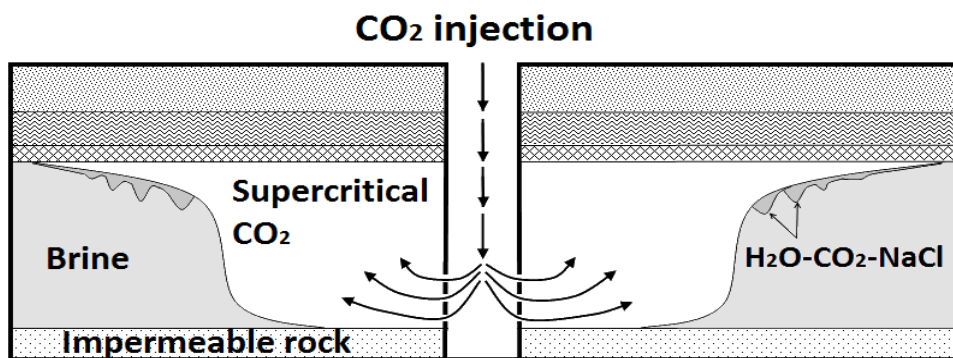


Figure 2.2: Schematic diagram illustrating a CO₂ injection site consisting of a saline aquifer. After injection CO₂ spreads through the reservoir, displacing reservoir brine.

at temperatures of 323.1-373.1 K, and at pressures up to 20 MPa.

Previous experimental investigations highlight the substantial effect of the salinity by considering the activity coefficients in the solubility of CO₂ rich phase across a wide range of pressure and temperature conditions (Chou et al., 1989). A number of different activity coefficient models are available for simulating reactive processes (Thomas et al., 2012; Wigand et al., 2008). The activity coefficient models based on Debye-Hückel type equations have limited applicability for high salinity solutions (Allen et al., 2005). For instance, the B-dot equation (Helgeson, 1969) or Davies equation for calculating the activity coefficients are not accurate for salinities greater than about 1 molal sodium chloride (Allen et al., 2005). Activity coefficients in high salinity solutions are measured by Pitzer and Truesdell-Jones (Pitzer and Mayorga, 1973). However, these do not cover the temperature range of interest for geological sequestration of CO₂ (above 25°C) (Allen et al., 2005).

Figure 2.2 shows that CO₂ is injected into a deep aquifer which is made up of

salinity through geological sequestration. In order to investigate the sequestration potential of a deep aquifer we need to set up a PVTx model to predict the thermodynamic properties of the solutions for temperatures between 50 and 100°C and pressures up to 600 bar, which are the conditions for a typical aquifer. Since we are interested in the long-term behavior of the system, the aquifer rocks are assumed to be reactive. In order to predict the long-term behavior of dissolved CO₂, we need to consider the kinetics of the reactions between fluids and aquifer rocks.

Carbon dioxide is introduced into saline aquifers typically in the supercritical state that forms an immiscible phase with respect to the resident liquid phase, brine, which is made up of relatively small fractions of various salts dissolved in water. CO₂ is soluble in brine, in which it spontaneously converts between CO₂ and H₂CO₃ (carbonic acid). Dissolution of CO₂ in brine alters the density of the original solution. After injection, CO₂ will initially tend to accumulate and spread out near the top of the permeable space (Pruess and García, 2002). This occurs because the density of the CO₂ at supercritical state is much lower than the density of brine. At the interface between the SC-CO₂ and brine, CO₂ starts to react with water molecules available in the aqueous phase (see Figure 2.3). H₂O-CO₂ and H₂O-CO₂-NaCl are the most common solutions in various geological environments (Hu et al., 2007; Schmidt and Bodnar, 2000) and the equilibrium properties of these solutions play a significant role in understanding of geological sequestration of CO₂ in deep saline aquifers.

Due to CO₂ dissolution, the aqueous-phase density increases by a few percent (Spycher et al., 2003). The hydrodynamically unstable fingers tend to migrate

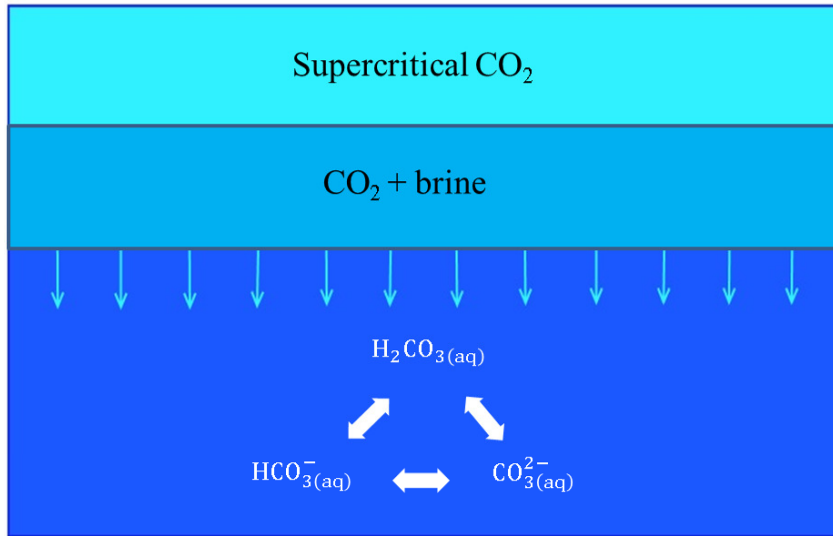


Figure 2.3: Dissolution of CO_2 into saline formation at the interface.

downward when the brine is enriched in CO_2 . It is known that density differences of about 0.1 kg m^{-3} are sufficient to make buoyant plumes which is crucial for the natural transport of dissolved CO_2 in deep saline aquifers (Haugan and Drange, 1992; Neufeld et al., 2010; Riaz and Tchelepi, 2006). Therefore, accurate prediction of solution density after dissolution of CO_2 is very important through the solubility and mineral trapping. Furthermore, the knowledge of PVTx model can be implemented in the oil and gas industry, civil and environmental engineering such as waste water treatment (Kumar et al., 2010; Pandit et al., 2011). Nowadays, with increasing interest in understanding the behavior of CO_2 in both above- and below-ground with respect to sequestration, the PVTx properties of the system are becoming important (Gislason et al., 2010; Hawthorne et al., 2011; Yu et al., 2011; Zhu et al., 2011).

Table 2.1: Experimental studies performed to determine the density of the CO₂-H₂O solution. The last column gives the range of concentrations, as mole fraction $x(\text{CO}_2)$, at which the density was determined.

| Authors | T/K | P/bar | Mole fraction of CO ₂ /% |
|--------------------------------|-----------------|------------------|-------------------------------------|
| Li et al. (2011) | 273 - 573 | 0.001 - 1000 | 0 - saturated values |
| Song et al. (2005) | 276, 283 | 40 - 120 | 0 - saturated values |
| Bando et al. (2004) | 303 - 333 | 100 - 200 | 0 - saturated values |
| Song et al. (2003a,b) | 273.25 - 284.15 | 50 - 125.0 | 0 - 0.61 |
| Zhang et al. (2002) | 308.15 | 77.52 - 124.84 | 99.7 |
| Blencoe et al. (2001) | 573.15 | 74.4 - 999.3 | 0 - 0.9 |
| Teng et al. (1997) | 278 - 293 | 64.4 - 294.9 | 0 - saturated values |
| Seitz and Blencoe (1997) | 573.15 - 623.15 | 999.3 | 0.1 - 0.9 |
| Teng and Yamasaki (1998) | 278 - 293 | 64.4 - 294.9 | 2.50 - 3.49 |
| Wood et al. (1996) | 298.15 - 633.41 | 10 - 350 | 0.279 - 0.332 |
| Fenghour et al. (1996) | 415.36 - 644.78 | 58.84 - 279.64 | 0.0612 - 0.7913 |
| Ohsumi et al. (1992) | 276.15 | 347.54 | 0.1798 - 0.6294 |
| King et al. (1992) | 288.15 - 298.15 | 60.8 - 243.2 | 2.445 - 3.070 |
| Zhang and Frantz (1992) | 519.95 - 634.45 | * | 5.5 - 16.5 |
| Crovetto and Wood (1992) | 622.75 - 642.70 | 196.4 - 281.3 | 0.48 - 0.8745 |
| Sternor and Bodnar (1991) | 494.15 - 608.15 | 487 - 3100 | 0.1234 - 0.7473 |
| Nighswander et al. (1989) | 352.85 - 471.25 | 20.4 - 102.1 | 0.22 - 1.66 |
| Patel and Eubank (1988) | 323.15 - 498.15 | 0.855 - 100.237 | 0.02 - 0.5 |
| Patel et al. (1987) | 323.15 - 498.15 | 1 - 100 | 0.5 - 0.98 |
| Wormald et al. (1986) | 473.2 - 623.2 | 10 - 120 | 0.5 |
| Zakirov (1984) | 573.15 | 50 - 1800 | 0.3 - 0.77 |
| Parkinson and De Nevers (1969) | 278.1 - 313.7 | 10.342 - 344.744 | 0.1 - 2.2 |
| Ellis and Golding (1963) | 504.15 - 643.15 | 47.91 - 254.43 | ** |
| Ellis (1959b) | 387.15 - 621.15 | 5 - 164 | 3.90, 6.27, 84.02 |

*Pressures are not reported, but can be calculated from their empirical formulations,
**concentrations are not directly reported, but can be calculated from the report.

Available experimental data for the density of binary H₂O-CO₂ solutions is summarized in Table 2.1. Most data is not applicable to CO₂ sequestration because it does not correspond to the saturated state of dissolved CO₂. We therefore use data reported by Li et al. (2011), Song et al. (2005), Bando et al. (2004), and Teng et al. (1997), for the density of saturated solutions. In general, the density of the saturated binary H₂O-CO₂ solution is observed to increase with pressure. This occurs because higher pressures increase the saturated mole fraction of dissolved CO₂ (Spycher and Pruess, 2010b), which increases solution density. Higher temperatures tend to decrease the density. This occurs because high temperatures lower the saturated mole fraction of dissolved CO₂, which results in a lower density (Marini, 2007).

An accurate determination of the liquid and gas molar volume of CO₂ is required for calculation of the solutions density. Previous studies find it difficult to accurately determine the molar volume of CO₂ in both the liquid and the gas phase simultaneously from a single equation of state (Duan et al., 2008; Spycher and Pruess, 2010b). Therefore, engineering applications currently use different models for the liquid and gas phase molar volumes. The equation of state proposed by Spycher and Pruess (2010b) gives the molar volume of CO₂ accurately only for the gas phase but not for the liquid phase. This difficulty arises because the correcting factors in the current RK-EOS of Spycher and Pruess (2010b) are optimized to match gas molar volumes determined experimentally and are also only temperature dependent. Experimental characterization of liquid molar volumes as a function of temperature and pressure is time consuming and experimental data is often available only for a limited range of pressure and temperature. Moreover, the laboratory

data is difficult to be compared among different studies (Duan et al., 2008). This is because the under-saturated mole fraction of CO_2 and the corresponding solution pH vary in different experiments.

Sequestration of CO_2 is completed by mineral trapping (Hitchon, 1996). Mineral trapping prevents mobile hazards such as leakage of CO_2 to the atmosphere (Bachu et al., 1994; Shogenova et al., 2009). The appealing concept that CO_2 could be permanently trapped as aqueous species and mineral precipitates in the fractures has prompted several experimental and numerical studies to investigate these principal mechanisms. Numerical modeling of reactive processes is required for investigating the long-term sequestration of CO_2 in the fractures. This is because mineral alterations are very slow and are not experimentally accessible. In the current study, we develop a numerical model for a reactive fluid flow within a designated fracture in order to evaluate long term mineral trapping of CO_2 . The numerical model analyzes the impact of CO_2 immobilization through carbonate precipitation inside the fracture.

Fractures are defined as fluid channels that have a high permeability (Noh, 2003). CO_2 trapping by secondary carbonate minerals such as calcite CaCO_3 , dolomite $\text{CaMg}(\text{CO}_3)_2$, siderite FeCO_3 , and dawsonite $\text{NaAlCO}_3(\text{OH})_2$ could occur in the fractures (Gislason et al., 2010). Since fugacity of CO_2 is high, calcite is a wide spread mineral under the conditions considered in our investigation (Marini, 2007). The addition of CO_2 mass as secondary carbonates to the solid phase leads to a decrease in permeability of the fractures. Consequently the fractures may become filled with precipitates of minerals. Permeability of the fracture controls the path of

aqueous CO₂ migration; therefore the variation of fracture dimension has a pivotal role on solubility and mineral trapping of CO₂. Although mineral kinetic properties and reactive surface areas are not well constrained and the range of problems concerning the interaction of water-CO₂-minerals is very broad, the numerical modeling gives us useful insights into the storage of CO₂ in both above- and below-ground.

Although experimental fluid dynamics play an important role in validating and determining the limits of the various approximations to the governing equations, it is limited in the Reynolds number it can achieve. Therefore, it is usually short of full scale. Furthermore, high temperature values associated with coupled reactive fluid flow problems are also beyond the scope of many experimental facilities. This is particularly true of reactive mass transfer problems where the changing mineral compositions add another level of complexity. Many geological formations are too big or too remote in space or in time to simulate experimentally. Therefore, obtaining detailed information of fluid flow would be expensive and time consuming. Moreover, geological reservoir and porous media flows are generally inaccessible to detailed experimental measurement because mineral alterations are very slow throughout geological sequestration of CO₂ (Busch et al., 2010). Therefore, it would be more practical to sequester CO₂ through fractures above the ground following the generally accepted methods. All of these categories of fluid motion, however, are amenable to the computational approach. Computational fluid dynamics provides detailed information at no additional cost and consequently permits a more precise understanding of the flow processes to be obtained (Molins et al., 2012).

Chapter 3

Effect of CO₂ Solubility on the Dissolution Rates of Minerals in Saline Aquifers for the Temperature Range of 50-100°C and Pressures up to 600 Bar

3.1 Introduction

We develop a model for geochemical reaction rates which is useful for the assessment of the extent of CO₂-brine-mineral interactions in saline solutions with saturated concentration of dissolved CO₂ as a function of pressure, temperature, and salinity. The model accounts for relatively slow dissolution rates of calcite and anorthite in saline aquifers that are perturbed by the subsurface injection of CO₂. The method uses a general, semi-empirical rate equation to which experimental rate data for many minerals can be reasonably well fit. We first evaluate the significance of pre-exponential factor and reaction order associated with the rate equation to determine the sensitivity of the reaction rates as a function to the pH of the system. The new rate equation of the primary minerals is then determined as a function of temperature, pressure, and salinity with a multi-parameter, non-linear regression of semi-empirical data. Then we investigate whether the proposed rate equation can reasonably reproduce reaction rates of minerals with new parameters that we obtained from regression. Afterwards, the effects of these parameters on reaction

rates, Damköhler number, and critical time of blockage for a single fracture are investigated to predict the actual efficiency of the mineral trapping of CO₂.

Upon injection of CO₂ into saline aquifers, production of weak carbonic acid (H₂CO₃) results from the dissolution of supercritical CO₂ into aquifer brine. The subsequent increase in the acidity of the solution induces primary minerals to dissolve into brine (He and Morse, 1993; Palandri, 2004). Precipitation of secondary carbonates follows when aqueous species of dissolved CO₂ react with dissolved minerals (Guyot et al., 2011; Prigiobbe et al., 2009). Natural convection is found to have a positive impact on dissolution of CO₂ into brine (Ennis-King et al., 2003; Riaz and Cinar, 2013; Riaz et al., 2006) and enhances the formation of stable carbonate precipitates (Xu et al., 2002, 2004, 2006). Although the extent of permanent storage through carbonate mineral precipitations is small compared to physical trapping mechanisms, both solubility trapping due to dissolution of CO₂ into brine and mineral trapping due to subsequent precipitation of minerals can be considered to be the most promising solutions to the challenge of long term, secure disposal of CO₂ (Metz et al., 2005).

For geological sequestration of CO₂ in saline aquifers, it is desirable to know the length of time required for a system to equilibrate with respect to alteration minerals and, perhaps more importantly, the rate of dissolution of primary minerals. As a result of CO₂ injection, saline aquifers are perturbed from equilibrium, and will require some length of time to re-equilibrate with alteration minerals. This occurs because the kinetics of CO₂-water-mineral interactions are generally slow at aquifer temperatures, pressures, and salinities (Gunter et al., 1997).

Although there is a growing number of experimental studies (Black and Haese, 2014; Carroll and Knauss, 2005; Daval et al., 2009), the investigation of geochemical reactions in the laboratory is difficult because of the (often) slow reaction rates of minerals (Gunter et al., 1997). Moreover, precipitation rate data do not exist for most minerals, because in mineral precipitation experiments, undesired metastable reaction products usually precipitate instead of the desired mineral, especially far from equilibrium at high degrees of super-saturation. It is therefore often more efficient to use computer modeling techniques to investigate geochemical reactions compared to long-term experiments (Bethke, 2008; Parkhurst, 1995; Xu et al., 2004, 1999, 2006; Zhang et al., 2009).

A general approach for describing dissolution rates of minerals as a function of composition and saturation state of aqueous solution is based on the general Arrhenius-type rate equation (Knauss et al., 2005; Lasaga, 1981; Liu et al., 2011; Schott et al., 2009; Steefel and MacQuarrie, 1996; Steefel and Maher, 2009). However, the lack of data over a wide range of temperatures may result in a large degree of uncertainty in the calculation of the Arrhenius activation energy (Pham et al., 2011; Zsakó and Arz, 1974) which is needed for determining the reaction rates.

Saldi et al. (2012) also point to modeling errors that may arise due to compositional variation of synthetic samples, uncertainties in pH titration and contact surface area. For synthetic mineral samples, there is a high degree of uncertainty in the experimentally determined values for the rates of dissolution and precipitation. For example, variation in composition, degree of cation disorder, degree of crystallization, as well as the frequency and distribution of crystal defects, contributes to

these uncertainties. Precipitation of secondary minerals can act as a passivating layer to decrease the reactive surface area of mineral compositions which inhibits further dissolution under dynamic conditions (Daval et al., 2009). Consequently, numerical simulations that do not take these factors into account may overestimate the amount of precipitate formed (Gaus et al., 2005; Haszeldine et al., 2005; Hellevang and Aagaard, 2010).

Another important consideration in the modeling of reaction rates is the impact of dissolved salts on the solubility and kinetics of chemical reactions in non-ideal (e.g. concentrated) solutions. Therefore, in the current study, effective concentrations of aqueous species, that is called activity, is considered for the calculation of the reaction rates. Activity coefficients in high salinity solutions are commonly modeled using the equations of Pitzer (1991). However, these do not cover the temperature range of interest for geological sequestration of CO₂ (Allen et al., 2005). Rumpf et al. (1994), Fournier (1985), Drummond (1981), Duan and Sun (2003) fit a Pitzer ion-interaction model for activity coefficient of CO₂ (Spycher and Pruess, 2005) and reasonably reproduce experimental solubilities. In this study, we further evaluate the effect of these activity coefficient models on the reaction rates. It is found that activity coefficient of CO₂ due to the presence of NaCl affects solubility, pH and kinetics of chemical reactions. However, we find that pH and mineral kinetics are less sensitive to different activity coefficient calculations as compared to solubility.

The objective of the current study is to determine the association between the solubility of CO₂ and the dissolution rate of minerals. We characterize the rate of reactions on the basis of the solubility of supercritical CO₂ and the pH of

the aqueous solution with respect to changes in pressure, temperature, and salinity. The significance of our study is that we perform sensitivity analysis with respect to reaction order, pre-exponential factor, and Arrhenius activation energy to highlight the effects of these parameters on available rate laws. The sensitivity analysis of reaction rates with respect to reaction order, n , helps us to obtain good agreement with experimental results. The dissolution rate equation in saturated solutions is then determined as a function of only parameters that are available as variables or constants during program execution such as pressure, temperature, and salinity with the help of a multi-parameter nonlinear regression of semi-empirical data.

Formation of precipitates consumes aqueous CO_2 and adds it to the solid phase of the geologic environment. The resulting changes in the concentration of aqueous CO_2 and the porosity and permeability of the aquifer can significantly impact the overall sequestration dynamics. In this study, a long-term reactive transport of CO_2 storage is carried out in a single fracture to investigate the impacts of temperature, pressure, and salinity on the reaction rates and, subsequently, the critical time of blockage due to precipitation of carbonates.

This chapter is organized as follows. In section 3.2 we will describe the kinetics of the chemical reactions after dissolution of CO_2 in the liquid phase. In section 3.3 we will perform sensitivity analysis of reaction rates with respect to the reaction order and pre-exponential factor and then determine the rate equations by means of nonlinear regression of semi-empirical data. This is followed by simulation of a single fracture on the basis of the obtained reaction rates to investigate the impact of fractures on CO_2 transport and storage capacity. In appendix A.1 we will quantify

the solubility of CO₂ at different temperature, pressure, and salinity values. In appendix B.1 we will investigate the dependence of pH on the amount of dissolved CO₂ on the basis of the electro neutrality condition.

3.2 Model description

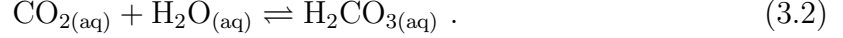
Carbon dioxide is introduced into saline aquifers typically in supercritical state (pressure above 73.8 bars and temperature above 31°C). The partitioning of gas CO₂ into a dissolved aqueous phase is described by



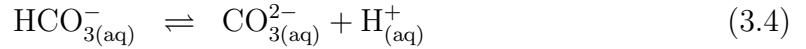
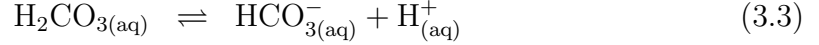
where subscripts, g and aq, indicate the gas and the aqueous phase, respectively. In this study, the native aqueous phase in the aquifer is taken to be brine, which is assumed to be made up of H₂O and sodium chloride NaCl salt. Although the composition of actual brine in saline aquifers may be more complex, our objective is to model the fundamental behavior under well characterized conditions for which experimental and modeling data is available. The simplification of the complex kinetic model may, however, lead to deviation from reality. This discrepancy may arise due to the factors such as nucleation, surface complexation, hydrogen bond, hydration, chemical reaction, ionization and reaction orders that could influence phase relations and reactions.

The amount of dissolved CO₂ depends upon the pressure, temperature and salinity conditions at the interface separating CO_{2(g)} and brine. Aqueous CO_{2(aq)}

combines with the $\text{H}_2\text{O}_{(\text{aq})}$ present in brine to form carbonic acid according to



Carbonic acid further decomposes into bicarbonate and carbonate ions according to the following equilibrium reactions



Dissolution of CO_2 into brine results in the production of carbonic acid (H_2CO_3) leading to the subsequent generation of $[\text{H}^+]$ ions. We determine the pH of the aqueous phase as a function of the amount of CO_2 dissolved, which in turn depends on conditions of pressure, temperature and salinity of brine. The pH of CO_2 enriched brine can be determined on the basis of the electro-neutrality condition by combining the speciation equilibrium model of Li and Duan (2007) with the solubility model of Spycher and Pruess (2005) as follows,

$$[\text{H}^+] = \sqrt{(\text{K}_{\text{a}1} + \text{K}_{\text{a}2}) \text{C}_{\text{T}} + \text{K}_{\text{w}}} , \quad (3.5)$$

where, $\text{K}_{\text{a}1}$ and $\text{K}_{\text{a}2}$ are the first and second dissociation constants, respectively. $\text{K}_{\text{w}} = [\text{H}^+][\text{OH}^-] \approx 10^{-14}$ is dissociation constant for water at standard pressure and temperature (Quist, 1970). The total concentration of carbonate species in the aqueous phase is denoted by C_{T} . The dissociation constants for the reactions considered must be valid for the temperature and pressure range of the system. Finally, pH is the negative logarithm of the activity of hydrogen ions in solution, $\text{pH} = -\text{Log}_{10} [\text{H}^+]$.

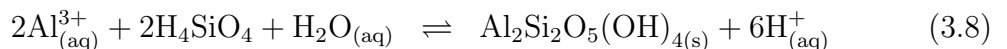
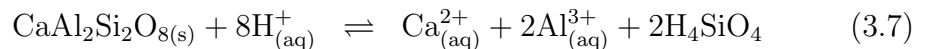
Assuming brine to be made up of H₂O and NaCl, the solubility of CO_{2(aq)} in brine can be quantified by the mole fraction, x_{CO_2} , given by

$$x_{\text{CO}_2} = \frac{m_{\text{CO}_2}}{m_{\text{CO}_2} + m_{\text{H}_2\text{O}} + 2 m_{\text{NaCl}}}, \quad (3.6)$$

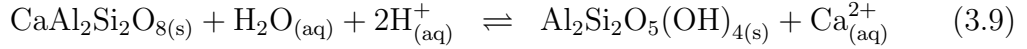
where m_{CO_2} , $m_{\text{H}_2\text{O}}$ and m_{NaCl} denote, respectively, the total molality of aqueous species of dissolved CO₂, H₂O and NaCl in the solution.

We assume that the solid phase of the geologic environment is anorthite, which provides free calcium needed for calcite formation (Smith et al., 2011; Zhu et al., 1994). Feldspars make up nearly 60% of the earth's crust (Smith, 1994) and are present in both typical reservoirs and caprocks (Gaus, 2010). Anorthite (the Ca-end-member of the feldspar group) can be found in many geologic settings (Hangx and Spiers, 2009), and it has been specifically studied because its dissolution rate may significantly increase the porosity of reservoirs (Sorai et al., 2007) and because the Ca cation provides the potential of permanently sequestering injected CO₂ through the formation of carbonate minerals. We focus on precipitation of calcite because it is the more stable mineral composition in comparison with magnesite (MgCO₃), siderite (FeCO₃), dolomite (CaMg(CO₃)₂), and dawsonite (NaAlCO₃(OH)₂) due to the high fugacity of CO₂ under supercritical conditions (Berner et al., 1983; Flaathen et al., 2011; Marini, 2007; Weibel et al., 2011; Xu et al., 2004; Xu and Pruess, 2001).

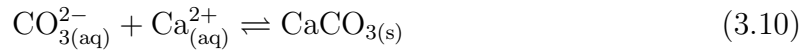
In the presence of H₂O_(aq) and hydrogen ions, anorthite, CaAl₂Si₂O_{8(s)} produces free calcium Ca_(aq)²⁺ according to the following reactions



By combining reactions 3.7 and 3.8, as to eliminate the expression for aqueous aluminum, the dissolution of anorthite and kaolinite can be obtained from the following equation:



where subscript, s, indicates the solid phase. This free calcium then combines with the carbonate ions to form a solid precipitate of calcium carbonate (Calcite).



Even though the liquid phase is made up of many aqueous species, including H^+ , Ca^{2+} , CaHCO_3^+ , OH^- , HCO_3^- , CO_3^{2-} , as long as the equilibrium reactions between each secondary species and basic reactants have been considered, reactions among the secondary species are not required to determine the amount of $\text{CO}_2(\text{g})$ needed to produce a given amount of calcite (Bethke, 2008).

Chemical equilibrium models are typically used to describe reversible and fast reactions such as those in Eqs. 3.3 and 3.4. However, a kinetic method is required when dealing with slower reaction involving dissolution and precipitation of mineral compositions such those in Eqs. 3.9 and 3.10.

The reaction rates for the dissolution of mineral compositions are generally determined on the basis of the temperature dependent Arrhenius equation (Aagaard and Helgeson, 1977, 1982; Rickard and Sjöberg, 1983; Shiraki et al., 2000; Sjöberg, 1978). However, this approach does not always lead to a good agreement with experimental data (Nielsen, 1964; Reddy and Gaillard, 1981; Rodriguez-Blanco et al., 2011). To overcome this limitation, Palandri (2004) suggested an extension of the

standard Arrhenius equation where the logarithm of the reaction rate depends on the reaction order and pH, as well as the activation energy and temperature, as,

$$\log_{10} k' = \log_{10} A - \frac{E}{2.3025 RT} - n \text{ pH} , \quad (3.11)$$

where, k' is the dissolution rate normalized to the reacting surface area (\log_{10} mole $\text{m}^{-2}\text{s}^{-1}$), R is the universal gas constant, E , is Arrhenius activation energy (kJ mole^{-1}) and n , is generally a fractional number typically regarded as a factor to make the model fit the data, but can have theoretical meaning such as reaction order with respect to pH of the saturated solutions (Lasaga, 1998, 1995; Oelkers et al., 1994). The pre-exponential factor, A , also known as a frequency factor, represents the frequency of collisions between reactant molecules. The acidic, neutral, and basic regions were selected by Hellmann (1994) to be the ranges of pH, 1.3 to 4.0, 5.6 to 8.2, and 8.6 to 10.3, respectively. Due to the dissolution of CO_2 , which results in production of H_2CO_3 , the pH of the brine is within acidic region. The pre-exponential factor for dissolution of anorthite and calcite within the range of interest can be obtained from the model of Palandri and Kharaka (2004). Values for activation energy, E , are reported by Icenhower and Dove (2000). In general, application of these parameters is within the range of conditions under which the parameters were obtained, i.e. from 25 to 300°C and the pH between 1.3 and 10.3. At a given pH associated with solubility of supercritical CO_2 at given temperature, pressure and salinity, dissolution rate can be obtained from Eq. 3.11.

The selected equation applies only to bulk dissolution rates and it does not account for temperature dependence of the pre-exponential factor A and apparent

pH dependence of the activation energy E , which can be described using adsorption isotherms (Lasaga, 1995). Therefore, the rate equation we have selected, Eq. 3.11, requires improvement. In the current study we show that E and A depend on n but not on pH as we show with experimental data therefore we vary n , A and E to get a better match with experimental data.

In the following section we will evaluate the significance of the pre-exponential factor A , activation energy E and the reaction order n associated with the rate equation to determine the sensitivity of the reaction rates as a function to the pH of the system. The sensitivity analysis of reaction rates with respect to n , A and E helps us to obtain good agreement with experimental results. The dissolution rate equation in saturated solutions is then determined as a function of pressure, temperature and salinity with the help of a multi-parameter nonlinear regression of semi-empirical data.

3.3 Sensitivity analysis

The reaction order n of each chemical reaction is empirical and dimensionless. Although n can be predicted from transition state theory if the details of the reaction mechanism is known; it has been quantified for only a few minerals, and for those minerals only for a single mechanism. In all other cases, the default values for n are to a first approximation, unity. Uncertainties in values for n are currently the source of much uncertainty in the length of time to system equilibration computed in models of water-rock-interaction.

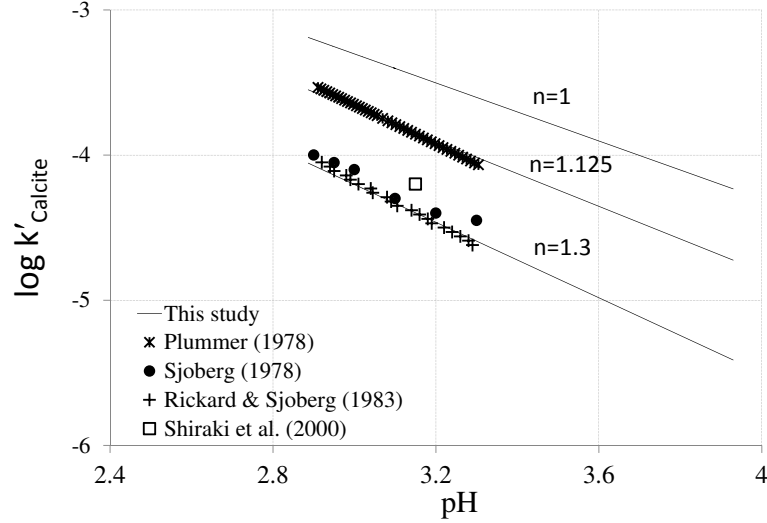


Figure 3.1: Log of dissolution rate of calcite in pure water ($m=0$) computed at 25°C as a function pH: Comparison of the results for different reaction orders (solid lines $n=1$, $n=1.125$, $n=1.3$) with respect to the pH and experimental data (symbols).

Reaction rates are known to be sensitive to the reaction order with respect to the pH of the system. We perform a sensitivity analysis with respect to the dissolution rate of calcite, k'_{calcite} , to highlight the effect of the reaction order, n , on the reaction rate. Log-log plots of dissolution rate (Eq. 3.11) as a function of pH allow one to derive n from the slope, $\log_{10} A$ and E from the intersection of the curve and y-axis ($\log_{10} k'_{\text{calcite}}$). Therefore, the variation of the pre-exponential factor and activation energy as a function of temperature is shown in the current study to result in a change in the intersection of the plots and y-axis. It can be seen that either increasing the temperature or decreasing the activation energy (for example through the use of catalysts) will result in an increase in the rate of reaction.

Figure 3.1 shows that the reaction order, n , with respect to the pH of the system has a significant effect on reaction rates (see also Eq. 3.11). It is found

that at low pH, dissolution rate of calcite increases with decreasing pH catalyzed by H^+ . The results for the dissolution rate of calcite as a function of the pH are also compared with experimental data from the literature in Fig. 3.1. Experimental results include the data obtained at a constant temperature and pressure of 25°C and 1 bar by Sjoberg (1978), Shiraki et al. (2000), Rickard and Sjoberg (1983). The data reported by Plummer et al. (1978) accounts for the effect of temperature and pressure. Figure 3.1 shows that k'_{calcite} obtained with the current model with $n = 1$ does not represent the experimental data. Differences between observed and computed reaction rates may occur because of variables beyond the scope of the geochemical modeling, such as variation in computed saturated mole fractions and pH of the system. To overcome this discrepancy, the free parameters such as reaction order and pre-exponential factor can be varied by means of sensitivity analysis to obtain agreement with experimental data. For instance, the reaction order, n , for dissolution rate of calcite can be changed to ≈ 1.3 or ≈ 1.125 in order to get the best fit with Rickard and Sjoberg (1983), and Plummer et al. (1978), respectively. We use $n \approx 1.125$ for our further investigation on the rate equations.

Figure 3.2 (a) depicts the variation of dissolution rate of calcite with pressure for various values of n , that are obtained from the sensitivity analysis in order to obtain agreement with experimental data, in pure water at 50°C. It is found that the dissolution rate increases with pressure and temperature and decreases with reaction order. Figure 3.2 (b) depicts the sensitivity of the dissolution rate of calcite in logarithmic scale (based 10) with respect to the reaction order and salinity of the solution at $T = 50^\circ\text{C}$, $P = 100$ bar. It is found that the dissolution rate of calcite

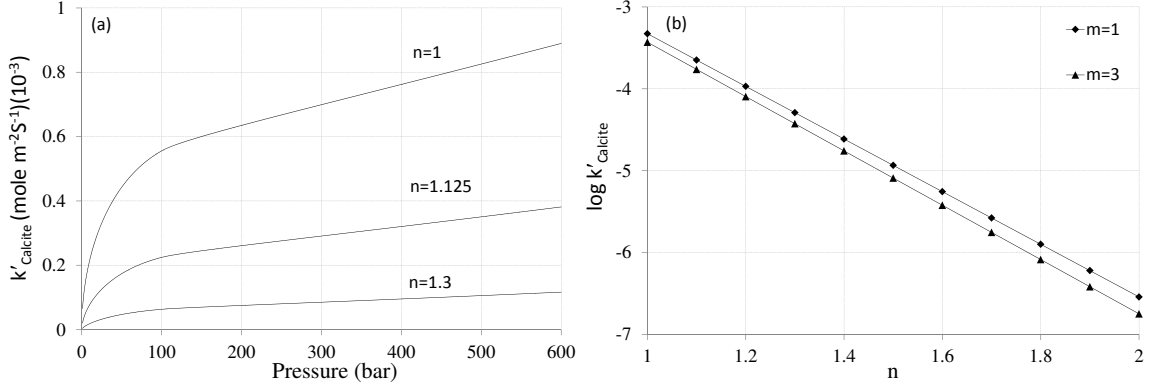


Figure 3.2: (a) Calculated dissolution rate of calcite with pressure based on different reaction order values in pure water ($m=0$) computed at 50°C . (b) Calculated log of dissolution rate of calcite with respect to reaction order, n , in saline water computed at various values of the molality of NaCl, m , $T= 50^{\circ}\text{C}$, $P= 100$ bar. The dissolution rates of calcite are found to decrease for higher value of reaction order and salinity. decreases as reaction order and salinity increase.

The lack of data over a wide range of temperatures may result in a large degree of uncertainty in the calculation of the reaction order n , pre-exponential factor A and Arrhenius activation energy E . Therefore, any rate equation that is to be used in geochemical computer modeling must contain only parameters that are available during program execution as variables or constants. To this end, the rate of chemical reactions with respect to the saturated concentration of CO_2 is determined as a function of temperature (T/K), pressure (P/bar) and salinity ($m/\text{molality}$), with a multi-parameter, non-linear regression of semi-empirical reaction rates. We use the following three-parameter, third order polynomial to represent the dissolution rates of calcite and anorthite,

$$k = a_0 + a_1T + a_2T^2 + a_3P + a_4P^2 + a_5m + a_6m^2 + a_7TP + a_8Tm + a_9Pm . \quad (3.12)$$

Table 3.1: Coefficients in Equation 3.12

| a_i | Calcite | Anorthite |
|-------|----------------------------|----------------------------|
| a_0 | 3.85100×10^{-4} | 1.77467×10^{-7} |
| a_1 | -2.54654×10^{-6} | -1.17231×10^{-9} |
| a_2 | 4.64099×10^{-9} | 2.05863×10^{-12} |
| a_3 | -3.56518×10^{-7} | -1.53164×10^{-10} |
| a_4 | -3.76945×10^{-11} | -1.10817×10^{-14} |
| a_5 | 4.38863×10^{-5} | 1.89898×10^{-8} |
| a_6 | 1.10690×10^{-6} | 4.28500×10^{-10} |
| a_7 | 1.53608×10^{-9} | 6.19685×10^{-13} |
| a_8 | -1.58641×10^{-7} | -6.58631×10^{-11} |
| a_9 | -1.94965×10^{-8} | -7.50258×10^{-12} |

The coefficients of the polynomial are determined by minimizing the error between k and k' with the method of multi-parameter, nonlinear regression (Lasdon et al., 1978). The error, ε , is defined as

$$\varepsilon = \sum_{i=1}^j [k'(P_i, T_i, m_i) - k]^2, \quad (3.13)$$

where, $k'(P_i, T_i, m_i)$ indicates reaction rates calculated from Eq. 3.11 at T_i , P_i and m_i for a total of $j = 4$ data points. The units of pressure, temperature and salinity in Eqs 3.12 and 3.13 are bar, Kelvin, and molality respectively. The error ε is interpreted as the residual sum of squares of the difference between k' and k . The system of equations obtained by minimizing the error given by Eq. 3.13 with respect to the coefficients a_i is solved by an iterative method based on the generalized reduced gradient (GRG) algorithm (Brown, 2001). The resulting coefficients a_i in

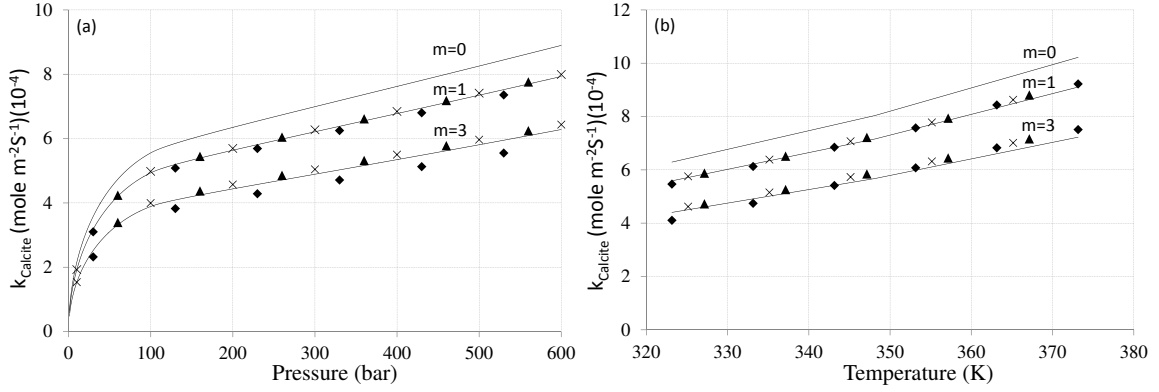


Figure 3.3: Calculated dissolution rate of calcite with pressure based on various activity coefficient models; Duan and Sun (2003) (solid lines), Rumpf et al. (1994) (crosses), Fournier (1985) (diamonds), Drummond (1981) (triangle) in saline water computed at (a) $T = 50^\circ\text{C}$ and pressures up to 600 bar, (b) $P = 100$ bar, various temperatures and molality of NaCl, m .

Eq. 3.12 are given in Table 3.1. The goodness-of-fit (R^2) is 0.997 and the error calculated from Eq. 3.13 is 1.7982×10^{-6} .

The rate of dissolution, k_{calcite} , obtained from Eq. 3.12 is shown in Figure 3.3 as a function of pressure and temperature for different values of salinity. With an increase in pressure, k_{calcite} increases rapidly for small values of P but then settles to a milder, constant rate of increase for larger values of the pressure, as shown in Fig. 3.3(a). In general, k_{calcite} increases with pressure and temperature but decreases with an increase in salinity. Dissolution rates obtained with different activity coefficient models are also shown with symbols. The difference in the rate of dissolution based on different activity coefficient models is observed in Fig. 3.3(a) to decrease in magnitude with an increase in salinity. However, k_{calcite} is somewhat less sensitive to the activity coefficient model compared with the solubility of CO_2 shown in Fig. 2. Even though the variation of k_{calcite} due to different activity coefficient

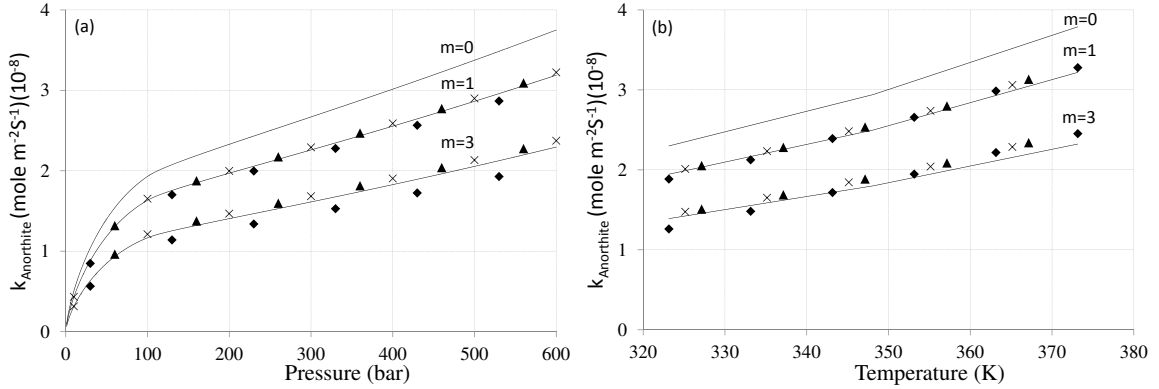


Figure 3.4: Calculated dissolution rate of anorthite with pressure based on various activity coefficient models; Duan and Sun (2003) (solid lines), Rumpf et al. (1994) (crosses), Fournier (1985) (diamonds), Drummond (1981) (triangle) in saline water computed at (a) $T = 50^\circ\text{C}$ and pressures up to 600 bar, (b) $P = 100$ bar, various temperatures and molality of NaCl, m .

models is relatively large for $m=3$, as shown in Fig. 3.3(a), the rate of increase of k_{calcite} remains unaffected by the various activity coefficient models. Figure 3.3(b) shows that the effect of the activity coefficient model on k_{calcite} as a function of temperature remains relatively weak for both levels of salinity.

Figure 3.4 depicts the dissolution rate of anorthite ($\text{CaAl}_2\text{Si}_2\text{O}_8$) as a function of pressure and temperature for various activity coefficients. Although the dissolution rate of anorthite, $k_{\text{anorthite}}$, is found to increase with pressure and temperature, it is quite small. In order to further continue the precipitation reaction, Ca^{2+} needs to dissolve out of anorthite. If one assumes anorthite to be the only source of Ca^{2+} , the rate-limiting factor is thus the dissolution rate of anorthite. To the best of our knowledge, the experimental data are not available for the same conditions considered here. Therefore, the results for dissolution rates of minerals can not be compared quantitatively with experiments. However, Hänchen et al. (2006) found

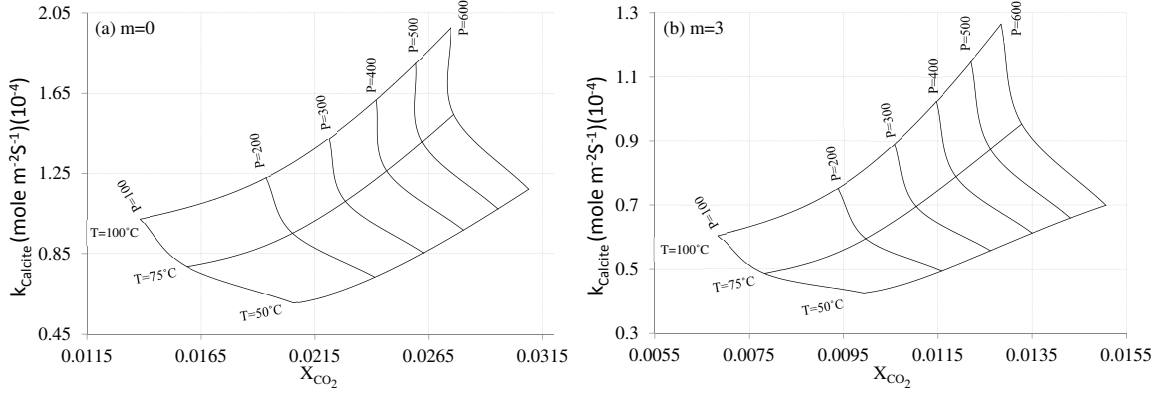


Figure 3.5: Calculated dissolution rate of calcite from Eq. 3.12 with pressure and temperature based on activity coefficient model of Duan and Sun (2003) in (a) pure water, (b) saline water with molality of NaCl, $m=3$.

that the dissolution rate of a different mineral such as olivine ($\text{Mg}_{1.82}\text{Fe}_{0.18}\text{SiO}_4$) reveals the similar trend in response to the changes in pH, pressure, and temperature of the system.

We employ the model of Duan and Sun (2003) for our further investigation on the rate equations. Because variation of dissolution rate of minerals is small with respect to the different activity coefficient models. The relationship between the dissolution rate of minerals k and the saturated mole fraction x_{CO_2} obtained from Eq. 3.12, is plotted in Fig. 3.5 and 3.6 as a function of temperature and pressure. The data is arranged as lines of constant temperature and constant pressure in the space of k and x_{CO_2} , as indicated in Fig 3.5 and 3.6. Each data point corresponds to a set of T and P values that range from $323^\circ\text{C} \leq T \leq 373^\circ\text{C}$ and $100 \text{ bar} \leq P \leq 600 \text{ bar}$, respectively. Figure 3.5 and 3.6 show that on constant temperatures lines, increasing pressures increase the dissolution rate and the saturated mole fraction of CO_2 . Along lines of constant pressure, increasing temperatures uniformly decrease

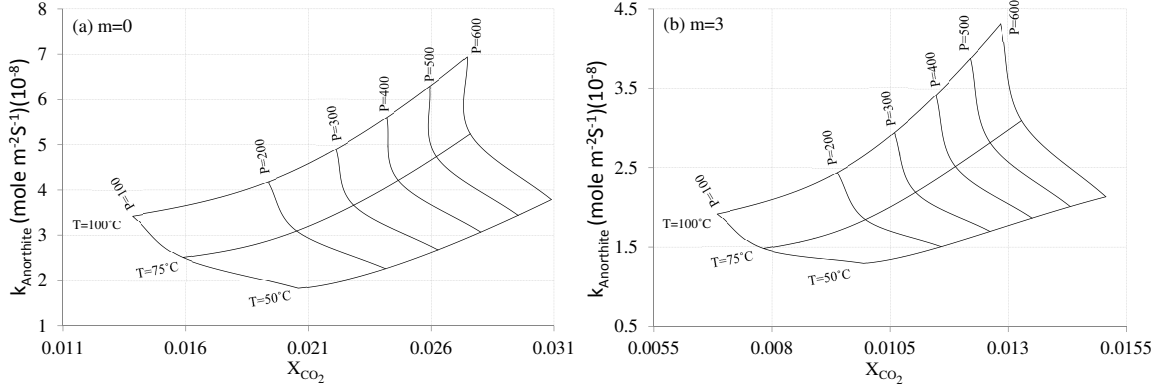


Figure 3.6: Calculated dissolution rate of anorthite from Eq. 3.12 with pressure and temperature based on activity coefficient model of Duan and Sun (2003) in (a) pure water, (b) saline water with molality of NaCl, $m=3$.

the mole fraction of CO_2 and increase the dissolution rate of calcite and anorthite.

Our method for calculating k will be used in the Chapter 5 to predict critical time of blockage for a single fracture.

3.4 Conclusions

The kinetics of the chemical reactions such as dissolution rates of calcite and anorthite are calculated in order to quantify the rate of mineral trapping of CO_2 . Our study confirms that the dissolution rate of anorthite is the rate-limiting process in the sequestration of CO_2 under the temperature and pressure conditions of typical saline aquifers, i.e. 50 to 100°C and up to 600 bar, respectively.

We have shown that the reaction order can be varied to obtained agreement with the experimental data. To this end, the reaction order for the dissolution rate of calcite is refined from 1 to 1.125 and 1.3 in order to get the best fit with Plummer et al. (1978) and Rickard and Sjöberg (1983), respectively. The reaction

order obtained with this method may have no physical meaning or relationship to the intrinsic reaction processes occurring on the molecular level.

The rate equation of the primary minerals in saturated solutions is determined as a function of only the parameters that are available as variables during program execution, such as pressure, temperature, and salinity, with the help of a multi-parameter nonlinear regression of semi-empirical data. We find that the proposed rate equation can reasonably reproduce reaction rates of minerals with new parameters that we obtain from sensitivity and multi-variant nonlinear regression studies.

Chapter 4

Effect of CO₂ Solubility on the Density of CO₂-H₂O and CO₂-H₂O-NaCl Solutions in Saline Aquifers

4.1 Introduction

A new model is proposed to find the density of saturated ternary solutions of H₂O-CO₂-NaCl in the temperature range of 50-100°C and pressures up to 600 bar. The model calculates the molar volumes of dissolved CO₂ from the density of saturated binary H₂O-CO₂ solutions. These densities are determined as a function of temperature and pressure from a regression of experimental data. The mole fractions of dissolved CO₂ in binary and ternary solutions are determined with a thermodynamic model based on the Redlich-Kwong equation of state. The liquid molar volumes of CO₂ are made to coincide with one solution branch of the Redlich-Kwong equation while retaining the solution branch associated with the molar volume of the gas phase. This allows the simultaneous calculation of both the gas and the liquid molar volumes. Using the modified equation of state, we predict the density of saturated ternary solutions and find good agreement with experimental data. Finally, we use our model to investigate the effects of temperature, pressure and salinity on the onset of buoyancy driven convection and wavelength of the finger-like structures during CO₂ sequestration.

Sequestration of carbon dioxide in deep saline aquifers can help prevent excessive buildup of CO₂ concentrations in the atmosphere (Orr, 2009). Carbon dioxide is typically introduced into an aquifer in a supercritical state. The density of the supercritical CO₂ is less than that of the brine. Therefore, upon injection, supercritical CO₂ flows upwards and collects below the impermeable cap rock and above the brine. At the interface between the supercritical CO₂ and brine, the CO₂ dissolves into the brine and forms a CO₂-brine solution whose density is greater than that of the underlying brine. This produces an unstable density stratification that promotes convective mixing and enhances the dissolution of supercritical CO₂ into brine (Ennis-King et al., 2003; Neufeld et al., 2010; Riaz and Cinar, 2013; Riaz et al., 2006). Because this convective mixing is driven by the density difference between the CO₂-brine solution and brine, the accurate determination of these densities is required to accurately model CO₂ sequestration.

Modeling CO₂ sequestration requires an accurate estimate of the density of a saturated brine-CO₂ solution in equilibrium with supercritical CO₂ (Meybodi and Hassanzadeh, 2013; Myint and Firoozabadi, 2013). The focus on saturated solutions is also motivated by the consideration that density changes upon dissolution of CO₂ are small (less than 6% in the temperature range of 50-100°C, pressures up to 600 bar, and salinities up to 6 molal NaCl) and that the density of an under-saturated solution varies linearly with mole fraction of CO₂ (Song et al., 2013). Hence, only the density and mole fraction of a saturated solution are needed for specifying boundary conditions at material interfaces between supercritical CO₂ and brine. The density of a saturated CO₂-brine solution depends on both the mole fraction and partial molar

volume of dissolved CO_2 (Akinfiyev and Diamond, 2010; Bodnar et al., 2013; Yan et al., 2011). Meanwhile, the mole fraction of dissolved CO_2 depends on the molar volume of CO_2 in the gas phase. Both the liquid and gas phase molar volumes of CO_2 are functions of temperature and pressure. Most previous characterizations of the liquid molar volume of dissolved CO_2 , however, are obtained for dilute solutions, and are often available as a function of temperature only (Enick and Klara, 1990; Moore et al., 1982; Teng et al., 1997; Yan et al., 2011). Furthermore, the direct experimental characterization of liquid molar volumes is difficult, and available data rarely correspond to the equilibrium state of supercritical CO_2 with respect to the liquid phase (Song et al., 2003a; Zhang et al., 2002).

The current study determines partial liquid molar volumes of CO_2 using the density of a saturated binary $\text{H}_2\text{O}-\text{CO}_2$ solution determined as a function of pressure and temperature through a multi-parameter nonlinear regression of experimental data. This density is used with a rigorous thermodynamic model of the gas molar volume to find the mole fraction of CO_2 in binary $\text{H}_2\text{O}-\text{CO}_2$ solutions. From this information, we obtain the molar volume of liquid CO_2 as a function of pressure and temperature. Our calculations indicate that the liquid molar volume varies substantially with pressure, and the behavior as a function of temperature is qualitatively different at different pressures.

The molar volume of CO_2 gas is characterized in this study using an improved form of the Redlich-Kwong equation of state (RK-EOS) proposed by Spycher and Pruess (2005, 2010b). The RK-EOS has two coefficients that are functions of temperature, and are obtained through regression of experimental data. This leads to

a more accurate prediction of gas molar volumes in comparison to previous forms of the RK-EOS with constant coefficients (Lemmon et al., 2003; Marini, 2007). We note that Duan et al. (1992) have proposed another method of calculating the gas molar volume of CO₂ through a virial-type equation of state containing fifteen adjustable parameters. We find, however, that the RK-EOS of Spycher and Pruess (2005) is sufficient for numerical simulation of the interaction of CO₂ and brine in porous media.

The RK-EOS of Spycher and Pruess (2010b) accurately provides the molar volume of CO₂ for the gas phase, but not the liquid phase. The difficulty arises because the coefficients in the RK-EOS of Spycher and Pruess (2010b) are optimized to match only the gas molar volumes. Engineering applications therefore find it difficult to pair liquid molar volumes with corresponding gas molar volumes at equilibrium to find the density of saturated solutions. In this study, we associate the liquid molar volume with a modified RK-EOS that yields the liquid molar volume as one of the solution branches, while retaining the solution branch related to the gas molar volumes. The molar volumes of CO₂ in liquid phase obtained from the modified RK-EOS are then used to study the influence of pressure, temperature and salinity on the density of saturated ternary H₂O-CO₂-NaCl solutions. These estimates show good agreement with the experimental data reported by Song et al. (2013).

The current study also investigates the influence of activity coefficients for aqueous CO₂ in NaCl solutions. Previous studies by Drummond (1981), Fournier (1985) and Rumpf et al. (1994) consider only the temperature dependence of the ac-

tivity coefficients. Duan and Sun (2003) show that the effect of salinity on solubility can be modeled more accurately by characterizing activity coefficients as a function of both temperature and pressure. Nomeli and Riaz (2014) study the effect of various activity coefficient models on reaction rates for the formation and dissolution of calcite. In this study, we further evaluate the effect of different activity coefficient models on the density of saturated solutions. We find that competing mechanisms related to the effects of temperature on the activity coefficients and fugacity produce counterintuitive behavior such that solubility does not always decrease with temperature.

An increase in solubility of CO_2 increases the density of the CO_2 -rich brine and drives the onset of buoyancy driven convection during CO_2 sequestration. We use our results for the density of CO_2 - H_2O and CO_2 - H_2O - NaCl solutions to investigate the effects of temperature, pressure and salinity on the time required for onset of buoyancy-driven convection and wavelength of the finger-like structures at onset of convection. We find that there is an optimal set of pressure, temperature and salinity which can minimize the onset time. We also observe that the wavelength decreases with pressure and salinity and increases with temperature.

This study is organized as follows: In section 4.2, we describe our method for calculating the liquid molar volume of dissolved CO_2 at equilibrium. In sections 4.3 and 4.4, we respectively quantify the partial molar volumes of H_2O and the mole fraction of dissolved CO_2 . Results from our new method for the partial molar volume of CO_2 in the liquid phase are presented in section 4.5. In section 4.6, new coefficients are derived for the Redlich-Kwong EOS equation of state to yield both

the liquid and gas partial molar volumes of CO₂ simultaneously. In sections 4.7 and 4.8, we investigate the effects of temperature, pressure and salinity on the density of ternary solutions, onset of buoyancy driven convection, and wavelength of the finger-like structures at onset of convection during CO₂ sequestration. Finally, we summarize our conclusions in section 4.9.

4.2 Modeling approach

When CO₂ dissolves into brine across a material interface at equilibrium, the density of the saturated solution is perturbed by the mole fraction and molar volume of dissolved CO₂. The density ρ_T of the saturated ternary H₂O-CO₂-NaCl solution can be modeled on the basis of mole fractions and molar volumes of H₂O, CO₂ and NaCl through the following relation,

$$\rho_T = \frac{\sum_{i=1}^3 x_i M_i}{\sum_{i=1}^3 x_i v_i} = \frac{\sum_{i=1}^3 x_i M_i}{\sum_{i=1}^3 x_i M_i / \rho_i}, \quad (4.1)$$

where, x_i , M_i , v_i and ρ_i are the mole fraction, molar mass, partial molar volume, and the density of the pure component i , respectively. The subscripts, $i = 1$, $i = 2$ and, $i = 3$ denote H₂O, CO₂, and NaCl, respectively, in this study.

We determine the partial molar volume $v_{2(l)}$ of liquid CO₂ from the density of saturated binary H₂O-CO₂ solutions for which experimental data is more readily available and contains less experimental uncertainties. For $x_3 = 0$, Eq. (4.1) gives the liquid molar volume as

$$v_{2(l)} = \frac{(1 - x_2)M_1 + x_2M_2 - \rho_B(1 - x_2)M_1/\rho_1}{\rho_B x_2}, \quad (4.2)$$

Table 4.1: Coefficients in Equation 4.3

| | Non-linear Regression | Linear Regression |
|-------|---------------------------|---------------------------|
| a_0 | 1.07719145 | 1.17994981 |
| a_1 | 0 | -5.77750×10^{-4} |
| a_2 | 1.807316×10^{-4} | 7.371614×10^{-5} |
| a_3 | -8.35073×10^{-7} | 0 |
| a_4 | -9.59081×10^{-8} | 0 |
| a_5 | -1.85537×10^{-7} | 0 |

where ρ_B denotes the density of the saturated binary solution. Given ρ_B , the density ρ_1 of water and the mole fraction x_2 in saturated solutions, the molar volume $v_{2(l)}$ of liquid CO₂ can be obtained from Eq. (4.2). This molar volume can then be used to find the density ρ_T of saturated ternary solutions from Eq. (4.1).

Available experimental data for the density of binary H₂O-CO₂ solutions is summarized in Table 4.2. Most data is not applicable to CO₂ sequestration because it does not correspond to the saturated state of dissolved CO₂. We therefore use data reported by Li et al. (2011), Song et al. (2005), Bando et al. (2004), and Teng et al. (1997), for the density of saturated solutions. This data is plotted in Fig. 4.1 as a function of pressure at two different values of temperature. In general, the density of a saturated binary solution is observed to increase with pressure. This occurs because higher pressures increase the saturated mole fraction of dissolved CO₂ (Spycher and Pruess, 2010b), which increases solution density. Comparison of densities in Figs. 4.1 (a) and (b) shows that higher temperatures tend to decrease the density. This occurs because high temperatures lower the saturated mole fraction of dissolved CO₂, which results in a lower density (Marini, 2007).

Table 4.2: Experimental studies performed to determine the density of the CO₂-H₂O solution. The last column gives the range of concentrations, as mole fraction $x(\text{CO}_2)$, at which the density was determined.

| Authors | T/K | P/bar | Mole fraction of CO ₂ /% |
|--------------------------------|-----------------|------------------|-------------------------------------|
| Li et al. (2011) | 273 - 573 | 0.001 - 1000 | 0 - saturated values |
| Song et al. (2005) | 276, 283 | 40 - 120 | 0 - saturated values |
| Bando et al. (2004) | 303 - 333 | 100 - 200 | 0 - saturated values |
| Song et al. (2003a,b) | 273.25 - 284.15 | 50 - 125.0 | 0 - 0.61 |
| Zhang et al. (2002) | 308.15 | 77.52 - 124.84 | 99.7 |
| Blencoe et al. (2001) | 573.15 | 74.4 - 999.3 | 0 - 0.9 |
| Teng et al. (1997) | 278 - 293 | 64.4 - 294.9 | 0 - saturated values |
| Seitz and Blencoe (1997) | 573.15 - 623.15 | 999.3 | 0.1 - 0.9 |
| Teng and Yamasaki (1998) | 278 - 293 | 64.4 - 294.9 | 2.50 - 3.49 |
| Wood et al. (1996) | 298.15 - 633.41 | 10 - 350 | 0.279 - 0.332 |
| Fenghour et al. (1996) | 415.36 - 644.78 | 58.84 - 279.64 | 0.0612 - 0.7913 |
| Ohsumi et al. (1992) | 276.15 | 347.54 | 0.1798 - 0.6294 |
| King et al. (1992) | 288.15 - 298.15 | 60.8 - 243.2 | 2.445 - 3.070 |
| Zhang and Frantz (1992) | 519.95 - 634.45 | * | 5.5 - 16.5 |
| Crovetto and Wood (1992) | 622.75 - 642.70 | 196.4 - 281.3 | 0.48 - 0.8745 |
| Sterner and Bodnar (1991) | 494.15 - 608.15 | 487 - 3100 | 0.1234 - 0.7473 |
| Nighswander et al. (1989) | 352.85 - 471.25 | 20.4 - 102.1 | 0.22 - 1.66 |
| Patel and Eubank (1988) | 323.15 - 498.15 | 0.855 - 100.237 | 0.02 - 0.5 |
| Patel et al. (1987) | 323.15 - 498.15 | 1 - 100 | 0.5 - 0.98 |
| Wormald et al. (1986) | 473.2 - 623.2 | 10 - 120 | 0.5 |
| Zakirov (1984) | 573.15 | 50 - 1800 | 0.3 - 0.77 |
| Parkinson and De Nevers (1969) | 278.1 - 313.7 | 10.342 - 344.744 | 0.1 - 2.2 |
| Ellis and Golding (1963) | 504.15 - 643.15 | 47.91 - 254.43 | ** |
| Ellis (1959b) | 387.15 - 621.15 | 5 - 164 | 3.90, 6.27, 84.02 |

*Pressures are not reported, but can be calculated from their empirical formulations,
**concentrations are not directly reported, but can be calculated from the report.

The experimental data presented in Fig. 4.1 suggests that we approximate ρ_B using the following two-parameter, second order polynomial,

$$\rho_B = a_0 + a_1T + a_2P + a_3T^2 + a_4P^2 + a_5TP \ . \quad (4.3)$$

The coefficients of the polynomial are determined by minimizing the error between ρ_B and experimental data points $\tilde{\rho}_B$ with the method of multi-parameter, nonlinear regression (Lasdon et al., 1978). The error, ε , is defined as

$$\varepsilon = \sum_{i=1}^n [\tilde{\rho}_B(P_i, T_i) - \rho_B]^2 \ , \quad (4.4)$$

where, $\tilde{\rho}_B(P_i, T_i)$ indicates discrete experimental data at T_i and P_i for a total of n data points. The units of pressure and temperature in Eqs 4.3 and 4.4 are bar and Kelvin, respectively. The error ε is interpreted as the residual sum of squares of the difference between experimental data points and ρ_B . The system of equations obtained by minimizing the error given by Eq. (4.4) with respect to the coefficients a_i is solved by an iterative method based on the generalized reduced gradient (GRG) algorithm (Brown, 2001). The resulting coefficients a_i in Eq. (4.3) are given in Table 4.1.

Table 4.3: Residual sum of squares, RSS

| Authors | ε |
|------------------------------------|--------------------------|
| This study (Non-linear Regression) | 5.28780×10^{-4} |
| Duan et al. (2008) | 1.00059×10^{-3} |
| This study (Linear Regression) | 4.66673×10^{-2} |
| Spycher and Pruess (2010b) | 5.12492×10^{-2} |

Fig. 4.1 shows ρ_B , calculated from Eq. (4.3) (solid line) as a function of pressure for $T= 25^\circ\text{C}$ (panel a) and $T= 65^\circ\text{C}$ (panel b). Compared with experimental data

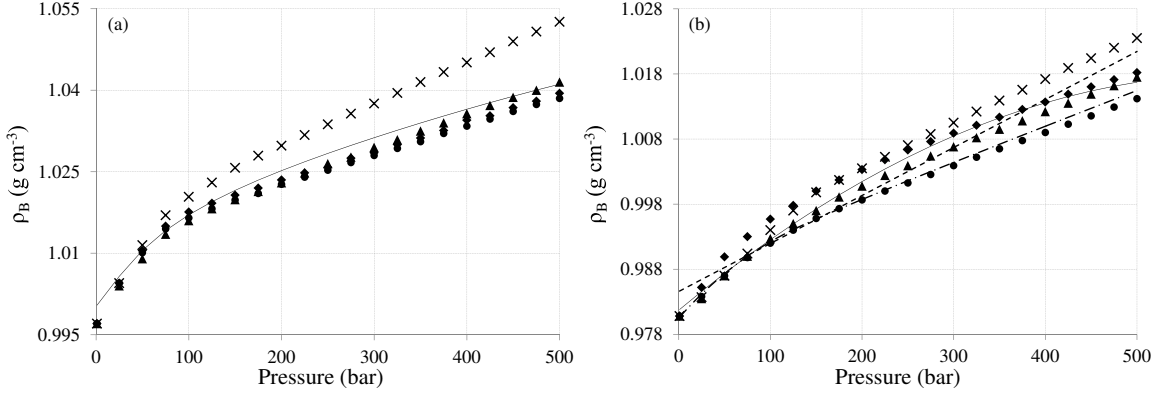


Figure 4.1: Experimental data for ρ_B reported by Teng et al. (1997) (crosses), Bando et al. (2004) (triangles), Song et al. (2005) (diamonds) and Li et al. (2011) (solid dots) for the temperatures (a) 25°C and (b) 65°C. Solid lines show ρ_B obtained from Eq. (4.3). Results from the model of Duan et al. (2008) are shown in panel (b) using a dash-dotted line. The dashed line in panel (b) shows our results obtained with linear regression.

at $T=25^\circ\text{C}$, ρ_B follows the data sets of Bando et al. (2004), Song et al. (2005) and Li et al. (2011) more closely because the data set of Teng et al. (1997) deviates for higher pressures. In the case of $T=65^\circ\text{C}$ (panel b), the experimental data are more evenly distributed, and hence ρ_B provides a good match with all data sets. Fig. 4.1(b) also plots ρ_B based on the model of Duan et al. (2008) (dash-dotted line). Their model for liquid molar volumes is used in Eq. (4.2) along with the mole fraction obtained from the Redlich-Kwong equation described later in sections 4.4 and 4.6 to obtain ρ_B . Estimates from the model of Duan et al. (2008) are close to our results based on Eq. (4.3). Fig. 4.1(b) also shows the density ρ_B based on a linear regression (dashed line). According to Table 4.3, ρ_B based on the non-linear regression model provides a more accurate representation of experimental data compared with the linear regression, the model of Duan et al. (2008) and the model of Spycher and

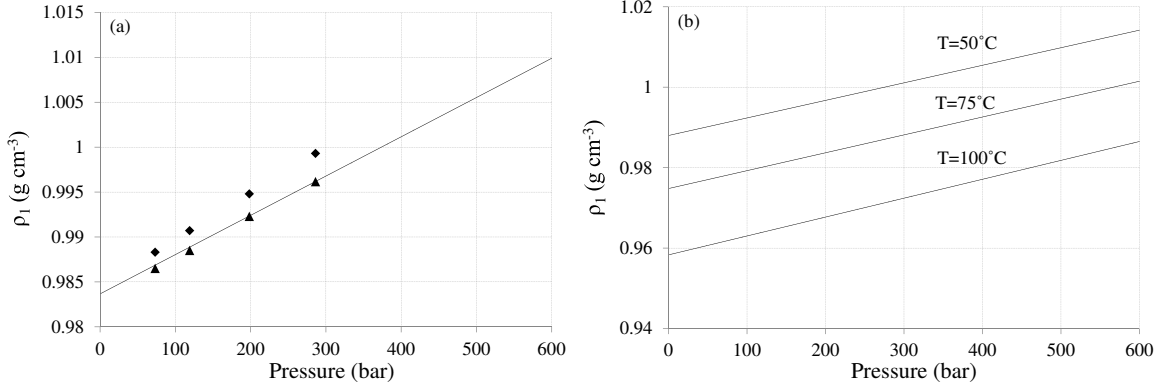


Figure 4.2: (a) Density of pure water at T=65°C based on the EOS model of Kell (1975) (solid line) that is used in the current study. Density values reported by Li et al. (2004) and those recommended by NIST are shown with symbols, (diamonds) and (triangles), respectively. (b) Variation of H₂O density with temperature based on the EOS of Kell (1975)

Pruess (2010b). The value of ρ_B based on nonlinear regression will therefore be used in Eq. (4.2) to estimate the liquid molar volume.

4.3 Molar volume of H₂O and density ratio

The density, ρ_1 , and molar volume, $v_1 = M_1/\rho_1$, of H₂O are required to calculate the density, ρ_T given by Eq. (4.1). Because CO₂-brine solutions consist mostly of H₂O (Nomeli and Riaz, 2014; Spycher and Pruess, 2010b), small errors in estimating ρ_1 can introduce substantial errors in the estimation of ρ_T . Table 2.1 in IAPWS-95 clearly shows that most correlations for the thermodynamic properties of H₂O found in the literature cover a portion of the fluid region in the phase space that is not suitable for CO₂ sequestration (Wagner and Pruss, 2002).

Moreover, in the report of Wagner and Pruss, 2002, Figure 7.2 illustrates

that, in contrast to IAPS-84 and Hill's equation of state, IAPWS-95 is able to represent the density data of Kell (1975) to within their experimental uncertainty $\Delta\rho = \pm 0.0004\%$ at $T = 277$ K to $\Delta\rho = \pm 0.0012\%$ at $T = 423$ K without significant oscillations. We therefore use the EOS of Kell (1975) to find the densities of pure water that are valid over a wider range of temperatures and pressures. Fig. 4.2 demonstrates that ρ_1 calculated from the EOS of Kell (1975) (solid line) approximates those recommended by NIST (National Institute of Standards and Technology) (diamonds) with an average deviation of 2×10^{-5} , and also shows good agreement with the experimental data of Li et al. (2004) (triangles). Note that the densities recommended by NIST are also accepted by the International Association for the Properties of Water and Steam (Wagner and Pruss, 2002).

Fig. 4.3(a) shows the relative density difference $(\rho_B/\rho_1 - 1)$ between a binary saturated solution and pure H_2O as a function of pressure for $T = 65^\circ\text{C}$. Values of ρ_B used in the calculation of $(\rho_B/\rho_1 - 1)$ are based on experimental data points and various models. The density ρ_1 is based on the EOS of Kell (1975). Fig. 4.3 indicates that binary solutions are heavier than pure water for all cases, i.e. $(\rho_B/\rho_1 - 1) > 0$, as expected. With increasing pressure, $(\rho_B/\rho_1 - 1)$ follows more or less the same trend as ρ_B shown in Fig. 4.1. This is because the density of pure water increases linearly with pressure, as shown in Fig. 4.2. Fig. 4.3(a) also shows, however, that $(\rho_B/\rho_1 - 1)$ based on experimental data is relatively more sensitive to experimental uncertainty compared with the experimental data for ρ_B shown in Fig. 4.1.

Fig. 4.3(a) demonstrates that $(\rho_B/\rho_1 - 1)$ based on non-linear regression (solid line) better approximates the qualitative trends observed experimentally compared

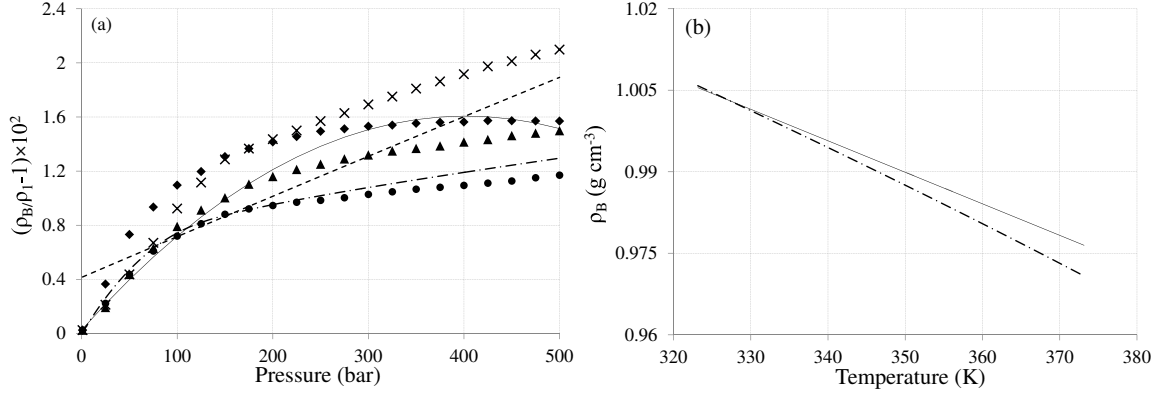


Figure 4.3: (a) Relative density difference, $(\rho_B/\rho_1 - 1)$, as a function of pressure at 65°C. Lines indicate the relative density computed from the non-linear regression Eq. (4.3) (solid line), linear regression (dashed line) and the model of Duan et al. (2008) (dash-dotted line). Symbols represent $(\rho_B/\rho_1 - 1)$ based on the experimental data of Teng et al. (1997) (crosses), Bando et al. (2004) (triangles), Song et al. (2005) (diamonds) and Li et al. (2011) (circles). The density of pure water, ρ_1 , is based on the EOS of Kell (1975). (b) ρ_B based on the non-linear regression (solid line) and the model of Duan et al. (2008) (dash-dotted line) as a function of temperature at 150 bar.

with the linear regression (dashed line). We observe that the model of Duan et al. (2008) (dash-dotted line) closely follows the experimental data of Li et al. (2011) (solid dots). Note that our calculation of $(\rho_B/\rho_1 - 1)$ based on nonlinear regression shows a non-monotonic behavior. This is a mathematical artifact of the regression that seeks a best fit between scattered data sets, particularly at high pressures where the data of Teng et al. (1997) (crosses) deviates from the other data sets. As future experimental data becomes available, the non-monotonic behavior of our non-linear regression will likely be reduced or eliminated. Fig. 4.3(b) plots ρ_B as a function of temperature at 150 bar when ρ_B is obtained from the non-linear regression (solid

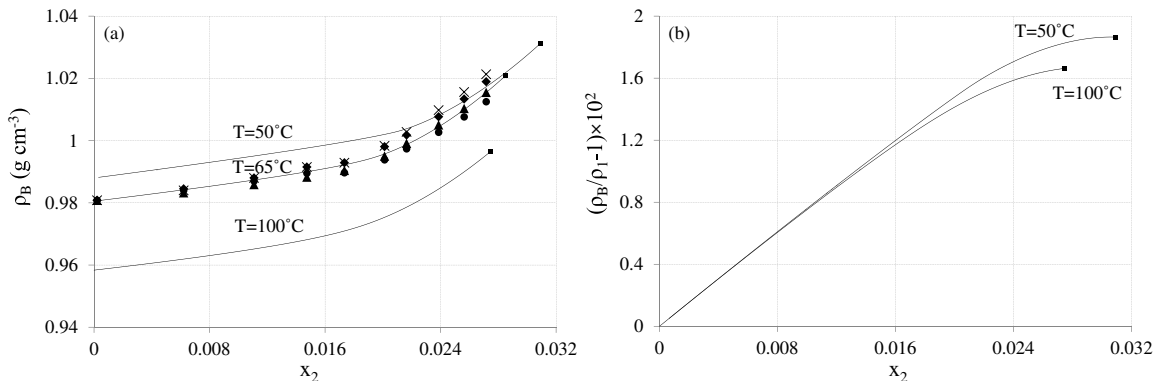


Figure 4.4: (a) Density of the saturated binary solution, ρ_B , as a function of saturated mole fraction of dissolved CO_2 . Symbols denote liquid molar volume based on experimental data for density noted in Fig. 4.1. The solid squares on the constant temperature lines correspond to the maximum mole fraction of CO_2 at 600 bar. (b) Relative density of the saturated binary solution, ρ_B , with respect to the density of pure water, ρ_1 .

line) and the model of Duan et al. (2008) (dash-dotted line). A qualitatively similar behavior is predicted by both calculations, with better quantitative agreement at lower temperatures.

4.4 Saturated mole fraction of dissolved CO_2

The mole fraction of dissolved CO_2 is needed to determine the density of the ternary solution ρ_T and the partial molar volume $v_{2(l)}$ given by Eqs. 4.1 and 4.2, respectively. In the following, we describe the method based on RK-EOS for determining the mole fraction of CO_2 corresponding to the saturated state of the solution. The equilibrium partitioning of supercritical CO_2 with respect to a dissolved

aqueous phase is described by



Assuming brine to be made up of H₂O and NaCl, the mole fraction of CO_{2(aq)} in brine can be defined as

$$x_2 = \frac{m_{\text{CO}_2}}{m_{\text{CO}_2} + m_{\text{H}_2\text{O}} + 2 m_{\text{NaCl}}} , \quad (4.6)$$

where m_{CO_2} , $m_{\text{H}_2\text{O}}$ and m_{NaCl} denote the molality of CO₂, H₂O and NaCl, respectively, in the solution. The factor of 2 for m_{NaCl} accounts for the complete dissociation of dissolved NaCl into Na⁺ and Cl⁻ ions. The molality of CO₂ can be expressed as the ratio $m_{\text{CO}_2} = a_{\text{CO}_2}/\gamma_{\text{CO}_2}$ where a_{CO_2} is the activity of CO₂ in the solution and γ_{CO_2} is the activity coefficient. The activity a_{CO_2} of dissolved CO₂ and the fugacity f_{CO_2} in the CO₂ rich phase are related through the equilibrium constant, $K = f_{\text{CO}_2}/a_{\text{CO}_2}$. Using these relations, the mole fraction of CO₂ in Eq. (4.6) can be expressed as

$$x_2 = \frac{f_{\text{CO}_2}}{f_{\text{CO}_2} + (m_{\text{H}_2\text{O}} + 2 m_{\text{NaCl}}) K \gamma_{\text{CO}_2}} . \quad (4.7)$$

We determine the fugacity f_{CO_2} from the following relationship,

$$f_{\text{CO}_2} = \phi y_{\text{CO}_2} P , \quad (4.8)$$

where ϕ and y_{CO_2} are the fugacity coefficient and mole fraction, respectively, of CO₂ in the supercritical phase. In regions of the aquifer occupied by supercritical CO₂, we set $y_{\text{CO}_2} = 1$ because the amount of H₂O in these regions is negligible for $T \leq 100^\circ\text{C}$. (Spycher and Pruess, 2010b). We compute ϕ from the following equation,

$$\ln \phi = \ln \left(\frac{v_{2(g)}^{\text{RK}}}{v_{2(g)}^{\text{RK}} - S} \right) + \frac{S}{v_{2(g)}^{\text{RK}} - S} - \frac{3Q}{\text{SRT}^{3/2}} \left[\ln \left(\frac{v_{2(g)}^{\text{RK}} + S}{v_{2(g)}^{\text{RK}}} \right) - \frac{S}{3(v_{2(g)}^{\text{RK}} + S)} \right] - \ln Z \quad (4.9)$$

where $v_{2(g)}^{\text{RK}}$ is the maximum root of the RK-EOS, which corresponds to the molar volume of CO_2 in gas phase, $Z = Pv_{2(g)}^{\text{RK}}/RT$ is the compressibility factor of supercritical CO_2 , and Q and S are coefficients given in Table 4.4 for the temperature range of 283 – 380 K (Spycher and Pruess, 2010a). Finally, we use the model for K given by Marini (2007) and Spycher and Pruess (2010b), which is valid for the supercritical range of temperatures and pressures. The calculation of the gas molar volume $v_{2(g)}^{\text{RK}}$ is described later in section 4.6.

Based on the calculated value of x_2 , we predict the dependence of ρ_B on x_2 , as shown in Fig. 4.4(a). Constant temperature lines extend up to the maximum pressure of 600 bar computed in this study. We emphasize that ρ_B is the density of a saturated solution at its corresponding saturation value of x_2 . This value of ρ_B should not be confused with the density of under-saturated solutions for arbitrary values of x_2 that is often reported in the literature. Fig. 4.4(a) shows that ρ_B increases with the mole fraction of dissolved CO_2 . The experimental data for the density of saturated binary solutions at 65°C, when plotted as a function of x_2 , is observed to be well-represented by our model. The relative density difference $(\rho_B/\rho_1 - 1)$ is plotted in Fig. 4.4(b). It is relatively less sensitive to changes in temperature except at larger values of the mole fraction. The basis for the increase in solution density with x_2 can be understood in terms of the size of a CO_2 molecule with higher molecular weight of 44.01 compared to that of pure water with molecular weight of 18.0152. Consequently, the total molecular density of $\text{H}_2\text{O}-\text{CO}_2$ solution becomes greater than that of pure water, which increases the solution density.

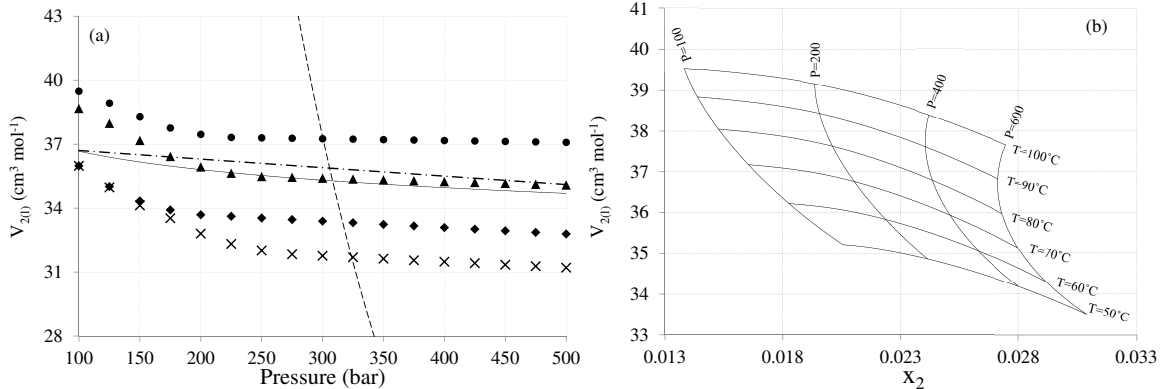


Figure 4.5: (a) Partial molar volume of dissolved CO₂ in the liquid phase at 65°C. Lines represent, this study (solid line), the model of Duan et al. (2008) (dash-dotted line) and RK-EOS (dashed line). Symbols denote liquid molar volume based on experimental data for density noted in Fig. 4.1 (b) The relationship between the liquid molar volume $v_{2(l)}$ and the saturated mole fraction x_2 obtained from Eq. (4.7).

4.5 Partial molar volume of CO₂ in saturated solutions

Fig. 4.5(a) illustrates the variation of $v_{2(l)}$ with pressure for $T = 65^\circ\text{C}$. The solid line shows our results for $v_{2(l)}$ given by Eq. (4.2), with x_2 obtained from Eq. (4.7), ρ_B from Eq. (4.3), and ρ_1 from the EOS of Kell (1975). For comparison, we also show results for $v_{2(l)}$ obtained with the methods of Duan et al. (2008) (dash-dotted line) and experimental data (symbols) for ρ_B shown in Fig. 4.1. From the experimental results for $v_{2(l)}$, we observe that the liquid molar volume initially decreases rapidly with increasing pressure, after which $v_{2(l)}$ appears to asymptote to nearly constant values. The $v_{2(l)}$ obtained from our method provides a slightly better representation of these trends than the model of Duan et al. (2008). Both models predict a monotonic decrease of $v_{2(l)}$ over the entire range of pressures. Fig. 4.5(a)

indicates that the variation in the experimental data for ρ_B is amplified in the calculation of $v_{2(l)}$. Hence, a level of uncertainty exists no matter which method is used. The strength of our approach is that $v_{2(l)}$ is based on experimentally measured densities of saturated binary H₂O-CO₂ solutions that are easier to obtain than direct experimental measurement of $v_{2(l)}$. Consequently, with our approach the estimate of $v_{2(l)}$ can be systematically improved as future experimental data for ρ_B are reported.

The relationship between the liquid molar volume $v_{2(l)}$ and the saturated mole fraction x_2 obtained from Eq. (4.7), is plotted in Fig. 4.5(b) as a function of temperature and pressure. The data is arranged as lines of constant temperature and constant pressure in the space of $v_{2(l)}$ and x_2 . Each data point corresponds to a set of T and P values that range from $323^\circ\text{C} \leq T \leq 373^\circ\text{C}$ and $100 \text{ bar} \leq P \leq 600 \text{ bar}$, respectively. On lines of constant temperature, increasing pressures increase the mole fraction and decrease the molar volume. Along lines of constant pressure, increasing temperatures at low pressures uniformly decrease the mole fraction and increase the molar volume. For high pressures, on the other hand, an increase in temperature along lines of constant pressure leads to a non-monotonic change in the mole fraction, while the molar volume increases uniformly. This occurs because competing mechanisms related to the effects of temperature on the activity coefficients and fugacity produce counterintuitive behavior such that solubility does not always decrease with temperature. This characterization of the molar volume related to the saturated mole fraction of dissolved CO₂ clearly shows that the molar volume is a function of pressure, a condition that is often ignored in previous calculations of the molar volume. Our method for calculating $v_{2(l)}$ will be used in section 4.7 to

Table 4.4: Coefficients in Equation 4.10.

| (T, P) | Q | | S | |
|------------|---------------------|---------------------|------|--------|
| | old | new | old | new |
| (323, 50) | 6.206×10^7 | 5.602×10^7 | 27.8 | 19.230 |
| (323, 100) | 6.206×10^7 | 4.814×10^7 | 27.8 | 17.730 |
| (323, 300) | 6.206×10^7 | 1.286×10^7 | 27.8 | 3.013 |
| (348, 50) | 6.103×10^7 | 5.343×10^7 | 27.8 | 17.450 |
| (348, 100) | 6.103×10^7 | 4.970×10^7 | 27.8 | 16.930 |
| (348, 300) | 6.103×10^7 | 1.359×10^6 | 27.8 | 1.427 |
| (373, 50) | 6.000×10^7 | 4.998×10^7 | 27.8 | 14.810 |
| (373, 100) | 6.000×10^7 | 4.656×10^7 | 27.8 | 14.350 |
| (373, 300) | 6.000×10^7 | 1.144×10^6 | 27.8 | -3.516 |

predict the density of ternary solutions.

4.6 Modified Redlich-Kwong EOS

To obtain the molar volume of CO₂ in both gas and liquid phases, we modify the following RK-EOS of Spycher and Pruess (2010b),

$$v^3 - \frac{RT}{P}v^2 - \left(\frac{RTS}{P} - \frac{Q}{T^{1/2}P} + S^2 \right) v - \frac{QS}{T^{1/2}P} = 0, \quad (4.10)$$

where Q and S are adjustable coefficients. The units of pressure and temperature are bar and Kelvin, respectively. The molar volume is denoted by v , and R is the universal gas constant. In the supercritical region of CO₂ ($T > 31^\circ\text{C}$ and $P > 74$ bar) this cubic equation yields one root above the critical point and another below the critical point. It is generally understood that the maximum root $v_{2(g)}^{\text{RK}}$ gives the molar volume of CO₂ in gas phase and the minimum root $v_{2(l)}^{\text{RK}}$ is associated with

the molar volume of CO₂ in liquid phase (Marini, 2007). The dashed line in Fig. 4.5(a) shows that the liquid molar volume obtained in this manner from the RK-EOS (Eq. (4.10)) provides a poor representation of experimental data. We therefore modify the coefficients Q and S so that $v_{2(l)}^{\text{RK}}$ coincides with $v_{2(l)}$ based on our new method. Q and S are thermodynamically consistent. Because the molar volume of CO₂ in the gas phase computed from the modified RK-EOS are the same as what we get from the current RK-EOS which is based on statistical thermodynamics and mixing rules.

The new liquid molar volume of CO₂ from Eq. (4.2) and the original molar volume $v_{2(g)}^{\text{RK}}$ in the gas phase are used to form a cubic equation,

$$(v - v_{2(g)}^{\text{RK}})(v - v_{2(l)})(v - v_3^{\text{RK}}) = 0 , \quad (4.11)$$

where v_3^{RK} is the third root that is not associated with any physical quantity. By equating Eq. (4.11) with Eq. (4.10), we obtain the following system of equations,

$$\begin{aligned} \frac{RT}{P} &= v_{2(g)}^{\text{RK}} + v_{2(l)} + v_3^{\text{RK}} , \\ \frac{RTS}{P} - \frac{Q}{T^{0.5}P} + S^2 &= -(v_{2(l)}v_3^{\text{RK}} + v_{2(g)}^{\text{RK}}v_3^{\text{RK}} + v_{2(g)}^{\text{RK}}v_{2(l)}), \\ \frac{QS}{T^{0.5}P} &= v_{2(g)}^{\text{RK}}v_{2(l)}v_3^{\text{RK}} , \end{aligned} \quad (4.12)$$

for the unknowns, v_3^{RK} , Q and S. The new and the old coefficients of RK-EOS are given in Table 4.4. The new coefficients NC of RK-EOS at intermediate T and P can be obtained from the following equation:

$$\text{NC} = a_0 + a_1T + a_2P + a_3T^2 + a_4P^2 + a_5TP . \quad (4.13)$$

The resulting coefficients a_i in Eq. (4.13) are given in Table 4.5. Fig. 4.6(a)

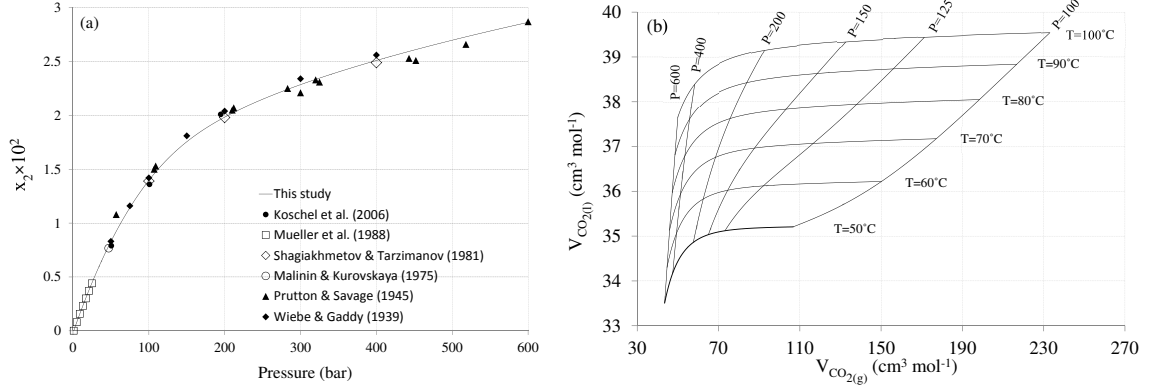


Figure 4.6: (a) Mole fraction of dissolved CO₂ as a function of pressure at 100°C. The residual sum of squares of the difference between experimental data points and x_2 is 6.811×10^{-6} . The mole fraction x_2 , obtained from the modified Redlich-Kwong EOS agrees well with experimental data for saturated binary solutions. (b) The relationship between gas and liquid molar volumes as a function of temperature and pressure predicted by the modified Redlich-Kwong EOS.

depicts the mole fraction x_2 at 100°C given by Eq. (4.7), where the gas molar volumes are obtained from Eq. (4.9) with new values of Q and S (modified RK-EOS). The results show excellent agreement with experimental data. Fig. 4.6(b) plots the phase space spanned by $v_{2(l)}$ and $v_{2(g)}^{RK}$ as a function of temperature and pressure obtained with the modified RK-EOS. We observe that $v_{2(l)}$ increases rapidly at high pressures along lines of constant low temperatures and saturates at lower pressures. For constant values of higher temperatures, the change is more gradual. Fig. 4.6(b) further indicates that $v_{2(g)}^{RK}$ increases more rapidly with temperature along lines of constant low pressures but at progressively lower rates along lines of constant high pressures.

Table 4.5: Coefficients in Equation 4.13

| | Q | S |
|-------|------------------------|---------------------------|
| a_0 | -2.01607×10^8 | -1.20487×10^2 |
| a_1 | 1.58614×10^6 | 8.66449×10^{-1} |
| a_2 | -2.41777×10^3 | -1.35087×10^{-3} |
| a_3 | -3.09568×10^5 | -1.63079×10^{-2} |
| a_4 | -2.52788×10^2 | -2.29424×10^{-4} |
| a_5 | 6.75334×10^2 | 9.41105×10^{-5} |

4.7 Density of ternary solutions

Our procedure for calculating ρ_T may be summarized in the following manner. For a given temperature, pressure and salinity, we first compute the molar volume v_1 of H₂O from Kell’s EOS (Kell, 1975). Next, we compute the mole fraction x_2 of dissolved CO₂ as described in section 4.4. Next, we compute $v_{2(l)}$ as described in section 4.5. Finally, we calculate the molar volume of NaCl using the model suggested by Rogers and Pitzer (1982),

$$v_3 = \left(\frac{1000 + m_3 M_3}{\rho' m_3} \right) - \left(\frac{1000}{\rho_1 m_3} \right), \quad (4.14)$$

where ρ' and ρ_1 are the densities of the H₂O-NaCl solution and H₂O, respectively. We also investigate the influence of four different models for the activity coefficient γ_{CO_2} of dissolved CO₂ in saline solutions. The models considered are those of (i) Fournier (1985), (ii) Duan and Sun (2003), (iii) Rumpf et al. (1994), and (iv) Drummond (1981).

In order to test the validity of our model, we compare our results for ρ_T with the experimental data of Song et al. (2013) (squares) and the model of Akinfiev and

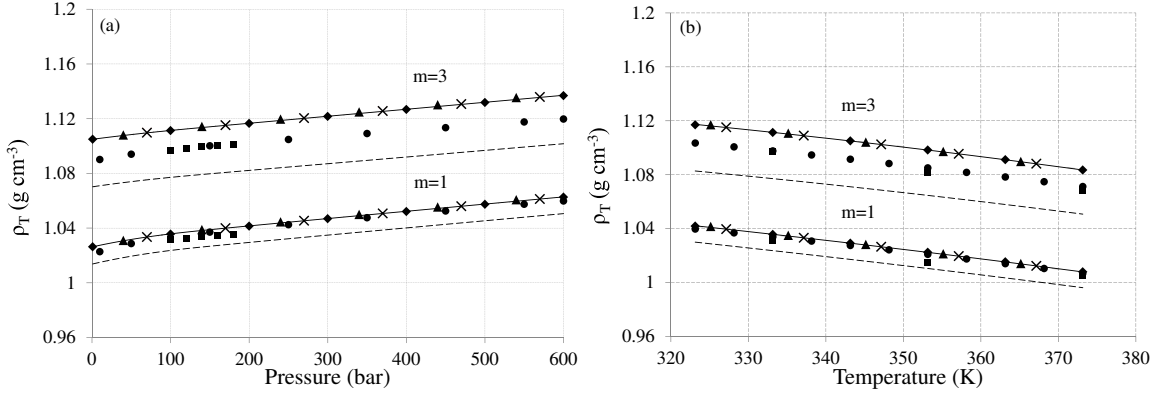


Figure 4.7: Density of ternary solution ρ_T at (a) 60°C and (b) 100 bar for two different values of NaCl molality. Our calculations of ρ_T are based on the activity coefficient models of Duan and Sun (2003) (line), Fournier (1985) (diamonds), and Drummond (1981) (crosses), Rumpf et al. (1994) (triangles). We compare our calculations of ρ_T with data of Song et al. (2013) (squares), Akinfiev and Diamond (2010) (circles), and Li et al. (2011) (dashed lines).

Diamond (2010) (circles), and Li et al. (2011) (dashed lines) for ternary solutions of $\text{H}_2\text{O}-\text{CO}_2-\text{NaCl}$. Because Song et al. (2013) only report the density of either under-saturated or over-saturated solutions, we use linear interpolation or extrapolation, respectively, to interpret their data as shown in Fig. 4.7. The comparison of ρ_T based on our model (Eq. 4.1) with the data of Song et al. (2013), Akinfiev and Diamond (2010), and Li et al. (2011) is shown for two values of m in Fig. 4.7. A relatively good agreement is obtained at $m = 1$ while there is a systematic difference of about 3% for $m = 3$. Fig. 4.7 also indicates that all activity coefficient models lead to essentially the same result.

To explain the difference between our model and experimental data, it is instructive to consider the factors that influence the calculation of density. These include the solubility of CO_2 in brine, the density of pure water and the partial

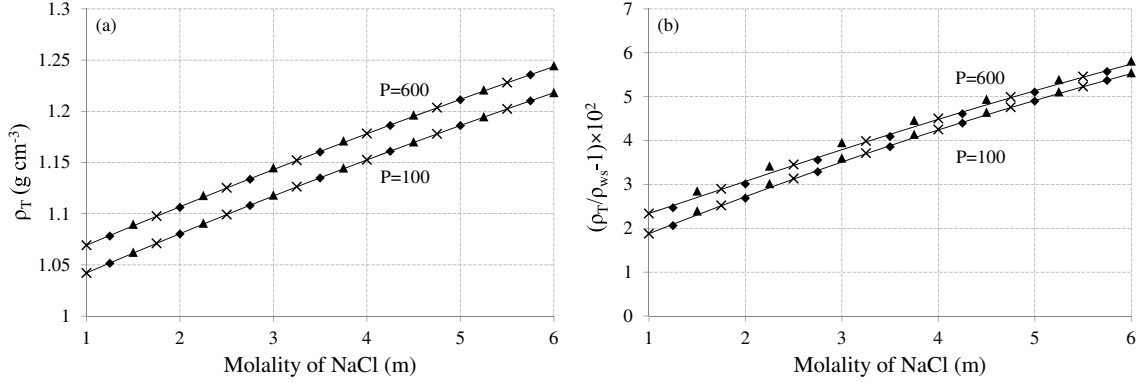


Figure 4.8: The density ρ_T of a ternary solution as a function of NaCl molality for the constant temperature 50°C and pressure (a) 100 bar and (b) 600 bar. The symbols show the influence of different models for the activity coefficient: Duan and Sun (2003) (solid line), Fournier (1985) (diamonds), Drummond (1981) (crosses), and Rumpf et al. (1994) (triangles).

molar volumes of dissolved NaCl and CO₂. Moreover, the excess volume of the mixture due to ion-CO₂ interactions has not been explored extensively in the previous models. In low salinity $m = 1$ a relatively good agreement is obtained because the contribution of ion-CO₂ interactions to the excess partial molar volume of CO₂ at given P and T tends to vanish.

Our calculation of the solubility is rigorous and the accuracy of the model that we use has been demonstrated extensively in the literature (Lemmon et al., 2003; Marini, 2007; Spycher and Pruess, 2005). The density of pure water has also been computed with a very accurate model that is consistent with the data of Wagner and Pruss (2002) and IAPWS-95. Moreover, the partial molar volume of NaCl is obtained with the highly accurate and widely accepted model of Rogers and Pitzer (1982). Finally, the relatively good agreement of our calculation of the partial molar

volume of liquid CO₂, $v_{2(l)}$ with the model of Duan et al. (2008) is encouraging for both models. However, the calculation of partial molar volume involves perhaps the greatest amount of uncertainty (see Fig. 4.5) and may be responsible for the difference. On the other hand, the systematic nature of the difference may point to the absence of some more fundamental factors in the model such as ionization and hydrogen bonds. There could also be experimental uncertainty that is not reported by Song et al. (2013).

Having confirmed our model with experimental data, we now perform a parametric study of ρ_T with respect to pressure, temperature and salinity. Fig. 4.7(a) shows the effect of pressure on ρ_T for constant temperature 60°C. Fig. 4.7(b) shows the effect of temperature on ρ_T for constant pressure 100 bar. Results are calculated for the salinities $m = 1$ and $m = 3$ using the activity coefficient models of Duan and Sun (2003) (solid line), Fournier (1985) (diamonds), Drummond (1981) (crosses), and Rumpf et al. (1994) (triangles). In all cases, we observe that ρ_T increases with pressure and decreases with temperature. This behavior is similar to that observed for the density of binary H₂O-NaCl solutions illustrated previously in Fig. 4.1 and occurs due to the increasing solubility with increasing pressure and decreasing solubility with increasing temperature.

We also observe that the influence of the four activity coefficient models in Fig. 4.7 is small, such that the relative percentage difference is on the order of 0.1%. The major difference between these models is that those of Fournier (1985) (diamonds), Drummond (1981) (crosses), Rumpf et al. (1994) (triangles) depend only on temperature and salinity, while the model of Duan and Sun (2003) further

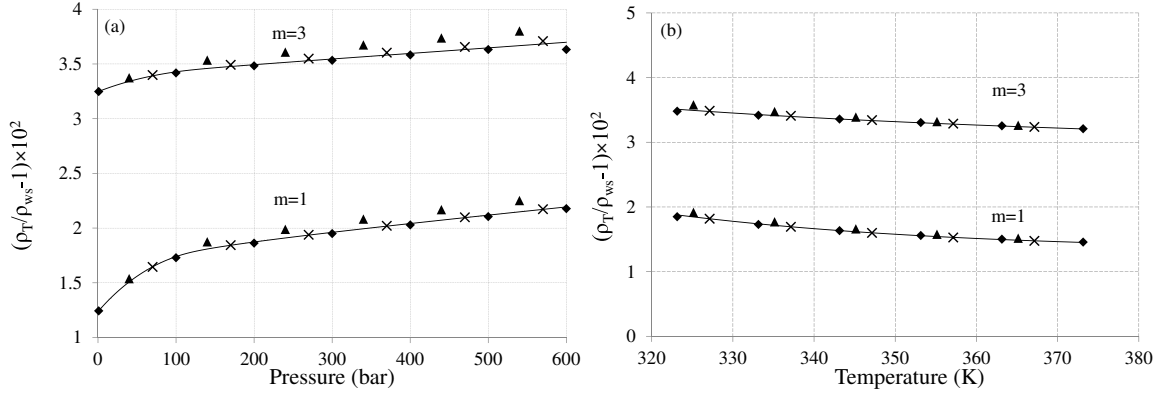


Figure 4.9: (a) Relative density difference between ρ_T and the density ρ_{ws} of H₂O-NaCl solutions at (a) 60°C and (b) 100 bar. Our calculations of $(\rho_T/\rho_{ws} - 1)$ are based on the activity coefficient models noted in Fig. 4.7.

includes the effects of pressure. The effects of pressure on γ_{CO_2} appear to be small.

Fig. 4.8 shows the influence of NaCl molality on ρ_T for $T = 60^\circ\text{C}$ and $P = 100$ bar (panel a) and 600 bar (panel b). The symbols and solid lines show the effect of the four different models for the activity coefficient. In all cases the density of the saturated ternary solution increases monotonically with increasing molality of NaCl. This is because increasing of mole fraction of NaCl with high molecular weight ($M_w = 58.44$ g/mol) leads to the increasing of the density of the ternary solution. This trend is shared by the variation of solution density with salinity at both low and high pressures, as shown in Fig. 4.8. Though the different activity coefficient models affect the values of ρ_T in Fig. 4.8, the maximum relative percentage difference, however, is less than 0.03%.

The relative density difference $(\rho_T/\rho_{ws} - 1)$ is plotted in Fig. 4.9(a), where ρ_{ws} is the density of the solution of H₂O and NaCl. We find that $(\rho_T/\rho_{ws} - 1)$

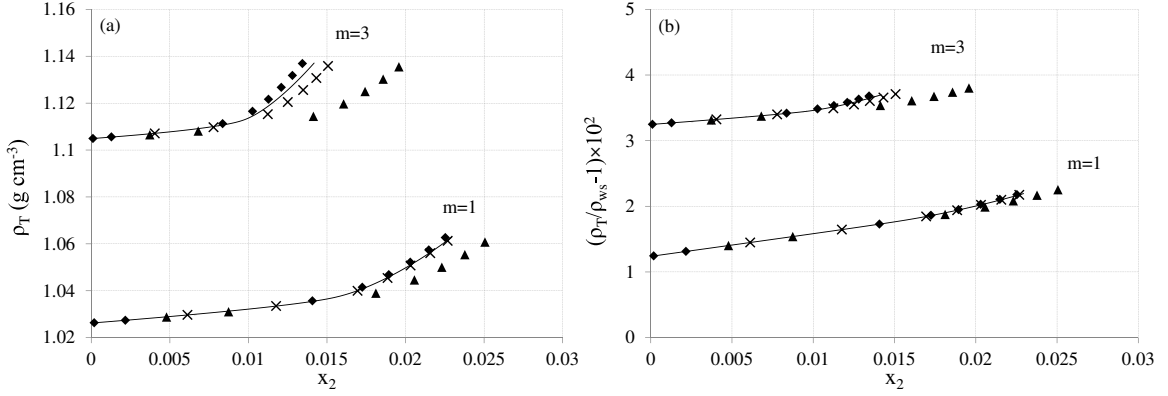


Figure 4.10: (a) Density of ternary solutions and (b) the relative density difference as a function of mole fraction. Our calculations are based on the activity coefficient models noted in Fig. 4.7.

increases with pressure and is always positive, indicating that ρ_T is greater than the density of the H₂O-NaCl solution. Within the range of higher pressures, $P > 100$, the increase in $(\rho_T/\rho_{ws} - 1)$ is more gradual than for $P < 100$. This is because at higher pressures, the variation of x_2 with pressure is relatively small. The higher level of salinity is also observed to increase the relative density difference because of the higher mole fraction of NaCl ($M_w = 58.44$ g/mol) associated with larger values of m_3 . Fig. 4.9(b) shows $(\rho_T/\rho_{ws} - 1)$ for different values of salinity within the range of 50-100°C and at 100 bar pressure. We observe that $(\rho_T/\rho_{ws} - 1)$ decreases with increasing temperature. Fig. 4.9 further indicates that the influence of different activity coefficients on $(\rho_T/\rho_{ws} - 1)$ is generally small.

We consider the relationship between ρ_T and the saturated mole fraction x_2 in Fig. 4.10(a), which shows that ρ_T increases with x_2 . The increase in ρ_T is much more rapid for larger values of the mole fraction, which is similar to the behavior of ρ_B as a function of x_2 plotted in Fig. 4.4(a). The influence of different activity coefficient

models on ρ_T is observed in Fig. 4.10(a) to increase for higher salinity solutions. For instance, the results based on the activity coefficient model of Rumpf et al. (1994) (triangles) seem to deviate slightly at higher pressures as shown in Fig. 4.10(a). This indicates that an accurate calculation of activity coefficients becomes more important for high salinity solutions. Fig. 4.10(b) depicts $(\rho_T/\rho_{ws} - 1)$ as a function of mole fraction x_2 at 60°C. Here, activity coefficient models appear to have only a small negligible effect on the relative density difference. While $(\rho_T/\rho_{ws} - 1)$ is always positive and increases monotonically with x_2 , higher salinity levels restrict x_2 to smaller values for the maximum pressure of 600 bar.

4.8 Onset of buoyancy driven convection

In this section, we use our results for the density of CO₂-H₂O and CO₂-H₂O-NaCl solutions to investigate the effects of temperature, pressure and salinity on the time required for onset of buoyancy-driven convection during CO₂ sequestration. We consider a homogeneous isotropic aquifer situated between two layers of impermeable rock, see fig. 4.11(a). The aquifer is characterized by a permeability κ , porosity θ , and dispersion coefficient \mathcal{D} . We assume that the supercritical CO₂ has collected in a horizontal layer situated below the upper cap rock and above the brine. The vertical z -coordinate points downwards in the direction of gravity, g . We assume that for the time scales of interest to onset of buoyancy-driven convection, the interface between the supercritical CO₂ and brine may be assumed fixed at $z = 0$. The lower layer of impermeable rock is situated at $z = H$.

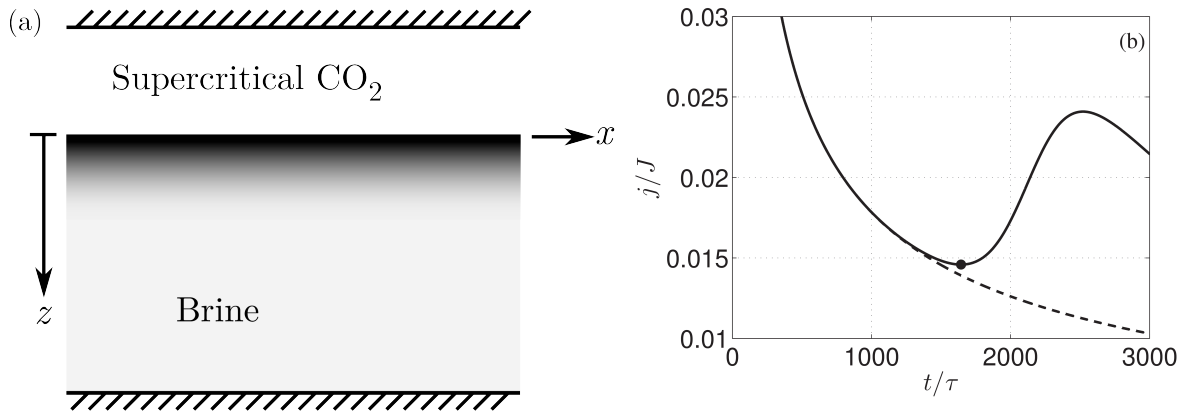


Figure 4.11: (a) Sketch (not to scale) of the homogeneous isotropic aquifer considered in Section 4.8. A layer of supercritical CO₂ is situated below the upper cap rock and above the brine. Dissolution of CO₂ forms a region of dense CO₂-rich brine (shaded dark gray) near $z = 0$. (b) The dashed line shows the temporal evolution of the flux j_d/J produced by the purely diffusive solution (4.15). The solid line shows the corresponding flux j/J produced a direct numerical simulation of buoyancy-driven convection (see Tilton and Riaz (2014) for details). The DNS was performed using the initial condition described in Eqs. 4.13–4.15 of Tilton and Riaz (2014) for ϵ^* . The solid dot shows the onset time of buoyancy-driven convection.

The brine is initially at rest, has a zero CO₂ concentration ($c = 0$), and has the uniform density $\rho = \rho_{ws}$. Dissolution of supercritical CO₂ is modeled by assuming that at time $t = 0$, saturated brine is supplied at $z = 0$ with constant concentration $c = c_{\text{sat}}$ and density $\rho = \rho_{\text{T}}$. With increasing time, $t > 0$, aqueous CO₂ diffuses downwards and forms a region of CO₂-rich brine near $z = 0$ that is shaded dark gray in fig. 4.11(a). For the time scales of interest to the current study, the end effects at $z = H$ are negligible (Tilton and Riaz, 2014) and the growth of the CO₂-rich layer is characterized by the following concentration profile,

$$c_d(z, t) = c_{\text{sat}} \left[1 - \operatorname{erf} \left(\frac{z}{\sqrt{4Dt}} \right) \right]. \quad (4.15)$$

The corresponding diffusive flux of CO₂ into the brine may be computed by applying Fick’s law at $z = 0$,

$$j_d = -\mathcal{D} \left. \frac{\partial c_d}{\partial z} \right|_{z=0} = J \sqrt{\frac{\tau}{\pi t}}, \quad (4.16)$$

where $J = c_{sat}U/\theta$ is a characteristic flux, $\tau = \theta^2 D/U^2$ is a characteristic time, and U is a characteristic buoyancy velocity $U = \kappa(\rho_T - \rho_{ws})g/\mu$. The subscripts “ d ” in Eqs. (4.15) and (4.16) stress that these relations are valid for the case of pure diffusion in quiescent brine, i.e. without convection. The dashed line in fig. 4.11(*b*) demonstrates that j_d decreases monotonically with increasing time.

As aqueous CO₂ diffuses downwards, the concentration profile c_d is naturally perturbed by local aquifer heterogeneities. Because the density of the CO₂-rich brine is greater than that of the underlying H₂O-NaCl solution, a gravitational

instability causes these perturbations to grow into finger-like structures that convect aqueous CO₂ downwards. This convection accelerates the dissolution of supercritical CO₂ and reduces the time required for total dissolution of the supercritical CO₂ (Ennis-King et al., 2003). This is demonstrated in Fig. 4.11(*b*) by the solid line showing the flux produced by a direct numerical simulation of this convection. Details of the simulation are given in Tilton and Riaz (2014). The initial time at which convection causes the flux to increase is marked with a solid dot. We refer to this time as the *onset time of buoyancy-driven convection*, $t = t_{on}$.

Tilton and Riaz (2014) recently obtained approximate relations for t_{on} using an initial value problem (IVP) approach. With this approach, a small perturbation is added to the diffusive solution c_d at an initial time $t = t_p$ through the initial

condition

$$c(x, z, t_p) = c_d(z, t_p) + c_p(z) \cos\left(\frac{2\pi x}{\lambda}\right). \quad (4.17)$$

The perturbation varies sinusoidally in the horizontal x -direction with the wavelength λ , and $c_p(z)$ is a shape function that describes the vertical variation of the perturbation. The initial perturbation (4.17) is characterized by an initial magnitude, ϵ^* , defined through the following non-dimensional norm,

$$\epsilon^* = \left[\frac{1}{L} \int_0^H \left(\frac{c_p}{c_{\text{sat}}} \right)^2 \right], \quad (4.18)$$

where $L = \theta D/U$ is a characteristic length. With the IVP approach, t_{on} is determined by numerically solving the governing transport equations subject to the initial condition (4.17). The main challenges are choosing physically acceptable combinations of the initial perturbation parameters ϵ , c_p , λ , and t_p , and managing the computational time. As this is beyond the scope of the current study, we refer readers to discussions in Daniel et al. (2013), Tilton et al. (2013), and Tilton and Riaz (2014).

Tilton and Riaz (2014) obtained the following relationships for t_{on} ,

$$\frac{t_{on}}{\tau} = 23.76 (\log_{10} \epsilon^*)^2 - 432.1 \log_{10} \epsilon^* + 89.75, \quad (4.19)$$

and for the dominant horizontal wavelength λ_{on} of the finger-like structures at $t = t_{on}$,

$$\frac{2\pi L}{\lambda_{on}} = 4.804 \times 10^{-4} (\log_{10} \epsilon^*)^2 + 6.968 \times 10^{-3} \log_{10} \epsilon^* + 0.06936, \quad (4.20)$$

Using relations (4.19) and (4.20) with our theoretical results for ρ_T and ρ_{ws} , we investigate the effects of temperature, pressure, and salinity on the onset time, t_{on} ,

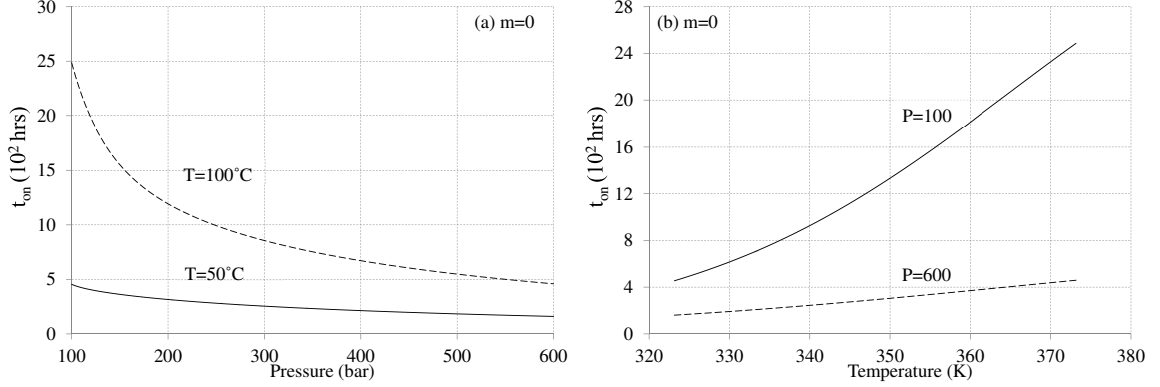


Figure 4.12: Onset time of buoyancy-driven convection t_{on} for H_2O-CO_2 solutions, $m = 0$, as a function of (a) pressure when $T = 50$ (solid line) and $100^\circ C$ (dashed line) and (b) temperature when $P = 100$ (solid line) and 600 bar (dashed line).

and wavelength, λ_{on} , for an aquifer with the following typical parameter values for CO_2 sequestration $\mu = 5 \times 10^{-4}$ Pa s, $\theta = 0.2$, $g = 9.81$ m s^2 , $\mathcal{D} = 10^{-9}$ m 2 s $^{-1}$, and $\kappa = 10^{-12}$ m 2 (Ennis-King et al., 2003; Tilton and Riaz, 2014; Zweigel et al., 2004). There currently remains significant uncertainty concerning appropriate values for the initial perturbation magnitude (Tilton and Riaz, 2014). For illustration purposes, we hereinafter consider the reasonable value of $\epsilon^* = 10^{-3}$.

Fig. 4.12(a) shows the variation of t_{on} with pressure for the salinity $m = 0$ and the temperatures $T = 50$ (solid line) and $100^\circ C$ (dashed line). We observe that t_{on} decreases with pressure because the solubility of CO_2 (x_{CO_2}) and the density difference $\Delta\rho = \rho_T - \rho_{ws}$ increase with pressure. Fig. 4.12(b) shows the variation of t_{on} with temperature for $m = 0$ when $P = 100$ (solid line) and 600 bar (dashed line). Increasing temperatures decrease the solubility of CO_2 , which results in a lower density difference and a higher t_{on} .

Fig. 4.13(a) plots the phase space spanned by t_{on} and x_{CO_2} as a function of

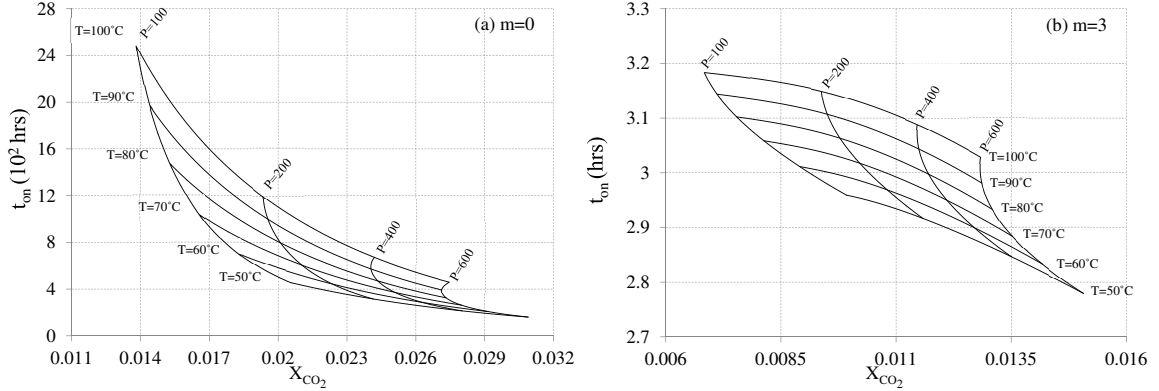


Figure 4.13: (a) The relationship between t_{on} and x_{CO_2} as a function of temperature and pressure, for salinities (a) $m = 0$ and (b) $m = 3$.

temperature and pressure for zero salinity, $m = 0$. We observe that t_{on} decreases with increasing pressure because the mole fraction x_{CO_2} and the density difference $\Delta\rho = \rho_T - \rho_{ws}$ increase with pressure. Along lines of constant pressure, increasing temperatures at low pressures uniformly decrease x_{CO_2} and increase t_{on} . The increase in t_{on} occurs due to the decrease in $\Delta\rho$ with decreasing mole fraction x_{CO_2} . For high pressures, however, an increase in temperature along lines of constant pressure produces a non-monotonic variation in the mole fraction, while t_{on} increases uniformly. Similar behavior was observed previously in Fig. 4.5(b). This implies that for certain combinations of high pressure and temperature, for example $(P,T) = (600 \text{ bar}, 90^\circ\text{C})$, the density difference $\Delta\rho$ can decrease, even though the mole fraction x_{CO_2} increases.

Fig. 4.13(b) shows the phase space spanned by t_{on} and x_{CO_2} for the nonzero salinity $m = 3$. The onset times for $m = 3$ are substantially smaller than those for $m = 0$ because the density increases with salinity. For example, in Fig. 4.13(a), onset of buoyancy driven convection occurs at $t_{on} = 2486$ hrs when $(P,T) = (100 \text{ bar}, 100^\circ\text{C})$.

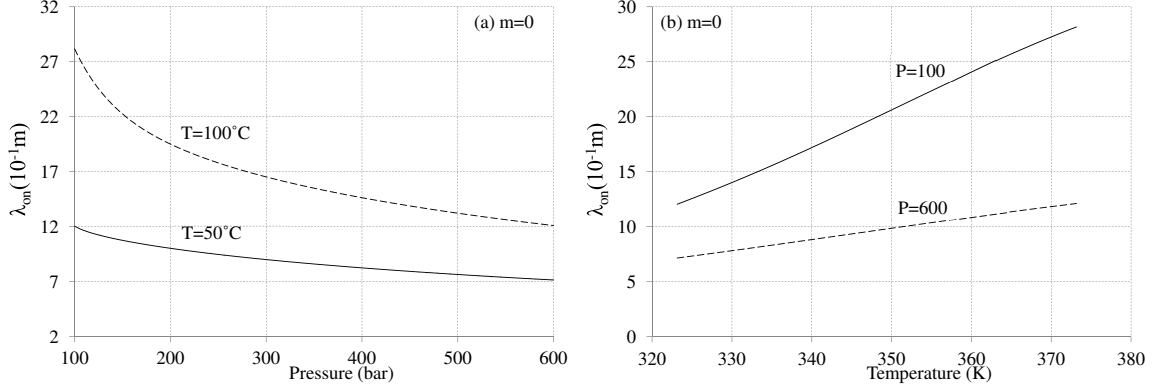


Figure 4.14: Wavelength λ_{on} for $\text{H}_2\text{O}-\text{CO}_2$ solutions, $m = 0$, as a function of (a) pressure when $T = 50$ (solid line) and 100°C (dashed line) and (b) temperature when $P = 100$ (solid line) and 600 bar (dashed line).

In Fig. 4.13(b), this decreases to $t_{on} = 3$ hrs. Figs. 4.12 and 4.13 are computed for the permeability $\kappa = 10^{-12}$. If the permeability is decreased to $\kappa = 10^{-13}$, the results for t_{on} must be multiplied by a factor of 100. This is because, from Eq. (4.19) and the definition of τ , t_{on} is inversely proportional to κ^2 .

In addition to the onset time, we present results for the wavelength λ_{on} of the finger-like structures at onset of convection because this characterizes the length scale of convective mixing. Fig. 4.14 shows the variation of λ_{on} with respect to pressure (panel a) and temperature (panel b) for salinity $m = 0$. We observe that λ_{on} decreases with pressure and increases with temperature because x_{CO_2} and $\Delta\rho = \rho_T - \rho_{\text{ws}}$ increase with pressure and decrease with temperature. Fig. 4.15 plots the phase space spanned by λ_{on} and x_{CO_2} as a function of temperature and pressure for salinity $m = 0$ (panel a) and $m = 3$ (panel b). As expected, λ_{on} decreases with pressure and salinity. Along lines of constant pressure, increasing temperatures at low pressures uniformly decrease x_{CO_2} and increase λ_{on} . The increase in λ_{on}

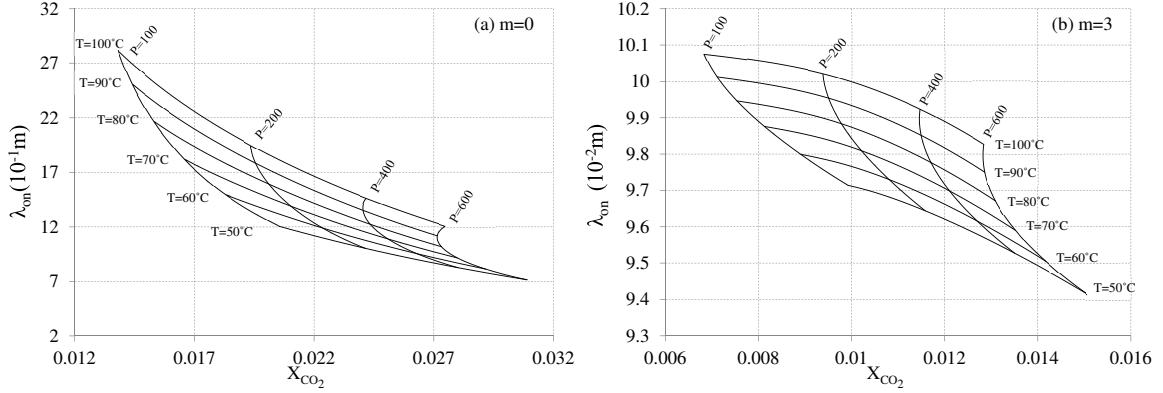


Figure 4.15: (a) The relationship between λ_{on} and x_{CO_2} as a function of temperature and pressure for permeability, $\kappa = 10^{-12}$, and salinity values of (a) $m = 0$, (b) $m = 3$.

occurs due to the decrease in $\Delta\rho$ with decreasing mole fraction. For high pressures, however, an increase in temperature along lines of constant pressure produces a non-monotonic variation in the mole fraction, while λ_{on} increases uniformly. Similar behavior was observed previously in Fig. 4.13(a).

Finally, we consider the aquifer properties shown in Table 4.6 that correspond to geologic sequestration occurring in the Alberta Basin (IEA, 2008). The pressures vary between 5915 kPa at 950 m depth and 27,000 kPa at 2814 m depth (Table 4.6); the temperature varies between 26°C and 103°C, and the salinity varies from 0.4 mol/kg to 5.84 mol/kg. For illustration purposes, we consider the average properties $T = 75^\circ C$, $P = 100$, $m = 3$, $\kappa = 2.05 \times 10^{-13}$, $\theta = 0.15$, and $\epsilon^* = 10^{-3}$. From these, we find that onset of buoyancy driven convection occurs at 41.24 hrs with the dominant wavelength $\lambda_{on} = 3.626 \times 10^{-2}m$.

Table 4.6: Characteristics of CO₂ injection into saline aquifers in western Canada.

| Characteristic | Values |
|--------------------------------|--|
| Injection depth (m) | $950 \leq z \leq 2814$ |
| Porosity (%) | $4 \leq \theta \leq 26$ |
| Permeability (m ²) | $9.87 \times 10^{-16} \leq \kappa \leq 4.08 \times 10^{-13}$ |
| Formation pressure (bar) | $60 \leq P \leq 270$ |
| Formation temperature (°C) | $50 \leq T \leq 100$ |
| Salinity (mol/kg) | $0.40626 \leq m \leq 5.8424$ |

4.9 Conclusion

We have developed a new model to predict the density of saturated solutions of CO₂-H₂O-NaCl. The model is based on calculating the liquid molar volume from experimental data for the density of saturated binary solutions and the corresponding mole fractions of dissolved CO₂.

To calculate the liquid molar volume of CO₂, the density of saturated binary H₂O-CO₂ solutions has been determined with multi-parameter, nonlinear regression of experimental data. This development improves earlier models of the liquid molar volume that depend only on temperature and do not often coincide with equilibrium conditions. The model can be improved systematically with the availability of more experimental data for the density of saturated binary solutions. Such data is relatively easier to obtain and is less sensitive to experimental uncertainty compared to direct measurement of liquid molar volume of CO₂, $v_{2(l)}$, experimentally.

The new liquid molar volumes related to saturated solutions have been linked in this study to the existing Redlich-Kwong EOS. This has been accomplished by

associating the new liquid molar volumes with one of the solution branches of the Redlich-Kwong EOS. The solution branch that corresponds to correct gas molar volumes has been maintained. With the modified Redlich-Kwong EOS it is now possible to obtain both the gas and liquid molar volumes simultaneously.

Our parametric study indicates that the densities of binary and ternary saturated solutions increase gently at low values of mole fraction but more rapidly at larger values. The relative densities of the saturated solutions do not vary appreciably at low mole fractions. In general, the solution density is found to increase with pressure, salinity, and the mole fraction of dissolved CO_2 , but decreases with an increase in temperature. We have also evaluated the influence of four different models for the activity of aqueous CO_2 in brine. We find that the influence of such models is important at higher level of salinity.

The comparison of ρ_T based on our model (Eq. 4.1) with the data of Song et al. (2013), Akinfiyev and Diamond (2010), and Li et al. (2011) is shown for two values of m in Fig. 4.7. A relatively good agreement is obtained at $m = 1$ while there is a systematic difference of about 3% for $m = 3$. This occurs because of the factors that influence the calculation of density. These include the solubility of CO_2 in brine, the density of pure water and the partial molar volumes of dissolved NaCl and CO_2 . Moreover, the excess volume of the mixture due to ion- CO_2 interactions has not been explored extensively in the previous models. The relatively good agreement is obtained for $m = 1$ because the contribution of ion- CO_2 interactions to the excess partial molar volume of CO_2 at given P and T is negligible.

We also investigate the effect of temperature $T \in [50, 100]^\circ\text{C}$, pressure $P \in$

[100, 600] bar, and salinity $m \in [0, 3]$ (which are the conditions for a typical aquifer) on the onset of buoyancy driven convection during CO₂ sequestration. For a given porosity and permeability, we find the onset time t_{on} can vary by one order of magnitude with variations in T, P and m. More specifically, t_{on} decreases with increasing pressure and salinity and decreasing temperature. It is also found that the onset time is highly sensitive to permeability. We conclude that high-permeability aquifers with high pressure, high salinity, and low temperature are most suitable for sequestration of CO₂, from the standpoint of minimizing the time required for the onset of buoyancy driven convection. For these conditions, we also find that the wavelength λ_{on} at onset of convection tends to be minimized. Though beyond the scope of this study, this may have an effect on mixing, nucleation and precipitation of secondary carbonates.

Chapter 5

Fracture simulation

5.1 Introduction

The fracture permeability, an important parameter controlling CO₂ migration throughout sequestration, affects the amount of mineralization trapping of CO₂ which enhances the long-term CO₂ storage. In this study, a long-term geochemical modeling of subsurface CO₂ storage is carried out in a single fracture to investigate the impact of fractures on CO₂ transport and storage capacity. The problem contains flow of injected CO₂ between finite plates that represents a single fracture. CO₂ is initially dissolved in the brine and then precipitates during the geochemical reactions between H₂O-CO₂ and minerals. In order to properly explain the physics of the reactive transport, we control the availability of calcium ions Ca²⁺ that contributes to the growth rate of calcite in the fracture. We then study the physics and the critical time of blockage within a reasonable simulation time to interpret the results. The model is composed of direct numerical simulation tools and algorithms for incompressible flow and conservative transport combined with kinetics of corresponding chemical reactions. For each time step, transport and reactions are solved by means of a finite difference method using a sequential non-iterative approach. It is found that mineral precipitation has an important effect on reservoir porosity and permeability. The single fracture is found to be filled at the inlet because concen-

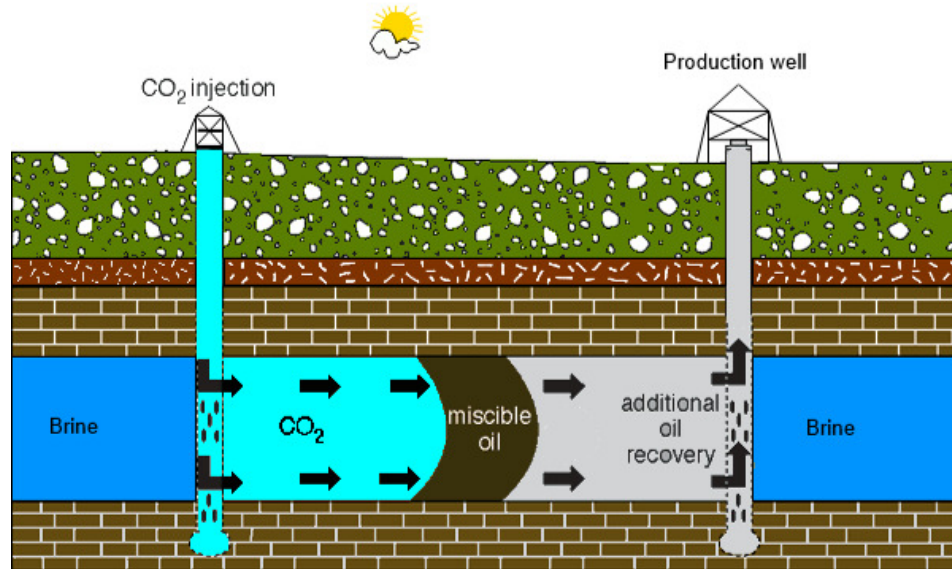


Figure 5.1: Schematic diagram illustrating the use of CO₂ injection to Enhance Oil Recovery (EOR).

trations of carbonate ions are greater (more saturated states). In addition, using parameter analysis we also could determine the effect of various mineral precipitates on porosity of fractures.

Among the various mechanisms and means of CO₂ sequestration, trapping in enhanced oil recovery (EOR) operations is the most attractive because it provides a secure geological trap, while contributing to the recovery of additional oil through fractures and realizing an economic benefit that helps in offsetting the cost of CO₂ sequestration (Shaw et al., 2002) (see figure 5.1). Therefore, the geological sequestration of CO₂ through fractures are intended for the interpretation, prediction, and transport of chemical species in subsurface environments.

Sequestration of CO₂ in fractured rocks is done by four principal mechanisms: solubility trapping, mineral trapping, structural trapping, and residual trap-

ping (Hitchon, 1996; Luo et al., 2012; Ngoc et al., 2014). Solubility and mineral trapping are the most stable long term solutions to CO₂ sequestration because they prevent mobile hazards such as leakage of CO₂ to the surface (Bachu et al., 1994; Bolourinejad et al., 2014; Shogenova et al., 2009). The appealing concept that CO₂ could be permanently trapped as aqueous species and mineral precipitates has prompted several experimental and numerical studies to investigate these principal mechanisms (Dalkhaa et al., 2013; Ketzer et al., 2009; Liu and Maroto-Valer, 2013; Ma and Yoon, 2013; Mitiku et al., 2013; Pham et al., 2011; Work, 2013; Xu et al., 2001).

Although experimental fluid dynamics play an important role in validating and determining the limits of the various approximations to the governing equations, it is limited in the Rayleigh number it can achieve. Therefore, it is usually short of full scale. High temperature values associated with coupled reactive fluid flow problems are also beyond the scope of many experimental facilities. This is particularly true of reactive mass transfer problems where the changing mineral compositions add another level of complexity. Moreover, many geological formations are too big or too remote in space or in time to simulate experimentally. Therefore, obtaining detailed information of fluid flow would be expensive and time consuming. Moreover, geological reservoir and porous media flows are generally inaccessible to detailed experimental measurement because mineral alterations are very slow throughout geological sequestration of CO₂ (Busch et al., 2010). Therefore, all of these categories of fluid motion are amenable to the computational approach. Computational fluid dynamics provides detailed information and consequently permits a useful un-

derstanding of the flow processes to be obtained (Molins et al., 2012).

A variety of simulators have been developed by the petroleum industry (Johnson et al., 2005), including ECLIPSE (Exploration Consultants Limited Implicit Program for Simulation Engineering), TOUGH (Transport of Unsaturated Groundwater and Heat), NUFT (Nonisothermal, Unsaturated Flow and Transport) and CMG-GEM (Canada Modeling Group-Generalized Equation of State Model), for numerical simulation study. The simulators mentioned above are used to model the movement of the CO₂ plume, the flow characteristics and the rate of the four trapping mechanisms during and after CO₂ injection. However, available data rarely corresponds to the equilibrium state of supercritical CO₂ with respect to the liquid phase. Consequently, such data cannot be paired with the saturated mole fraction of dissolved CO₂ to determine the pH of the system and kinetics of the chemical reactions (Duan et al., 2008). Estimates of reaction rates based on mole fraction of CO₂ that do not correspond to saturated solutions are not suitable for predicting phase changes related to mass transfer across material interfaces during CO₂ sequestration (Nomeli and Riaz, 2014).

Fractures in geology are defined as fluid channels that have a high permeability (Noh, 2003). The spatial variations of fracture properties, such as aperture width and orientations, are complicated and irregular. Many other parameters can also influence the CO₂ flow characteristics inside a fracture, including temperature, pressure, salinity, permeability, and heterogeneity (Green and Ennis-King, 2010; Kumar et al., 2004; Ozah et al., 2005; Saadatpoor et al., 2007). One way to approach the characterization is to start from a local characterization of a designated fracture and

expand to geological fractured formations.

Fluid flow inside a fracture is not always in local equilibrium with minerals with which it is in temporary or permanent contact. The deviation from equilibrium is usually small and the reaction kinetics under this condition is often very sensitive to environmental factors and solution compositions (Stumm et al., 1992). Minerals dissolve in or react with components in the aqueous phase. Under different conditions, minerals are precipitated and accumulated on the fracture walls.

CO₂ trapping by secondary carbonate minerals such as calcite CaCO₃, dolomite CaMg(CO₃)₂, siderite FeCO₃, and dawsonite NaAlCO₃(OH)₂ could occur inside fractures (Gislason et al., 2010). Since the fugacity of CO₂ is high through sequestrations, calcite is a wide spread mineral under the conditions considered in our investigation (Marini, 2007). The addition of CO₂ mass as secondary carbonates to the solid phase leads to a decrease in permeability of the fractures. Consequently the fractures may become filled with precipitates of minerals during their burial over geologic time scales (Laubach, 2003). Permeability of the fracture controls the path of aqueous CO₂ migration. Therefore the variation of aperture dimension has a pivotal role on solubility and mineral trapping of injected CO₂.

Especially in low permeability reservoirs, the natural fracture permeability is an important issue. In many reservoirs, major fractures appear to dominate reservoir performance as compared to smaller and tighter fractures that play only a minor role. In fractured reservoirs with a small porosity and permeability, the closure of natural fractures will occur during depletion of a reservoir. Therefore, permeability of a major fracture has a critical importance in assessing the economics of a future

reservoir development.

Reactive transport in porous media is a dynamic process that affects: mineral composition and surface chemistry, porosity, permeability, and fluid flow. Fracture aperture width can shrink or get larger as the chemical reactions proceed at the fracture surface. The mass conservation equation is applied to find that how the fracture aperture width changes with time. Laubach et al. (2000) observed that the same differential stresses control the behavior of both large and tiny fractures. The results of his studies show that mineralization of macro-fractures is similar to micro-fractures in numerous cases (Laubach, 2003). Therefore, the macro-fractures study provides useful information about fate of micro-fractures through mineral trapping of CO₂.

In this study, a numerical model of reactive transport is developed to evaluate long term mineral trapping of CO₂ inside a designated fracture. The model is used to simulate a reactive fluid within a permeable fracture. Fluid convection, diffusion, and chemical reactions inside a finite space are solved as a simplified representation of natural mineral trapping. The purpose of the current study is to evaluate the critical time of blockage based on Reynolds, Peclet, and Damköhler numbers that correspond to the properties of the fluid flow such as its velocity, pH, and concentrations of reactive aqueous species as well as the physical properties of the fracture such as its dimensions.

There are several different parameters that affect the precipitation/dissolution of minerals such as reaction order, complexes, adsorption, convection, diffusion, and desorption. To date, because of lack of data on nucleation and precipitation of calcite

under aquifer conditions, estimation of the amount of trapped CO_2 through mineral trapping after a specific period of time has been a critical unresolved problem. Recently, the kinetics of corresponding chemical reactions under aquifer conditions are given by Nomeli and Riaz (2014). Moreover, the fundamental issue in mineral trapping of CO_2 is to perceive how the fractures are filled with precipitates and cease to be fluid channels. To overcome this in the current study, transport and reactions are solved by means of a finite difference method using a sequential non-iterative approach. We show that how the fracture aperture width distributions change with time. This is motivated by the fact that finite difference schemes are simple to understand and they are easy to generalize to more complex boundary conditions due to the production of solid phase as minerals precipitates and, last but not least, they are easy to implement on a computer. The interaction between flow and chemical reactions is significant and plays a pivotal role through mineral trapping of CO_2 ; however, a large computational penalty has to be paid if this is considered explicitly.

Although mineral kinetics properties and reactive surface area are not well constrained and range of problems concerning the interaction of water- CO_2 -minerals is very broad, the numerical modeling gives us useful insights into the storage of CO_2 inside the fracture. This study is organized as follows. In section 5.2 we describe the mass conservation equation including convection, diffusion, and reaction terms that predicts actual efficiency of mineral trapping mechanism by considering physical properties of fluid flow and characteristics of the mineral compositions. In section 5.3.1 the incompressible Navier-Stokes equation is solved by the standard projection

method to obtain the velocity distribution. In section 5.3.3, we investigate the critical time of blockage for a single fracture. It is found that the fractures are filled at the inlet with precipitates and cease to be fluid channels after specific period of time.

5.2 Model Description

After injection of CO_2 into a fracture, it starts reacting with water molecules H_2O available inside the fracture and produces carbonic acid H_2CO_3 . pH reduction due to the solubility of CO_2 induces rock mineral alteration (Nomeli and Riaz, 2014; Palandri, 2004). Aqueous H_2CO_3 dissociates to bicarbonate HCO_3^- and carbonate CO_3^{2-} ions and then reacts with free calcium Ca^{2+} which is provided by anorthite $\text{CaAl}_2\text{Si}_2\text{O}_8$ and they eventually convert to the secondary mineral which is called calcite CaCO_3 . The sources of calcium Ca^{2+} and carbonate ions CO_3^{2-} required for continued precipitation are (1) transport of carbonate ions by fluid flow and (2) presence of calcium ions. An under-saturated solution becomes supersaturated when it goes through fractures. This occurs because carbonate ions are transported by fluid flow. The equilibrium is completely reached between the fracture surfaces in contact with that fluid because of the slow movement of reactive fluid.

Dissociation of carbonic acid to bicarbonate $\text{HCO}_{3(\text{aq})}^-$ and carbonate $\text{CO}_{3(\text{aq})}^{2-}$ ions is almost instantaneous (see Eqs. 3.3 and 3.4), therefore it can be effectively considered at equilibrium. However, the chemical reaction leading to the production of calcite is kinetically slow (Jacobson and Langmuir, 1974; Mucci, 1983; Visconti

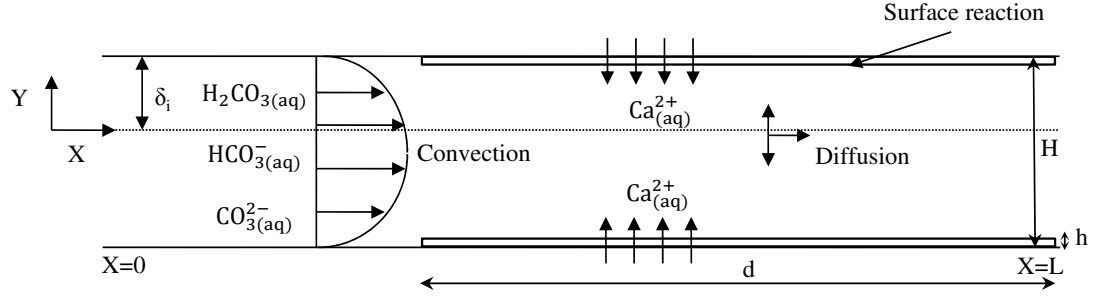


Figure 5.2: Schematic picture of precipitation and dissolution reaction in a single fracture.

et al., 2010). In general, the solubility product of CaCO_3 , $\text{pK}(\text{CaCO}_3)$, is -8.41 at 25°C (Jacobson and Langmuir, 1974) which is too low. Therefore, on long time scale, CO_2 will be permanently trapped in aquifers as a form of calcite.

The governing chemical reactions in the current study are the following:

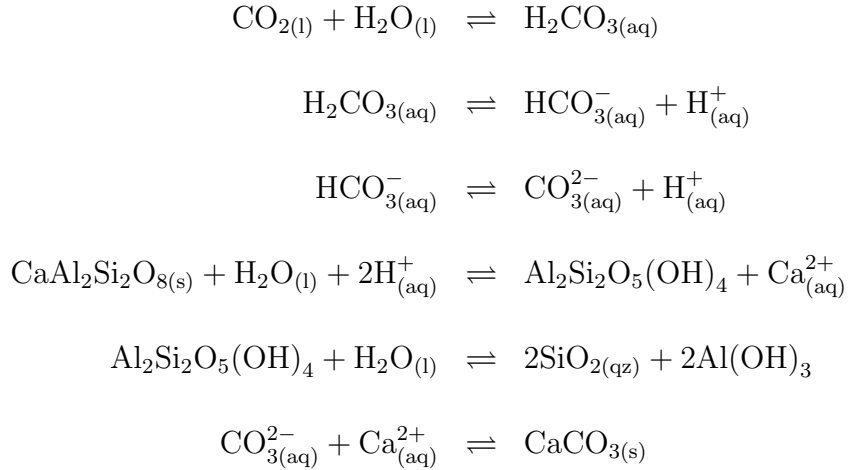


Figure 5.2 shows a schematic diagram of species convection and diffusion. The finite parallel walls denote a single fracture and the region outside of the plates represents the source of calcium ions Ca^{2+} . The dissolved CO_2 flows between the plates when it diffuses toward the x- and y-directions. The reaction rate at the

surface is affected by the concentration of aqueous species. We are going to solve the mass conservation equation inside a two-dimensional finite parallel plates by considering the fluid convection, diffusion and chemical reactions. The code will use a sequential non-iterative approach, which solves the transport and the reaction equations separately. The simulation is expected to reveal the time evolution of the aperture shrinkage caused by precipitation of calcite. This will lead to a direct estimate of the amount of trapped CO₂ through mineral trapping after a specific period of time.

In order to carry out the simulation, we assume a uniform and constant pressure and temperature, uniform initial concentrations for the mass transport, the precipitation of calcite takes place at the solid surfaces, flow is single-phase, incompressible and laminar in the fracture, the chemical reaction between carbonate and calcium ions produces calcite, precipitates are porous and allow the aqueous species to dissolve out from the surfaces, convection and diffusion occur in the x- and y-direction, diffusion coefficients are isotropic and independent of concentrations, fracture has finite length and its network is connected.

Consider the transport of the concentration of each species across the boundary of volume V . The amount of each species in the volume V is equal to the integral of the concentration over the volume, expressed mathematically by the integral $\int_V C_i dV$. The amount escaping or entering through the boundaries of V per unit time is equal to the integral of the flux over the surface enclosing the volume, or in symbols $\int_A J_i dS$, where J_i is the flux of the concentration across the surface A , and dS points in a direction normal to the surface. The flux is taken to be positive if it is

directed along the outward normal dS to the surface A . The total amount of species concentration consumed or produced at the rate R_i by chemical reactions taking place within the volume is equal to $\int_V R_i dV$. Therefore, the reaction term and transport terms require to be included in the mass conservation equations. The rate of change with time of the concentration of species i contained within the volume V can be expressed as:

$$\frac{d}{dt} \int_V C_i dV = - \int_A J_i dS + \int_V R_i dV , \quad (5.1)$$

This equation can be put in differential form by transforming the surface integral using Gauss's theorem and then rearranging the equation by placing the time derivative inside the integral to yield:

$$\int_V \left\{ \frac{\partial C_i}{\partial t} + \nabla \cdot J_i - R_i \right\} dV = 0 , \quad (5.2)$$

because the volume V is arbitrary the integrand itself must vanish leading to the differential equation:

$$\frac{\partial C_i}{\partial t} + \nabla \cdot J_i = R_i , \quad (5.3)$$

This equation holds at each point within the volume V and expresses the desired conservation law for the concentration of each species. Where J_i represents the solute flux of the i th species consisting on contributions from advection and diffusion, with form $J_i = -D_i \nabla C_i + \mathbf{u} C_i$. Where, D_i is diffusion coefficient and \mathbf{u} is velocity of fluid. The chemical reaction rates R_i , are assumed to be first order with respect to the concentrations of reactive components $R_i = k \min(C_i, C_j)$. Where, k denotes the reaction rate normalized to the reacting surface area ($\text{mole m}^{-2}\text{s}^{-1}$), s represents

specific surface area of solid (m^{-1}). Applying the general expression Eq. 5.3 yields the following mass conservation equation,

$$\frac{\partial C_i}{\partial t} = -\left(u \frac{\partial C_i}{\partial x} + v \frac{\partial C_i}{\partial y}\right) + D_i \left(\frac{\partial^2 C_i}{\partial x^2} + \frac{\partial^2 C_i}{\partial y^2}\right) \pm k_s \min(C_i, C_j) , \quad (5.4)$$

Before proceeding, the desirable properties of a numerical solution to the transport equation should be considered. The three main properties we seek are: (1) accuracy in both space and time, which implies that errors are minimized, (2) monotonicity, meaning that negative concentration are not produced and computational efficiency, (3) stability of the solution is also important. Our modeling of flow and transport inside the fracture for the mineral trapping purpose is based on space discretization by means of integral finite differences. We solve partial differential equations by using a second-ordered finite difference discretization. The second-order approximation is used to calculate the concentrations of the species. Higher order approximations are also possible, however, they may introduce spurious oscillations which may not be monotone. This is particularly true in the case of high Peclet number (Steeffel et al., 2005).

Figure 5.3 shows the discretization stencil in two dimensions. The discretization is performed in a rectangular grid system. The grid spacing, Δx and Δy are given by $x_{i+1} - x_i$ and $y_{j+1} - y_j$, respectively. The finite difference schemes which are cell-centered assume that the concentration at the grid itself is representative of the entire cell and it is coupled with the velocity at the boundary of the cell.

Eq. 5.3 is solved using an operator splitting approach, where, for each time step, transport and reactions are solved using a sequential approach. First, the

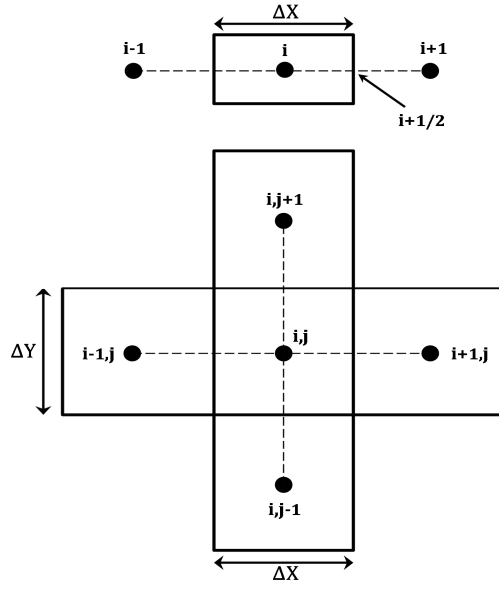


Figure 5.3: Cell-centered finite difference discretization scheme in two dimensions.

conservative transport step advances the concentration of each reactive species in the aqueous phase, subject to the fluid Courant-Friedriches-Lewy (or CFL) condition, which constraints the time step size Δt for a given spatial discretization $(\Delta x, \Delta y)$. Δt is selected as the minimum value of the following equations, $\min(\Delta t_1, \Delta t_2, \Delta t_3)$, to satisfy the CFL number:

$$\begin{aligned}
 \Delta t_1 &= \frac{\text{Re}}{2(1/\Delta x^2 + 1/\Delta y^2)} \\
 \Delta t_2 &= \frac{4}{\text{Re}(u_{\max} + v_{\max})^2} \\
 \Delta t_3 &= Cdx^2 \min(\text{Pe}_1, \text{Pe}_2) ,
 \end{aligned} \tag{5.5}$$

Convection and diffusion of carbonate ions in brine alter the local equilibrium and usually makes the solution supersaturated. The deviation from equilibrium affects the precipitation/dissolution rates of calcite. At supersaturated levels calcite precipitates inside the fracture and accumulated on the surface of the walls. Dissolution and precipitation of all minerals are assumed to be kinetically controlled (Nomeli

and Riaz, 2014), therefore, the model can monitor changes in porosity and permeability during the simulation from changes in the volume of the fracture. However, the uncertainties are as follows: effect of flow velocity on distribution of calcite along a fracture and role of nucleation and crystal growth.

We incorporate the periodic boundary condition to solve the PDEs. The accuracy of the periodic approximations is sufficiently high to justify, in some cases, using a larger computational domain to simulate periodically. Despite the great accuracy of this approximation, it is not without pitfalls such as aliasing error. The last point in the values is omitted since it should always be the same as the first. The periodic boundary conditions are defined as follows:

$$C(i, j - 1) = C(i, ny) \text{ for } j = 1, i \in \Omega, \quad (5.6)$$

The velocity values are zero inside the solid phase and the fluid is at rest. This occurs because the mineral precipitates are assumed to be porous and permeable. Therefore, the aqueous species can still diffuse through the precipitates.

Initial concentration of CO_3^{2-} is 0 inside the fracture and initial concentration of Ca^{2+} is obtained from saturation state of calcite. The non-dimensional length and width of the channel are 2 and 1, respectively. The normalized concentration of dissolved CO_2 is 1 on the left hand-side. The concentration of Ca^{2+} , inside the primary solid phase at the top and bottom of the channel, is normalized with respect to the initial concentration of dissolved CO_2 .

5.3 Reactive transport in a fracture

5.3.1 Governing equations for flow and transport

We solve the mass conservation equation inside a two-dimensional finite parallel walls by considering convection, diffusion, and chemical reactions. We use a sequential approach to solve the transport and the reaction equations separately. The non-dimensional form of convection-diffusion-reaction equation (5.4) can be obtained in the following form ($t = Ht^*/U$, $C = \rho C^*/M_w$, $x = Hx^*$ and $\mathbf{u} = U\mathbf{u}^*$). Where, C stands for the concentration of Ca^{2+} and aqueous species of dissolved CO_2 , ρ denotes the density, M_w is the molecular weight of calcite, U is the characteristic velocity, D represents the diffusion coefficient of species and H is the aperture width of the fracture.

$$\frac{\partial C_i^*}{\partial t^*} = \frac{1}{\text{Pe}} \nabla \cdot (D \nabla C_i^*) - \nabla \cdot (\mathbf{u}^* C_i^*) + \text{Da} \min(C_i^*, C_j^*) , \quad (5.7)$$

here, \mathbf{u} is the velocity vector and is obtained from direct numerical simulation of the Navier-Stokes equation at the pore scale. The Peclet number, Pe , compares the characteristic time for diffusion given a length scale with the characteristic time for advection, $\text{Pe} = UH/D$. We characterize reaction kinetics with the local Damköhler number, $\text{Da} = rH/U$, that is the ratio of the reaction rate, $r = k/HC_{1,in}$, to the rate of convection. Where, $C_{1,in}$ is the initial concentration of dissolved CO_2 when $T = 50^\circ\text{C}$, $P = 100$, and $m = 0$ that is constant for all of the simulations. Here, k is the dissolution rate of anorthite which in turn is a function of the concentration of the dissolved CO_2 in the fractures. The global Da that is shown in the following

figures and tables for each case, however, is a function of the saturated concentration of the dissolved CO₂ at the inlet.

A large Peclet number with respect to the velocity U will lead to a small Damköhler number. Under this condition a large concentration passes almost entirely throughout the fracture resulting in a relatively uniform precipitation of carbonates. Inside the fractures, however, there is always a spatial variation of Da due to changes in the concentration of the reactive species and reaction rate. The global Da that is shown in the following figures and tables for each case, however, is a function of the saturated concentration of the dissolved CO₂ at the inlet.

Precipitation of calcite occurs when the flow becomes supersaturated. At this point, the saturation index SI requires to be more than solubility product of calcite.

$$SI = \text{Log}_{10} \frac{a_{\text{Ca}^{2+}} a_{\text{CO}_3^{2-}}}{K_{\text{sp}}} , \quad (5.8)$$

Here SI is the saturation index with respect to calcite, which represents saturation states of injected CO₂. a is a thermodynamic activity and K_{sp} is a thermodynamic solubility product of calcite. The saturation index is a useful quantity to determine whether the brine is saturated ($SI = 0$), undersaturated ($SI < 0$), or supersaturated ($SI > 0$) with respect to the given minerals. Changes in pressure, temperature and salinity not only can affect the solution saturation state, but are also likely to influence the Damköhler number at a given saturation state, P, T and m.

We assume that based on our solubility calculation, the corresponding low aqueous mole fractions of CO₂ ($x_{\text{CO}_2} < 3\%$) do not affect significantly the viscosity and density of the solution which is taken as constant during CO₂ sequestration.

Javaheri et al. (2010) have shown that the effect of geothermal gradients is small compared to solutal effects in real sites for CO₂ sequestration. Therefore, the fluid velocity distribution is determined by the equations of motion for a Newtonian fluid with a constant density and viscosity. A dimensionless Reynolds number Re can be obtained when one uses the following non-dimensional form of the incompressible Navier-Stokes equations (Panton, 2006). This is why mathematically all flows with the same Re are comparable,

$$\frac{\partial \mathbf{u}}{\partial t} + (\mathbf{u} \cdot \nabla) \mathbf{u} = -\nabla P + \frac{1}{Re} \nabla^2 \mathbf{u}, \quad (5.9)$$

when the Reynolds number, $Re = |\mathbf{u}|H/\nu$, is less than 1 (in practice flow is in the Stokes regime), the term $(\mathbf{u} \cdot \nabla) \mathbf{u}$ in Eq. 5.9 is negligible and the model simply becomes the time-dependent Stokes equation. However, when inertial forces are not negligible ($Re \geq 1$), the full Eq. 5.9 must be solved.

Here \mathbf{u} is the velocity vector, ρ is the fluid density, P is the pressure, and ν is the kinematic viscosity of the fluid. The parabolic velocity profile is initialized at the inlet (see Figure. 5.2). Likewise, periodic boundary conditions are considered here.

Eq. 5.9 is solved using the projection method which is an effective means of numerically solving time-dependent incompressible fluid-flow problems (Harlow and Welch, 1965). The algorithm of projection method is based on the Helmholtz decomposition (sometimes called Helmholtz-Hodge decomposition) of any vector field into a solenoidal part and an irrotational part. Typically, the algorithm consists of two stages. In the first stage, an intermediate velocity that does not satisfy the

incompressibility constraint is computed at each time step. In the second, the pressure is used to project the intermediate velocity onto a space of divergence-free velocity field to get the next update of velocity and pressure. In the following equation, the intermediate velocity, $\hat{\mathbf{u}}$, is explicitly computed using the Eq. 5.9 ignoring the pressure gradient term,

$$\frac{\hat{\mathbf{u}} - \mathbf{u}^n}{\Delta t} = -(\mathbf{u}^n \cdot \nabla) \mathbf{u}^n + \nu \nabla^2 \mathbf{u}^n, \quad (5.10)$$

where \mathbf{u}^n is the velocity at n^{th} time level. In the next step,

$$\frac{\mathbf{u}^{n+1} - \hat{\mathbf{u}}}{\Delta t} = -\frac{1}{\rho} \nabla P^{n+1}, \quad (5.11)$$

that can be rearranged for the velocity at $(n + 1)$ time level,

$$\mathbf{u}^{n+1} = \hat{\mathbf{u}} - \frac{\Delta t}{\rho} \nabla P^{n+1}. \quad (5.12)$$

Computing the right-hand side of the Eq. 5.11 requires a knowledge of the pressure, P , at $(n + 1)$ time level that is obtained by taking the divergence of both sides. Due to the divergence-free (continuity) condition, $\nabla \cdot \mathbf{u}^{n+1} = 0$ and the following Poisson equation is derived for P^{n+1} ,

$$\nabla^2 P^{n+1} = \frac{\rho}{\Delta t} \nabla \cdot \hat{\mathbf{u}}, \quad (5.13)$$

the final projection is then applied to enforce the divergence restraint on the velocity field. Substitution of the expression for the pressure field from Eq. 5.13 into the Eq. 5.9 yields the velocity for the next time level $(n + 1)$.

Table 5.1: Formal description of calcite structure.

| Calcite | |
|-----------------|---------------------------------|
| Class symmetry | Trigonal scalenohedral |
| Cell contents | 6CaCO ₃ |
| Cell parameters | a = b = 4.9896 Å, c = 17.0610 Å |

5.3.2 Governing equations for the growth rate of calcite

The CO₃ group is the fundamental structure of carbonate minerals. The C-O bond in calcite, which is computed by means of the empirical technique of Brown and Shannon (1973), is strongly covalent and is ~ 4 times greater than that of Ca-O bond. The general structure of calcite was expressed by Bragg (1914), while the other parameters of calcite were determined by Sass et al. (1957). Density of calcite is calculated by the following equation:

$$\rho = \frac{M_w (\text{g} \cdot \text{mol}^{-1})}{v (\text{cm}^3 \cdot \text{mol}^{-1})}, \quad (5.14)$$

where, ρ denotes the density, M_w is the molecular weight of calcite, and v represents the volume of the unit cell of calcite. The molar volume of calcite, v , can be obtained as follows:

$$v = \frac{v_o N_A 10^{-24}}{Z}, \quad (5.15)$$

where Z is the number of molecules of the substance in the unit cell which is 6 for calcite, N_A the Avogadro's number ($6.02214 \times 10^{23} \text{ mole}^{-1}$) and 10^{-24} the transformation factor from Å^3 to cm^3 . The formal description of calcite structure is given in table 5.1 (Marini, 2007). The cell parameters are used to calculate the unit cell volume of calcite, from which molar volume and density can be obtained. For

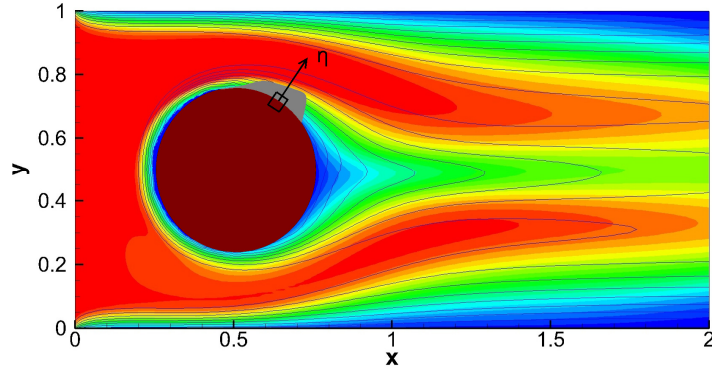


Figure 5.4: The production of precipitates on the surface of the original solid phase. η points in a direction normal to the surface of the solid phase.

any mineral, independent on the crystal system, the volume of the unit cell, v_o , is given by (Pauling, 1988), $v_o = abc(1+2\cos\alpha \cos\beta \cos\gamma - \cos^2\alpha - \cos^2\beta - \cos^2\gamma)^{1/2}$. For the hexagonal crystal system: $\alpha = \beta = 90^\circ$ and $\gamma = 120^\circ$. So $v_o = abc(1 - \cos^2\gamma)^{1/2}$. Since density of the calcite has been determined, a mass balance on solid phase at the fracture surface gives the rate change for the width of the fracture :

$$\frac{dm}{dt} = -r_{\text{CaCO}_3} M_w \quad , \quad \frac{d\eta}{dt} = -\frac{r_{\text{CaCO}_3} M_w}{\rho_{\text{CaCO}_3} A} \quad , \quad (5.16)$$

here $d\eta$ points in a direction normal to the surface of the solid phase (see Figure 5.4), M_w is the molecular weight, ρ_{CaCO_3} and r_{CaCO_3} denote the density and production rate of the calcite, respectively. By definition, r_{CaCO_3} is positive for precipitation reaction so that the aperture width of the fracture decreases with time.

The molar volume of calcite can also be computed through the following equa-

Table 5.2: Volumetric thermal expansion coefficients of carbonate minerals.

| Mineral | Cell parameters or volume | Thermal expansion coefficients | | | T range(K) |
|---------|------------------------------|--------------------------------|----------------|--------|------------|
| | | $a_o(10^{-4})$ | $a_1(10^{-8})$ | a_2 | |
| Calcite | a | -0.0315 | 0 | 0 | 297 – 1173 |
| | c | 0.1922 | 2.5183 | -1.214 | 297 – 1173 |
| | v | 0.0713 | 3.3941 | -1.214 | 297 – 1173 |

tion (Markgraf and Reeder, 1985):

$$v_{T, \text{CaCO}_3} = v_{T^\circ, \text{CaCO}_3} \cdot \exp \left[\int_{T^\circ}^T \alpha(T) dT \right], \quad (5.17)$$

here $v_{T^\circ, \text{CaCO}_3}$ is the molar volume of the calcite at the reference temperature. The experimental thermal expansion data of calcite are expressed by (Fei, 1995):

$$\alpha(T) = a_o + a_1 T + a_2 T^{-2}, \quad (5.18)$$

where the constants a_o , a_1 and a_2 are called isobaric volumetric thermal expansion coefficients. The differences, however, are always $\leq 0.01 \text{ cm}^3 \text{ mol}^{-1}$ and can be neglected. The volumetric and linear thermal expansion coefficients of calcite and dolomite are expressed by Fei (Fei, 1995) and are listed in Table 5.2 (Marini, 2007).

Figure 5.5 shows the variation of the v-component of the velocity vector \mathbf{u} for the entire domain and also the magnitude of the velocity vector \mathbf{u} as a function of y for a few values of fixed x . The volumetric flow rate is independent of the z -direction within a fracture, and the flow velocity is large where the aperture width is small and it is small where the aperture width is large. Therefore, velocity varies with time and is a function of aperture width. Because of precipitation at the surface,

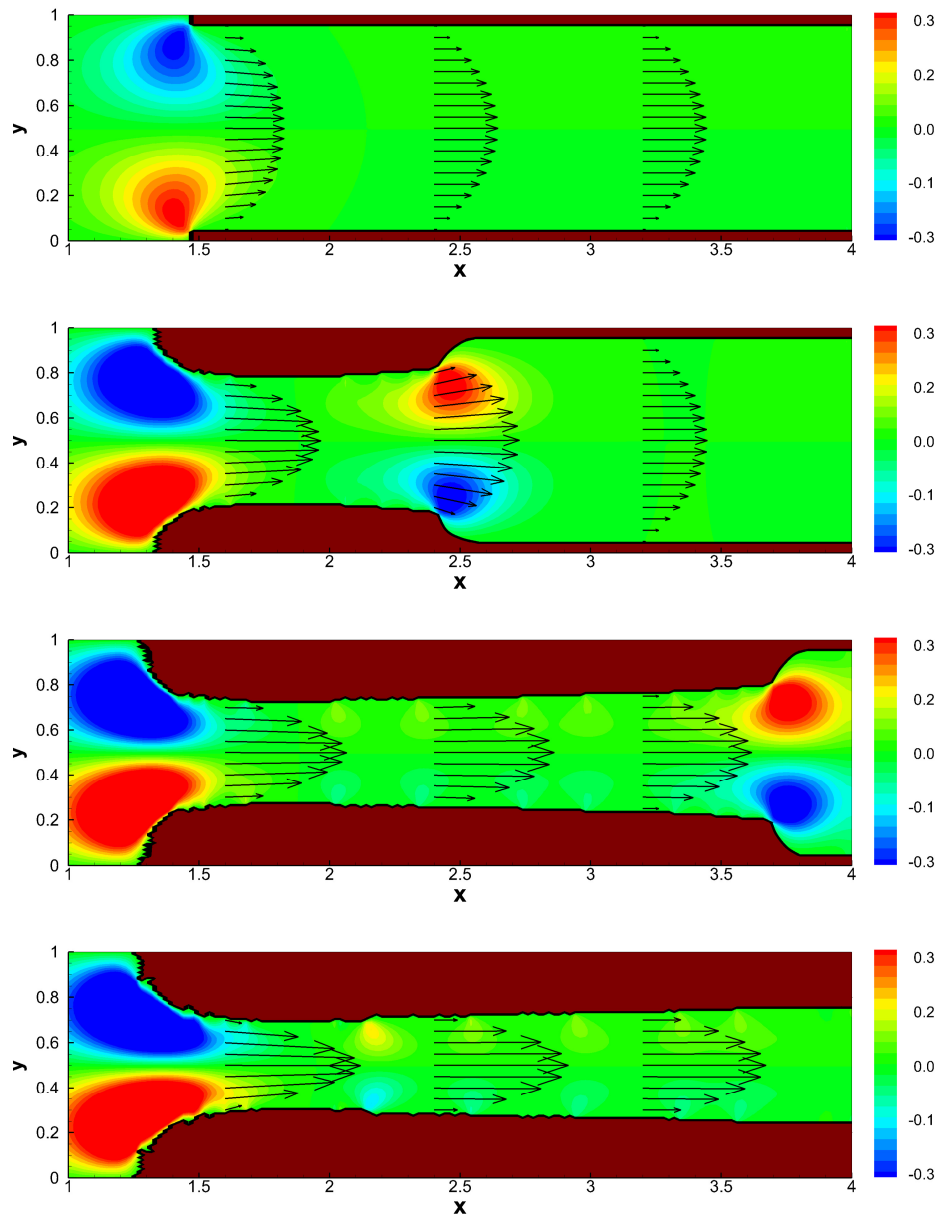


Figure 5.5: Normalized u-component of the velocity vector, \mathbf{u} , for the entire grid inside the domain and also as a function of y for a few values of fixed x when (a) $t = 3.171$, (b) $t = 6.342$, (c) $t = 9.512$, and (d) $t = 12.683$.

the aperture width is a function of a position and time. The ration of the L^2 -norm of the velocity components, $\|v\|_2/\|u\|_2$, is 0.087 and 0.0942 when $t = 6.342$ and $t = 12.684$, respectively. Therefore, the v -component of the velocity vector \mathbf{u} is not negligible and we need to numerically solve the two-dimensional, unsteady, incompressible Navier-Stokes equation, with special boundary conditions to obtain the velocity distribution in the domain.

5.3.3 Dimensionless critical time of blockage t_c for the fracture

The fundamental issue in mineral trapping of CO_2 is to predict when the fractures are filled with precipitates and cease to be fluid channels. Precipitation process of calcite requires fluid flow to import carbonate ions and calcium ions to be provided from the designated walls. This study focuses on constructing a numerical model of real fractures. Precipitation takes place at the surface as a function of supersaturated concentration of each species. The rate change of aperture width is also a function of reaction rate (see Eq. 5.16). Velocity should be updated after each time-step. By doing the simulation the time evolution of the aperture shrinkage caused by precipitation of calcite can be predicted. Therefore, we will be able to give an estimation of the amount of trapped CO_2 though mineral trapping after a specific period of time.

The variations of t_c and Da with respect to different temperature, pressure and salinity values are summarized in Table 5.3. The two dimensional flow field has 201×101 grids in the x - and the y -directions. It is found that for a constant

Table 5.3: The effects of temperature, pressure and salinity on Damköhler and critical time of blockage t_c when $Re = 10$ and $Pe = 1000$

| | | T=323.15/K | | T=348.15/K | | T=373.15/K | |
|------------|-------|------------------|-------|------------------|-------|------------------|-------|
| m/molality | P/bar | Da $\times 10^2$ | t_c | Da $\times 10^2$ | t_c | Da $\times 10^2$ | t_c |
| 0 | 60 | 1.71 | 5.612 | 2.71 | 5.443 | 3.97 | 5.394 |
| 0 | 90 | 1.77 | 5.566 | 2.78 | 5.412 | 4.09 | 5.340 |
| 0 | 130 | 1.80 | 5.538 | 2.82 | 5.383 | 4.18 | 5.255 |
| 0 | 200 | 1.85 | 5.437 | 2.83 | 5.338 | 4.22 | 5.174 |
| 0 | 270 | 1.88 | 5.352 | 2.84 | 5.271 | 4.25 | 5.121 |
| 0.40626 | 60 | 1.70 | 5.552 | 2.66 | 5.495 | 3.85 | 5.400 |
| 0.40626 | 90 | 1.71 | 5.484 | 2.68 | 5.418 | 3.89 | 5.219 |
| 0.40626 | 130 | 1.74 | 5.480 | 2.74 | 5.401 | 3.91 | 5.181 |
| 0.40626 | 200 | 1.79 | 5.474 | 2.75 | 5.237 | 3.97 | 5.170 |
| 0.40626 | 270 | 1.81 | 5.392 | 2.78 | 5.178 | 4.08 | 5.164 |
| 3.1243 | 60 | 1.62 | 5.506 | 2.59 | 5.299 | 3.75 | 5.231 |
| 3.1243 | 90 | 1.63 | 5.384 | 2.63 | 5.296 | 3.84 | 5.207 |
| 3.1243 | 130 | 1.67 | 5.280 | 2.67 | 5.271 | 3.87 | 5.196 |
| 3.1243 | 200 | 1.72 | 5.239 | 2.72 | 5.184 | 3.94 | 5.166 |
| 3.1243 | 270 | 1.73 | 5.233 | 2.76 | 5.135 | 4.02 | 5.135 |
| 5.8424 | 60 | 1.16 | 6.285 | 2.27 | 6.243 | 3.53 | 6.231 |
| 5.8424 | 90 | 1.22 | 6.265 | 2.43 | 6.182 | 3.68 | 6.142 |
| 5.8424 | 130 | 1.27 | 6.201 | 2.50 | 6.103 | 3.75 | 6.068 |
| 5.8424 | 200 | 1.31 | 6.106 | 2.57 | 5.995 | 3.82 | 5.940 |
| 5.8424 | 270 | 1.31 | 6.086 | 2.62 | 5.867 | 3.86 | 5.808 |

Table 5.4: Physical properties of a single fracture in Figure 5.6.

| Properties | Parameters | Value |
|-----------------------------|---------------|---|
| Characteristic velocity | U | 0.1 [cm/s] |
| Length of Anorthite surface | d | $3L/8 < d < L$ |
| Fracture aperture width | H | 0.1 [cm] |
| Reynolds number | $Re = UH/\nu$ | 10 |
| Peclet number | $Pe = UH/D$ | 1000 |
| Damköhler number | $Da = k/UC$ | 0.0175, 0.042 |
| Hight of Anorthite surface | h | 0.008 [cm] |
| Density | ρ | 1 [g/cm ³] |
| Molecular weight | M_w | 100 [g/mol] |
| Kinematic viscosity | ν | 1×10^{-3} [cm ² /s] |
| Diffusion coefficient | D | 1×10^{-5} [cm ² /s] |

pressure, increasing temperature uniformly increases Damköhler number Da and decreases t_c . In most cases, the smaller t_c occur at low salinity, high pressure and temperature. Changes in P , T and m not only can affect the solubility of CO_2 , but also influence the reaction rate k , Damköhler number Da , and subsequently the critical time of blockage t_c for a single fracture. We employ these results for our further investigation on the fracture simulation.

Figure 5.6 shows the concentration of the reactive components, aqueous species of dissolved CO_2 with the streamlines at Reynolds number $Re=10$ and Peclet number $Pe=1000$. Dimensionless numbers are calculated from the data shown in Table 5.4. Aqueous species of dissolved CO_2 , comes into the channel from the left hand side and calcium ion, Ca^{2+} , dissolves out from the surface of the original walls. Larger concentration always occure at the center of the fracture because the fluid velocity is

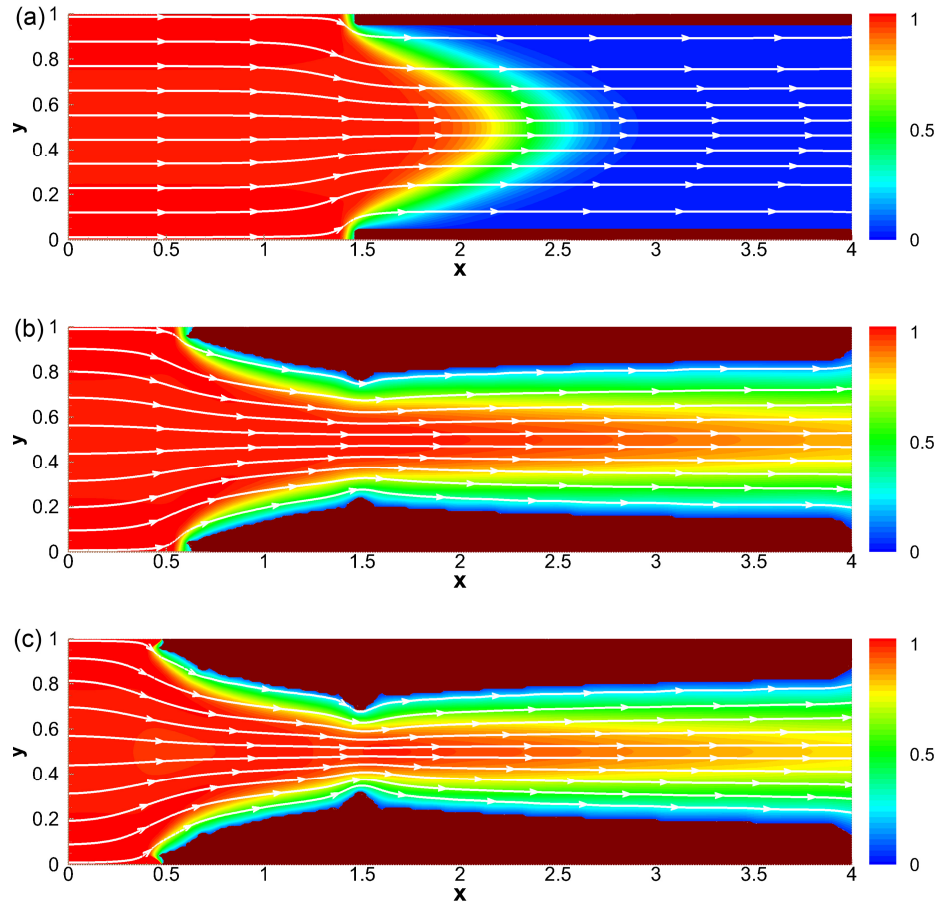


Figure 5.6: Normalized concentration of the reactive component, aqueous species of dissolved CO_2 , with the streamlines at Reynolds number=10 and Peclet number=1000 inside a fracture blockage with smooth walls (b) $t_c = 5.437$, when $T = 50^\circ\text{C}$, $P = 200$, $m = 0$, $\text{Da} = 1.75 \times 10^{-2}$, (c) $t_c = 5.174$, when $T = 100^\circ\text{C}$, $P = 200$, $m = 0$, $\text{Da} = 4.20 \times 10^{-2}$.

Table 5.5: Physical properties of the single fracture in Figure 5.7.

| Properties | Parameters | Value |
|-----------------------------|-------------|----------------|
| Temperature | T | 50°C |
| Pressure | P | 100 bar |
| Molality of NaCl | m | 1 |
| Length of Anorthite surface | d | $3L/8 < d < L$ |
| Damköhler number | $Da = k/UC$ | 0.01907 |

largest there. The large velocity tends to carry the injected (unreacted) components the farthest compared to the other regions in the x-direction (see Figure 5.5).

The reactive components are transported by convection, diffusion and chemical reactions inside the liquid phase. Although the flow is at rest inside the solid phase (no convection), calcium ions are still transported by diffusion. Once two reactive components reach each other precipitation takes place and calcite forms. We observe that the concentration gradient in the x-direction, though it can be small, is never exactly zero. Therefore, there is always a difference in fracture aperture widths between the inlet and the outlet. It is found that the fracture is filled at the inlet because concentrations of carbonate ions are greater (more saturated states). We also observe that for a constant pressure, increasing temperature from 50°C in Figure. 5.6(b) to 100°C in Figure. 5.6(c) increases Damköhler number Da and decreases t_c .

Figure 5.7 shows the concentration of the reactive components, aqueous species of dissolved CO_2 with the streamlines. Damköhler number is calculated from the data shown in Table 5.5. Carbonate ion, CO_3^{2-} , comes into the channel from the left

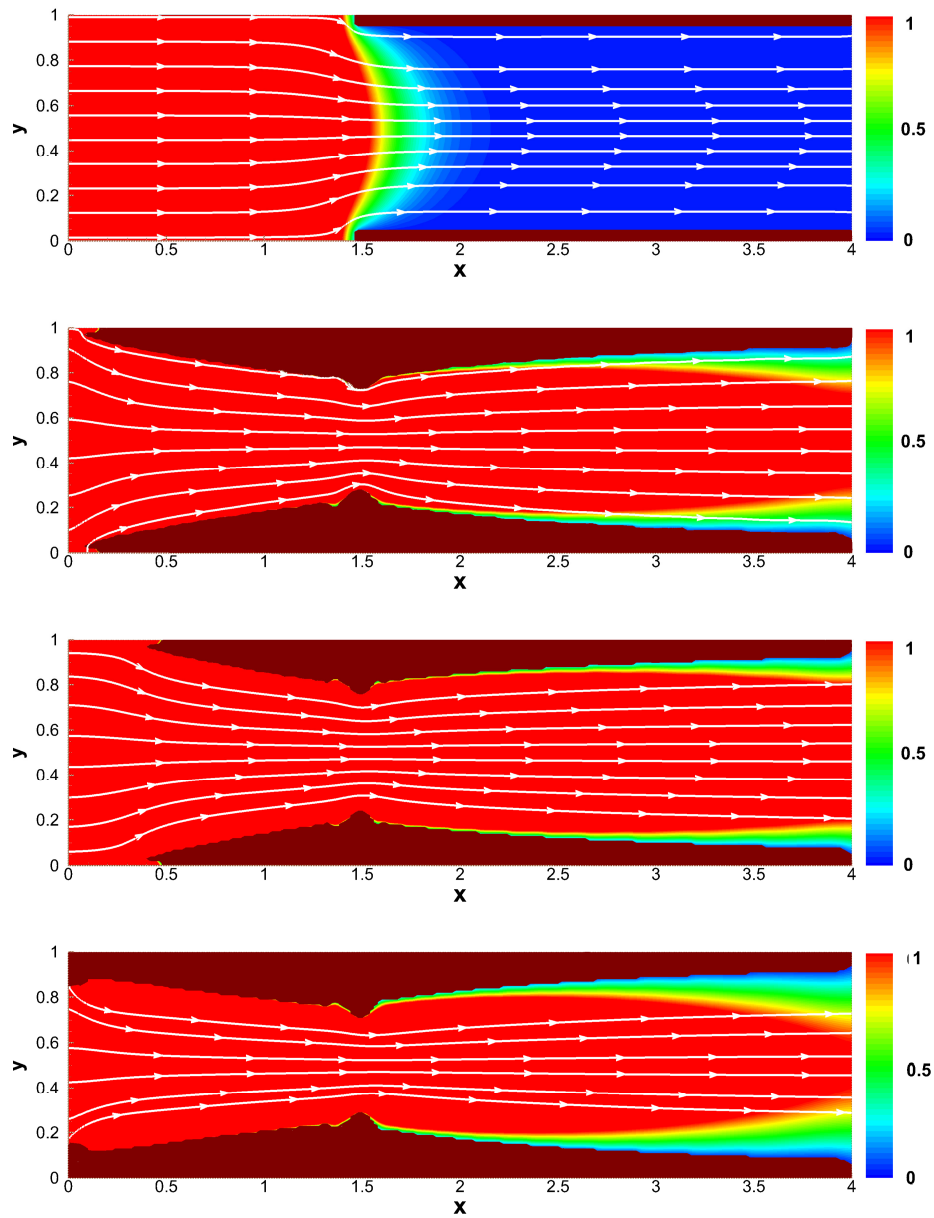


Figure 5.7: Normalized concentration of the reactive component, aqueous species of dissolved CO_2 , inside the fracture with the streamlines when (b) $\text{Re}=10$, $\text{Pe}=10$, (c) $\text{Re}=10$, $\text{Pe}=1000$, (d) $\text{Re}=50$, $\text{Pe}=10$. $t = 0.81$ for (a), $t = 2.42$ for (b), (c) and, (d)

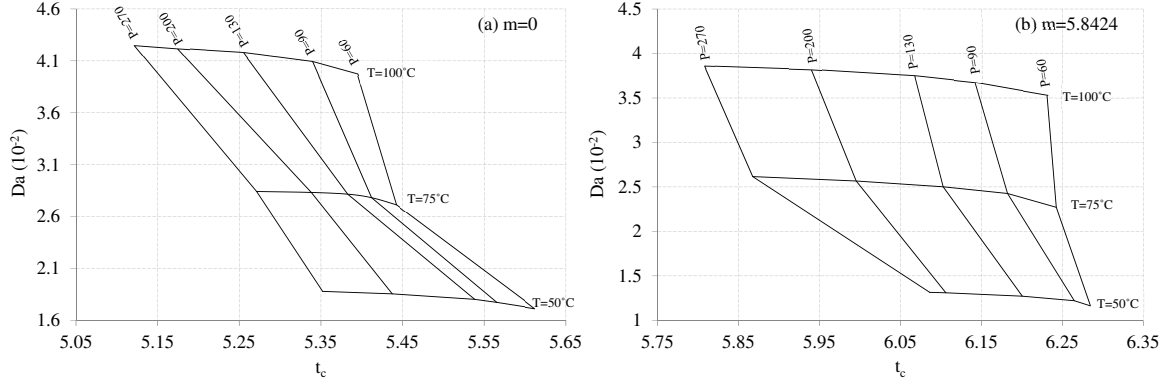


Figure 5.8: Critical time of blockage for the single fracture with pressure and temperature based on activity coefficient model of Duan and Sun (2003) in (a) pure water, $m=0$, (b) saline water with molality of NaCl, $m=5.8424$.

hand side and calcium ions, Ca^{2+} , are provided from the surface of the original walls. The reactive components are transported by convection, diffusion, and chemical reactions inside the liquid phase. Although the flow is at rest inside the solid phase (hatched area), calcium ions are still transported by diffusion. Once two reactive components reach each other precipitation takes place and calcite forms. There is a difference in fracture aperture widths between the inlet and the outlet. This occurs because the concentration gradient in the x-direction is not zero. The fracture is filled at the inlet because concentrations of carbonate ions are greater (more supersaturated states). We observe that for a constant Damköhler number Da , increasing Peclet number Pe from 10 in Figure. 5.7(b) to 1000 in Figure. 5.7(c) decreases the production of calcite precipitates which results in an increase in t_c . Increasing Reynolds number Re from 10 in Figure. 5.7(b) to 50 in Figure. 5.7(d) increases the production of calcite precipitates which results in a decrease in t_c . The variations of t_c with respect to different Re , Pe , and Da are summarized in Table 5.6.

Figure 5.8(a) plots the phase space spanned by Da and t_c as a function of temperature and pressure for salinity $m=0$. We observe that t_c decreases with increasing pressure on the constant lines of temperature because the mole fraction x_{CO_2} and reaction rate k increase with pressure. Along lines of constant pressure, increasing temperatures uniformly increases Damköhler number Da and decreases t_c . The decrease in t_c occurs due to the increase in reaction rate k which in turn results in an increase of Da .

Similar behavior is observed in Fig. 5.8(b) that plots the phase space spanned by Da and t_c as a function of temperature and pressure for salinity $m = 5.8424$. t_c is found to increase with salinity. The increase in t_c occurs due to the effect of salinity on solubility of CO_2 which results in a decrease in k and Da .

Figure 5.9(a) shows the critical time for a fracture blockage, t_c , with smooth walls as a function of Reynolds number Re when $Da = 1.70 \times 10^{-2}$, $Pe = 10$ (diamonds), $Pe = 100$ (squares), and $Pe = 1000$ (triangles). It is found that, for Peclet numbers ($Pe = 10$, $Pe = 100$), the critical time is insensitive to Reynolds number and decreases with Peclet number. For $Pe = 10$ and $Pe = 100$, the critical time oscillates around the mean value of $t_c = 4.7$ and $t_c = 2.4$, respectively. At high Peclet number $Pe = 1000$, however, the critical time generally decreases with increasing Reynolds number. This occurs because the concentrations of the reactive aqueous species becomes supersaturated due to the faster transport of reactive components. However, at $Pe = 1000$ and $Re = 100$ there is an outlier which may arise due to the production of different shape of precipitates.

Figure 5.9(b) shows the critical time for a fracture blockage, t_c , with smooth

Table 5.6: The effects of temperature, pressure and salinity on Damköhler and critical time of blockage t_c

| Re | Da=0.0170 | | | Da=0.0167 | | | Da=0.0197 | | | Da=0.0387 | | |
|-----|-----------|---------|---------|-----------|---------|---------|-----------|---------|---------|-----------|---------|---------|
| | Pe=10 | Pe=100 | Pe=1000 |
| 1 | 4.40244 | 2.54600 | 5.58604 | 5.4892 | 2.85012 | 5.5614 | 3.21372 | 2.3252 | 5.636 | 3.09344 | 2.24304 | 5.44512 |
| 10 | 4.72135 | 2.47378 | 5.43015 | 5.74693 | 2.75927 | 5.33105 | 3.2339 | 2.26751 | 5.6046 | 3.22853 | 2.16718 | 5.12645 |
| 20 | 4.76961 | 2.40788 | 4.90981 | 5.80613 | 2.73896 | 4.59758 | 3.22283 | 2.21239 | 5.02412 | 3.19418 | 2.13901 | 5.08466 |
| 30 | 4.80169 | 2.38304 | 4.50134 | 5.84398 | 2.74922 | 4.6938 | 3.18776 | 2.14402 | 4.70973 | 3.19203 | 2.18986 | 4.24756 |
| 40 | 4.82717 | 2.40375 | 4.50824 | 5.87101 | 2.70246 | 4.30821 | 3.20016 | 2.19782 | 4.32777 | 3.16896 | 2.11378 | 4.07194 |
| 50 | 4.84129 | 2.36612 | 4.11707 | 5.89529 | 2.75267 | 3.76502 | 3.17791 | 2.20315 | 4.2973 | 3.17069 | 2.15109 | 3.96732 |
| 60 | 4.83504 | 2.36289 | 3.62471 | 5.90759 | 2.75686 | 4.20576 | 3.17689 | 2.18137 | 3.40149 | 3.15522 | 2.1267 | 3.82527 |
| 70 | 4.82326 | 2.36717 | 3.51508 | 5.91417 | 2.75405 | 3.42957 | 3.22706 | 2.2088 | 3.40149 | 3.15324 | 2.16159 | 3.67237 |
| 80 | 4.80667 | 2.35491 | 3.41353 | 5.9146 | 2.77748 | 4.22478 | 3.14856 | 2.16124 | 4.29649 | 3.14891 | 2.12636 | 3.2735 |
| 90 | 4.82576 | 2.37586 | 2.74417 | 5.90684 | 2.74715 | 2.58979 | 3.15847 | 2.1857 | 3.07889 | 3.12235 | 2.13435 | 3.63879 |
| 100 | 4.74861 | 2.31136 | 3.58972 | 5.89099 | 2.72748 | 2.74169 | 3.12728 | 2.24563 | 3.48833 | 3.12814 | 2.19265 | 3.26489 |

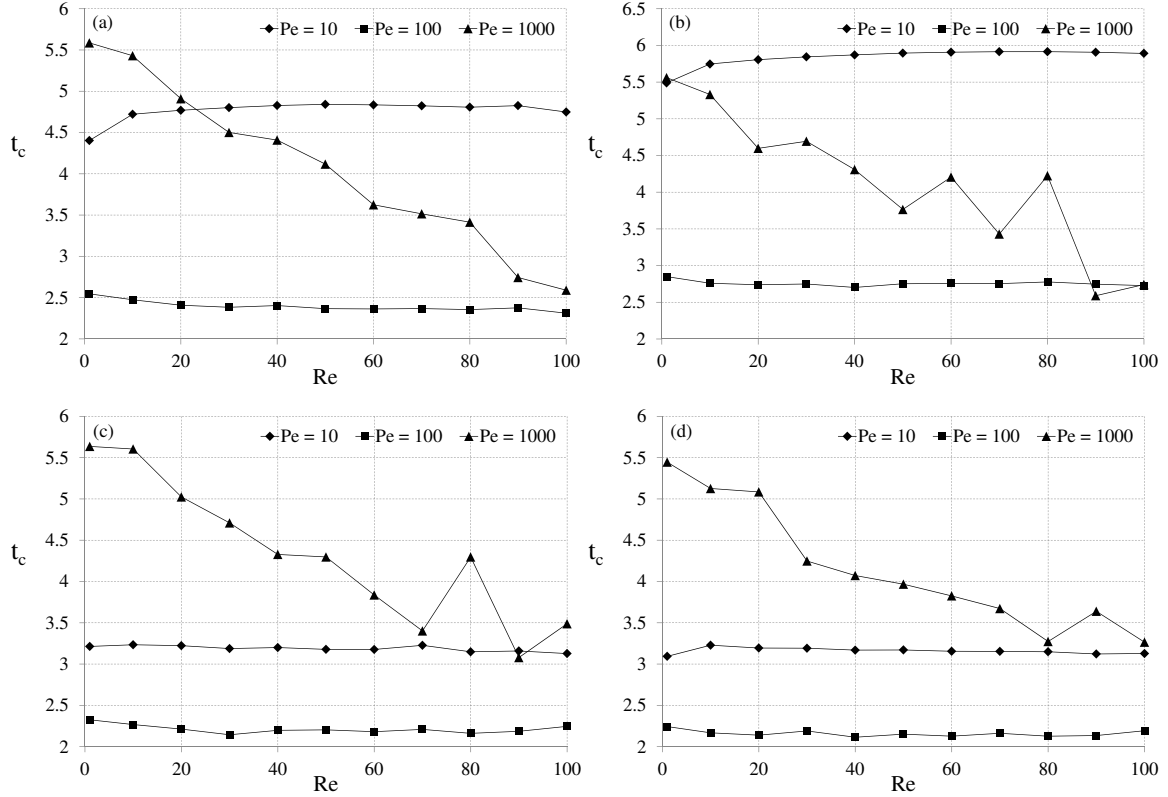


Figure 5.9: Critical times for a fracture blockage with smooth walls with respect to the changes in dimensionless numbers (a) $T = 50^\circ\text{C}, P = 100, m = 1, Da = 1.70 \times 10^{-2}$, (b) $T = 50^\circ\text{C}, P = 100, m = 3, Da = 1.67 \times 10^{-2}$ (c) $T = 50^\circ\text{C}, P = 400, m = 1, Da = 1.97 \times 10^{-2}$ (d) $T = 100^\circ\text{C}, P = 100, m = 1, Da = 3.87 \times 10^{-2}$.

walls as a function of Reynolds number when $Da = 1.67 \times 10^{-2}$, $Pe = 10$ (diamonds), $Pe = 100$ (squares), and $Pe = 1000$ (triangles). Damköhler number Da is found to decrease for $m = 3$. This occurs because the solubility of CO_2 , and hence reaction rate, decrease with salinity. From a comparison between panel (a) and (b), we observe that for $Pe = 10$ and $Pe = 100$, t_c increases with decreasing Da . At high Peclet number $Pe = 1000$, however, t_c does not change significantly with decreasing Da and generally decreases from 5.56 when $Re = 1$ to 2.74 when $Re = 100$.

Figure 5.9(c) shows the critical time for a fracture blockage, t_c , with smooth

walls as a function of Reynolds number when $Da = 1.97 \times 10^{-2}$, $Pe = 10$ (diamonds), $Pe = 100$ (squares), and $Pe = 1000$ (triangles). Damköhler number Da is found to increase because of the higher pressure value, $P = 400$. This occurs because the solubility of CO_2 , and hence reaction rate, increase with pressure. In panel (d), Damköhler number Da is also found to increase because of the higher temperature value, $T = 100^\circ C$. This occurs because higher temperature leads to an increase in the reaction rate. Similar behavior was observed previously in Figures 3.5 and 3.6. We find qualitatively similar trends to those demonstrated in Figure 5.9(c) and (d).

5.4 Conclusion

A numerical model of geochemical transport is developed to evaluate long term mineral trapping of CO_2 inside a single fracture. The methodology developed here is employed to evaluate the effects of convection, diffusion, and chemical reactions on the dynamics of flow through a single fracture. The calculated rates of the chemical reactions between dissolved CO_2 and rock minerals that potentially contribute to mineral trapping of CO_2 are taken into account here. The transport numerical model analyzes the impact of CO_2 immobilization on porosity of the fracture through carbonate precipitation. It is found that the addition of CO_2 mass as carbonate precipitates to the solid phase leads to a decrease in porosity and permeability of the fracture.

We observe that the critical time of blockage for a single fracture decreases with increasing pressure and temperature and increases with increasing salinity. The

current numerical simulation provides useful insight into the potential sequestration capacity of a porous media, and its controlling conditions, such as the critical time of blockage of a single fracture.

It is found that the designated fracture is filled at the inlet because concentrations of carbonate ions are greater (more supersaturated states). For lower Peclet numbers ($Pe \leq 100$), the critical time for a fracture blockage, t_c , is insensitive to the Reynolds number and increases with the Peclet number. At a high Peclet number $Pe = 1000$, however, the critical time generally decreases with an increasing Reynolds number.

Chapter 6

Conclusions and future work

6.1 Conclusions

CO₂ sequestration has recently emerged as an important option for reducing greenhouse effects that perturb life-cycle balance. Modeling the storage of CO₂ in saline aquifers on a reservoir scale is very demanding with respect to computational cost. We focused on obtaining a fundamental understanding of the effect of CO₂ solubility on the rates of geochemical reactions, density of brine, and time dependent porosity variation of a single fracture. In this regard, we evaluated the CO₂ sequestration capacity of both aqueous and mineral phases. To this end, we develop a method to determine the reaction rates of minerals through transition state theory in saline aquifers containing brine and a supercritical CO₂ phase. We observed that the transition state theory can reasonably reproduce experimental data with new parameters that we obtain in the current study.

The first objective of the current study is to determine the association between the solubility of CO₂ and the kinetics of chemical reactions on the basis of the transition state theory. It has been found that the addition of CO₂ and calcium ions Ca²⁺ precipitates to calcium carbonate (calcite) which leads to a decrease in porosity and permeability of the fracture. The kinetics of the chemical reactions such as dissolution rates of calcite and anorthite have been calculated in order

to quantify the rate of mineral trapping of CO₂. Our study confirms that the dissolution rate of anorthite is the rate-limiting process in the sequestration of CO₂ under the temperature and pressure conditions of typical saline aquifers, i.e. 50 to 100°C and up to 600 bar, respectively. The rate equation of the primary minerals in saturated solutions has been determined as a function of only the parameters that are available as variables during program execution, such as pressure, temperature, and salinity, with the help of a multi-parameter nonlinear regression of semi-empirical data. We thus seek to understand the complex kinetic modeling of key reactions only. The simplification of the complex kinetic model may, however, lead to deviation from reality. This discrepancy may arise due to the factors such as nucleation, surface complexation, hydrogen bond, hydration, chemical reaction, ionization and reaction orders that could influence phase relations and reactions. However, we find that the proposed rate equation can reasonably reproduce reaction rates of minerals with new parameters that we obtain from sensitivity and multi-variant nonlinear regression studies.

The second objective of the current study was to determine the density of the brine after dissolution of CO₂. Because, modeling of CO₂ sequestration also requires an accurate estimate of the density of a saturated brine-CO₂ solution in equilibrium with supercritical CO₂. For this purpose, we have developed a new model to accurately predict the density of saturated solutions of CO₂-H₂O-NaCl. The model is based on calculating the liquid molar volume from experimental data for the density of saturated binary solutions and the corresponding mole fractions of dissolved CO₂. The density of a saturated ternary solution based on the new

model agrees well with available experimental data. In general, the solution density is found to increase with pressure and the mole fraction of dissolved CO_2 , but decreases with an increase in temperature and salinity. We have also evaluated the influence of salinity for different models for the activity of aqueous CO_2 in brine. Our parametric study indicates that the densities of binary and ternary saturated solutions increase gently at low values of mole fraction but more rapidly at larger values. The relative densities of the saturated solutions do not vary appreciably at low mole fractions. We expect that our model will significantly impact future numerical simulations of flow and reactive transport of CO_2 in brine by allowing fluid density differences to be more accurately coupled to the pressure, temperature and salinity of an aquifer.

We also investigated the effect of temperature $T \in [50, 100]^\circ\text{C}$, pressure $P \in [100, 600]$ bar, and salinity $m \in [0, 3]$ on the onset of buoyancy driven convection during CO_2 sequestration. For a given porosity and permeability, we found the onset time t_{on} can vary by one order of magnitude with variations in T , P and m . More specifically, t_{on} decreases with increasing pressure and decreasing temperature and salinity. This occurs because the solubility of CO_2 increases with pressure, but decreases with temperature and salinity. An increase in solubility increases the density difference $\Delta\rho$, and drives the onset of buoyancy driven convection. As expected from previous studies (Daniel et al., 2013; Ennis-King et al., 2003; Riaz et al., 2006; Tilton and Riaz, 2014), the onset time is highly sensitive to permeability, such that t_{on} can decrease by two orders of magnitude when the permeability increases by one order of magnitude. We conclude that high-permeability aquifers with high pressure,

low temperature and low salinity are most suitable for sequestration of CO_2 , from the standpoint of minimizing the time required for the onset of buoyancy driven convection. For these conditions, we also found that the wavelength λ_{on} at onset of convection tends to be minimized. Though beyond the scope of this study, this may have an effect on mixing, nucleation, and precipitation of secondary carbonates.

The third objective of the current study was to investigate the impact of fractures on CO_2 transport and storage capacity. The fracture permeability, an important parameter controlling CO_2 migration throughout sequestration, affects the amount of mineralization trapping of CO_2 which enhances the long-term CO_2 storage. To this end, we develop a numerical model of geochemical transport to evaluate long term mineral trapping of CO_2 inside a single fracture. The purpose of the current study is to predict the actual efficiency of the mineral trapping mechanism by considering the physical properties of the fluid such as its density, pH, and also the characteristics of the mineral compositions. The computational fluid dynamics provides detailed information at no additional cost in our investigation and consequently permits a more precise understanding of the flow processes to be obtained. It is found that the fracture is filled at the inlet because concentrations of carbonate ions are greater (more saturated states). For lower Peclet numbers ($\text{Pe} \leq 100$), the critical time for a fracture blockage, t_c , is insensitive to the Reynolds number and increases with the Peclet number. At a high Peclet number $\text{Pe} = 1000$, however, the critical time generally decreases with increasing Reynolds number.

6.2 Future work

The current study encompasses a number of diverse disciplines including fluid mechanics, geochemistry, geology, physics, chemistry, hydrology, civil and environmental engineering. This is an attempt to some extent bridge the gap between these different disciplines by bringing together authors and researchers from different backgrounds. The results of the current study can be implemented in the oil and gas industry to describe the extend and consequences of reactive flow and transport in natural subsurface systems after injection of CO₂.

There are some future opportunities for me and the other researchers to investigate the physical properties of the fracture such as its size and surface roughness. Because, in general, the two rock surfaces that bound a fracture are rough (see Figure 6.1). The surface area available for calcite cement are the essential elements of the calcite precipitation model. Therefore, an accurate study of surface roughness is also required to predict the actual efficiency of mineral trapping of CO₂ for a long period of time. The degree of roughness can be a function of the fracture aperture width and the fluid properties within the fractures (Iwano and Einstein, 1993). One of the future works is to investigate the effects of the surface roughness on permeability changes caused by the mineral precipitation qualitatively. The numerical model can analyze the impact of CO₂ immobilization through carbonate precipitation inside the two parallel walls with roughness. The physical properties of the fracture such as its size and degree of roughness should be taken into account in the future model as well as the physical properties of the fluid such as its pH. This study

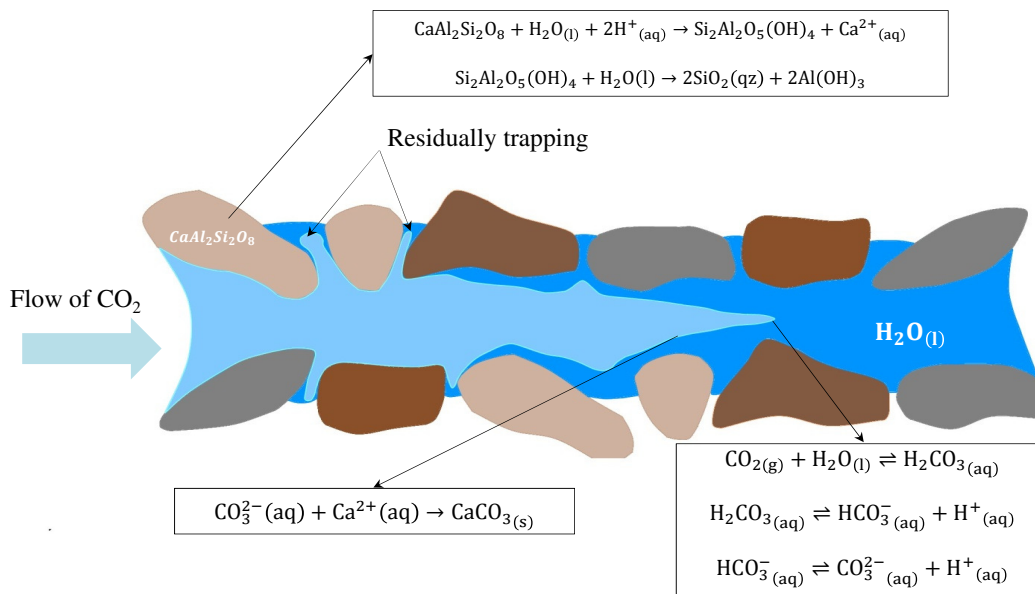


Figure 6.1: Schematic representation of mineral trapping of CO_2 inside a porous media.

may give information about the precipitation of calcite inside a fracture with non-smooth walls through geological sequestration of CO_2 . The goal is to quantitatively understand the permeability changes caused by the mineral precipitation.

This study also can be extended to focus on constructing a numerical model of real porous media which enables the value of the permeability to be predicted. A solid matrix, consisting of mineral grains and pore spaces, is referred to as a porous medium.

The porous media mineralization problem can be simplified by taking into account the chemical reactions at the solid surfaces. When the fluid is supersaturated by activities (concentrations) of species, precipitation occurs by reaction at the grains surfaces and subsequently decreases the porosity. The cementation of

carbonate can be an example of nucleation growth. The quantities describing the system at the macro-scale include the pressure, temperature, salinity, fluid density, concentration of gaseous and aqueous species, minerals compositions, porosity, and permeability.

One of the future works is to investigate the effects of the mineral precipitations on the porosity of the porous media such as magnesite (MgCO_3), siderite (FeCO_3), dolomite ($\text{CaMg}(\text{CO}_3)_2$), and dawsonite ($\text{NaAlCO}_3(\text{OH})_2$). The total porosity ϕ is defined as the fraction of volume of the rock made up of pore space:

$$\phi = \frac{V_p}{V_T} \quad (6.1)$$

where, ϕ is porosity, V_p and V_T denote the volume of the pores and total volume, respectively. The permeability κ characterizes the resistance of the porous rocks to the flow of fluid. The more permeable the porous rock, the faster fluid flows. Changes in porosity and permeability due to mineral dissolution and precipitation can affect fluid flow. This interaction between flow and chemical reactions is significant and plays a pivotal role through mineral trapping of CO_2 ; however, a large computational penalty has to be paid if this is considered explicitly in the current study. The modeling of flow and transport inside the porous media for mineral trapping purposes can also be based on space discretization by means of integral finite differences.

A small decrease in porosity may result in a significant decrease in permeability. The Kozeny- Carman equation relates the permeability κ (m^2) to the porosity

(ϕ) by the following equation:

$$\frac{\kappa}{\kappa'_o} = \left(\frac{\phi}{\phi_o}\right)^3 \left(\frac{1 - \phi_o}{1 - \phi}\right)^2 \quad (6.2)$$

where ϕ_o and κ_o are the initial porosity and permeability, respectively. ϕ and κ are the porosity and permeability, respectively. The model can monitor changes in porosity and permeability during the simulation from changes in the volume of the pores and total volume. Therefore, a new improved model may be obtained based on the future investigation of the porous media by means of the current study. The range of problems concerning the interaction of water-CO₂-minerals is very broad because mineral kinetic properties and reactive surface areas are not well constrained. The numerical modeling, however, may give us a decent understanding of the sequestration processes.

Chapter 7

Appendix

A.1 Solubility of CO₂ as a function of pressure, temperature and salinity

Assuming brine to be made up of H₂O and NaCl, the solubility of CO_{2(aq)} in brine can be quantified by the mole fraction, x_{CO_2} , given by

$$x_{\text{CO}_2} = \frac{m_{\text{CO}_2}}{m_{\text{CO}_2} + m_{\text{H}_2\text{O}} + 2 m_{\text{NaCl}}} , \quad (1)$$

where m_{CO_2} , $m_{\text{H}_2\text{O}}$ and m_{NaCl} denote, respectively, the molality of CO₂, H₂O and NaCl in the solution. The factor of 2 for m_{NaCl} is due to the complete dissociation of dissolved NaCl into Na⁺ and Cl⁻ ions. Molality of CO₂ can be expressed as the ratio, $m_{\text{CO}_2} = a_{\text{CO}_2} / \gamma_{\text{CO}_2}$, of the activity, a_{CO_2} , of CO₂ in the solution and the activity coefficient, γ_{CO_2} . The activity of dissolved CO₂ and the fugacity in the CO₂ rich phase, f_{CO_2} , are related through the equilibrium constant, $K = f_{\text{CO}_2} / a_{\text{CO}_2}$. Using these relations, the mole fraction of CO₂ in Eq. (1) can be expressed as

$$x_{\text{CO}_2} = \frac{f_{\text{CO}_2}}{f_{\text{CO}_2} + (m_{\text{H}_2\text{O}} + 2 m_{\text{NaCl}}) K \gamma_{\text{CO}_2}} , \quad (2)$$

Figure 1 depicts the variation of activity coefficient of aqueous CO₂ in NaCl solutions with different molalities. Activity coefficient of CO₂ increases with the

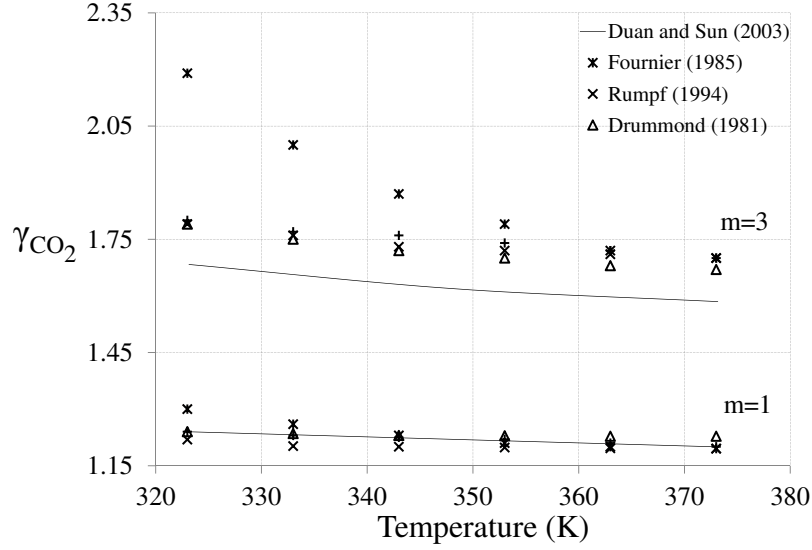


Figure 1: Activity coefficients for aqueous CO_2 at 1 bar pressure from various sources for 1 and 3 mol/kg NaCl aqueous solutions in the temperature range of 50-100°C. Activity coefficient of CO_2 increases with molality of NaCl, m , and decreases with temperature.

molality of NaCl. In most cases higher temperatures lead to a decrease in the activity coefficient, which would indicate a lower solubility based on Eq. 2. However an increase in temperature also affects fugacity, f_{CO_2} , and the equilibrium constant, K , in Eq. 2, as described in more detail below. Hence, an increase in temperature is not always accompanied by an increase in solubility.

In order to find the mole fraction of CO_2 in the solution for particular molalities of H_2O and NaCl, corresponding values of the activity coefficient, the equilibrium constant (Krauskopf and Bird, 1995) and fugacity need to be determined.

Following Marini (2007), the equilibrium constant, K , in Eq. 2 is given by

$$K = K^\circ \exp \left[\frac{\bar{V}_{\text{CO}_2}}{R T} (P - P^\circ) \right], \quad (3)$$

where, R , T and P are, respectively, the ideal gas constant, temperature and pressure. P° is the standard pressure and $\bar{V}_{\text{CO}_2} = 32.6 \text{ cm}^3/\text{mol}$ is the average partial molar volume of CO_2 in the temperature range, ($T < 100^\circ\text{C}$) and pressure range up to 600 bar (Marini, 2007). In this range of temperatures, the equilibrium constant at standard pressure, K° , can be obtained for the supercritical, $K_{(g)}^\circ$, and the subcritical, $K_{(l)}^\circ$, states of the CO_2 rich phase as

$$\log_{10}K_{(g)}^\circ = 1.189 + 0.01304 T - 5.446 \times 10^{-5} T^2, \quad (4)$$

$$\log_{10}K_{(l)}^\circ = 1.169 + 0.01368 T - 5.380 \times 10^{-5} T^2, \quad (5)$$

where, $K_{(g)}^\circ$ is used when the temperature and the volume of the gas phase are above the critical parameters of CO_2 , 31°C and $94 \text{ cm}^3 \text{ mol}^{-1}$, respectively. $K_{(l)}^\circ$ is given by Eq. (5), is used when the temperature and the volume of the gas phase are below the critical parameters of CO_2 .

The fugacity for the CO_2 rich phase in the supercritical state is determined from the following relation,

$$f_{\text{CO}_2} = \phi y_{\text{CO}_2} P, \quad (6)$$

where, ϕ and y_{CO_2} are, respectively, the fugacity coefficient and the mole fraction of CO_2 in the supercritical phase. For the range of pressures (up to 600 bar) and temperatures ($50\text{-}100^\circ\text{C}$) concerned with CO_2 sequestration problem, for calculating the fugacity of CO_2 , Spycher and Pruess (2010b) have shown that that mole fraction of H_2O in the compressed gas phase can be neglected when $T \leq 100^\circ\text{C}$ because of the negligible amount of H_2O in the CO_2 rich phase (Spycher et al., 2003). The

Table 1: Values of the coefficients used in the Redlich-Kwong equation.

| | Value | Units |
|---|---|--|
| Q | $7.54 \times 10^7 - 3.96 \times 10^4 T(\text{K})$ | bar cm ⁶ K ^{0.5} mol ⁻² |
| S | 27.80(±0.01) | cm ³ /mol |

fugacity coefficient of CO₂, ϕ , is then given by

$$\ln \phi = \ln \left(\frac{v}{v-S} \right) + \frac{S}{v-S} - \frac{3Q}{SRT^{3/2}} \left[\ln \left(\frac{v+S}{v} \right) - \frac{S}{3(v+S)} \right] - \ln Z, \quad (7)$$

where v is the molar volume of CO₂, $Z = Pv/RT$ is the compressibility factor of the CO₂ rich phase and Q and S are the correcting factors that are given in Table 1 (Spycher and Pruess, 2010a) for the temperature range of 283–380 K. Molar volumes of CO₂ for temperatures between 50 to 100°C and pressures up to 600 bar in the gas phase and the aqueous phase can be obtained with the equation of state given by Spycher and Pruess (2010b) and Duan et al. (1992), respectively.

$$v^3 - \frac{RT}{P}v^2 - \left(\frac{RTS}{P} - \frac{Q}{T^{1/2}P} + S^2 \right) v - \frac{QS}{T^{1/2}P} = 0. \quad (8)$$

The maximum root of Eq. 8, v_{\max} , gives the molar volume of CO₂ in the gas phase while the molar volume in the liquid phase is supposedly given by the minimum root, v_{\min} (Marini, 2007). The molar volume in the gas phase, v_{\max} allows the calculation of the fugacity coefficient, ϕ , from Eq. (7), which yields the value of fugacity, f_{CO_2} , from Eq. (6) for a given pressure, P .

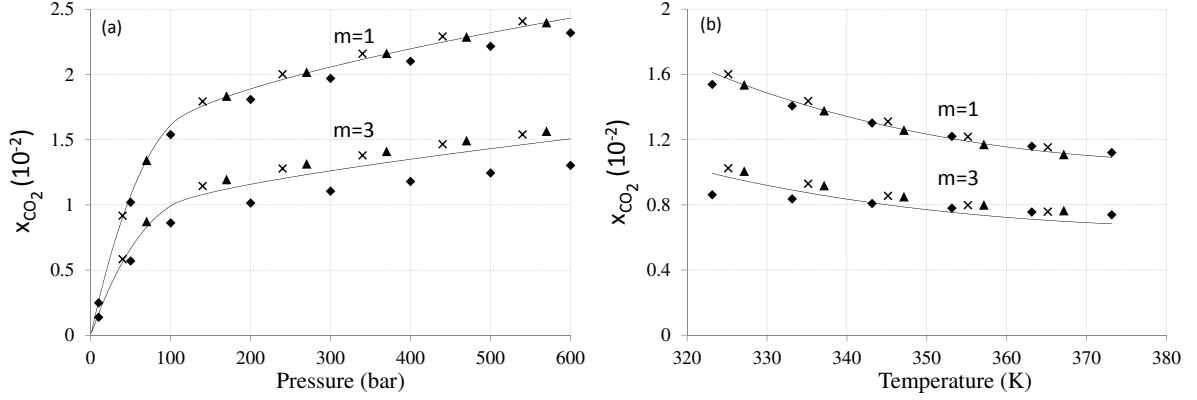


Figure 2: The calculated values of mole fraction of CO_2 by means of Eq. 2 based on various activity coefficient models; Duan and Sun (2003) (solid lines), Rumpf et al. (1994) (crosses), Fournier (1985) (diamonds), Drummond (1981) (triangle). (a) $T = 50^\circ\text{C}$ and (b) $P = 100$ bar. The solubility of CO_2 increases with pressure. Higher temperature and salinity values lower solubility.

We evaluate the solubility of CO_2 for various values of temperature, pressure and salinity based on various activity coefficients in saline water in Figure 2. We find that at 50°C the solubility based on the activity coefficients of Duan and Sun (2003), Rumpf (1994) and Drummond are in good agreement. The solubility calculation based on the activity coefficients of Fournier (1985), however, gives lower mole fractions of dissolved CO_2 compared to others. This variation is more pronounced at higher pressure, temperature and salinity values. Figure 2 also shows that the mole fraction of CO_2 increases with pressure. However, higher temperatures and salinities lead to a decrease in the mole fraction.

B.1 Dependence of pH on pressure, temperature and salinity

The dissociation constant of water, K_w , has been studied by several researchers. The model of Marshall and Franck (1981) is more reliable under aquifer conditions and will be employed in the current study to find the total concentration of $[H^+]$. The total concentration of species in the aqueous phase is given by

$$C_T = [H_2CO_3] + [HCO_3^-] + [CO_3^{2-}] . \quad (9)$$

Carbonic acid, H_2CO_3 , has two protons which may dissociate from the original molecule and make the brine acidic (Li and Duan, 2007; Meyssami et al., 1992). Thus, there are two dissociation constants. The first represents the dissociation into the bicarbonate (also called hydrogen carbonate) ion,

$$K_{a1} = \frac{[HCO_3^-][H^+]}{[H_2CO_3]} . \quad (10)$$

The first dissociation constant of carbonic acid $K_{a1} = k_d/k_r = 4.6 \times 10^{-7}$ at $25^\circ C$, where k_d is the rate constant for dissociation and k_r is the rate constant for acid recombination. The dissociation rate of carbonic acid is very fast ($k_d = 8 \times 10^5 s^{-1}$) (Brezonik and Arnold, 2011), therefore the kinetics of this reaction does not concern us further. In the current study, the values for K_{a1} are obtained from the model of Read (1975) at different temperatures and pressures. The second dissociation constant, K_{a2} , for the dissociation of bicarbonate ion into carbonate ion, CO_3^{2-} , is given by

$$K_{a2} = \frac{[CO_3^{2-}][H^+]}{[HCO_3^-]} . \quad (11)$$

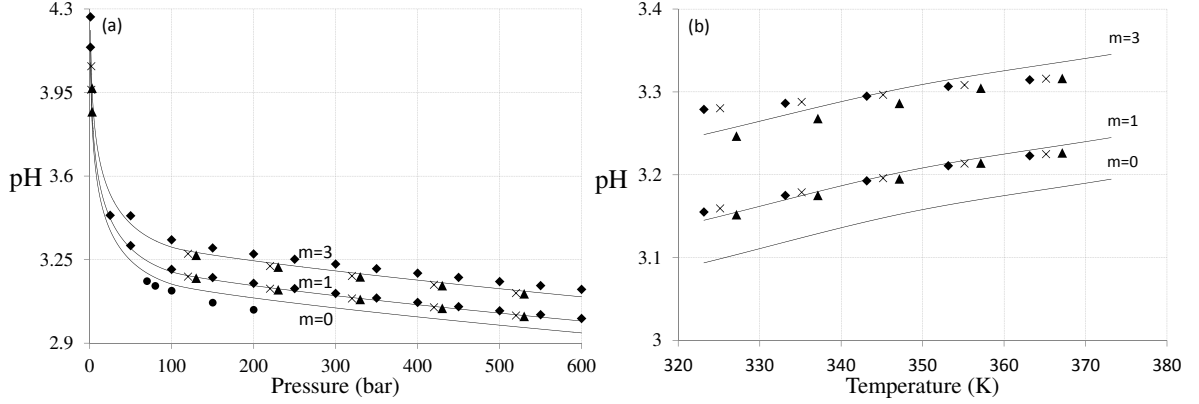


Figure 3: The pH variation of binary solution, H₂O-CO₂, for different values of salinity based on various activity coefficient models; Duan and Sun (2003) (solid lines), Rumpf et al. (1994) (crosses), Fournier (1985) (diamonds), Drummond (1981) (triangle). Experimental data of Toews et al. (1995) for $m = 0$ is shown with circles. (a) $T = 50^\circ\text{C}$ and (b) $P = 100$ bar.

The second dissociation constant is $K_{a2} = 4.68 \times 10^{-11}$ at 25°C , which is negligible compared to K_{a1} (Mehrbach et al., 1973) and can be neglected in Eq. 3.5.

At the macroscopic scale an aqueous solution is found to be electrically neutral (Stumm, 1970), therefore, charge must be conserved. The electro neutrality condition is

$$[\text{H}^+] + [\text{Na}^+] = 2[\text{CO}_3^{2-}] + [\text{HCO}_3^-] + [\text{OH}^-] + [\text{Cl}^-] . \quad (12)$$

Molarity of Na^+ and Cl^- are equal to molality of NaCl (Li and Duan, 2007). Substituting concentration of $[\text{H}_2\text{CO}_3]$ and $[\text{HCO}_3^-]$ from Eq. 10 and 11 into the Eq. 9 we find

$$\begin{aligned}
C_T &= \frac{[\text{H}^+]^2[\text{CO}_3^{2-}]}{K_{a1}K_{a2}} + \frac{[\text{H}^+][\text{CO}_3^{2-}]}{K_{a2}} + [\text{CO}_3^{2-}] \\
&= [\text{CO}_3^{2-}] \left(1 + \frac{[\text{H}^+]}{K_{a2}} + \frac{[\text{H}^+]^2}{K_{a1}K_{a2}} \right) .
\end{aligned} \tag{13}$$

Therefore, concentrations of deprotonated forms HCO_3^- (bicarbonate) and CO_3^{2-} (carbonate) depend on the concentration of $[\text{H}^+]$ (Stumm, 1970).

$$[\text{CO}_3^{2-}] = \frac{K_{a1}K_{a2}C_T}{[\text{H}^+]^2 + K_{a1}[\text{H}^+] + K_{a1}K_{a2}} . \tag{14}$$

$$[\text{HCO}_3^-] = \frac{K_{a1}[\text{H}^+]C_T}{[\text{H}^+]^2 + K_{a1}[\text{H}^+] + K_{a1}K_{a2}} . \tag{15}$$

Substituting these into the electro neutrality condition, Eq. 12, and combining it with $K_w = [\text{H}^+][\text{OH}^-]$ we derive a 4th degree equation in $[\text{H}^+]$:

$$[\text{H}^+] = C_T \frac{2K_{a1}K_{a2} + K_{a1}[\text{H}^+]}{[\text{H}^+]^2 + K_{a1}[\text{H}^+] + K_{a1}K_{a2}} + \frac{K_w}{[\text{H}^+]} . \tag{16}$$

The condition, $K_{a1} \gg K_{a2}$ and $K_{a1}[\text{H}^+] \gg K_{a2}[\text{H}^+]$, allows the following simplification

$$\begin{aligned}
\frac{2K_{a1}K_{a2} + K_{a1}[\text{H}^+]}{[\text{H}^+]^2 + K_{a1}[\text{H}^+] + K_{a1}K_{a2}} &\approx \frac{2K_{a1}K_{a2} + K_{a1}[\text{H}^+] + K_{a2}[\text{H}^+]}{[\text{H}^+]^2 + K_{a1}[\text{H}^+] + K_{a1}K_{a2} + K_{a2}[\text{H}^+]} \\
&= \frac{K_{a1}}{K_{a1} + [\text{H}^+]} + \frac{K_{a2}}{K_{a2} + [\text{H}^+]} .
\end{aligned} \tag{17}$$

Substituting Eq. 17 into the Eq. 16 we find

$$[\text{H}^+] = \frac{K_{a1}}{K_{a1} + [\text{H}^+]} C_T + \frac{K_{a2}}{K_{a2} + [\text{H}^+]} C_T + \frac{K_w}{[\text{H}^+]} . \tag{18}$$

Finally, pH is the negative logarithm of the activity of hydrogen ions in solution, $\text{pH} = -\text{Log}_{10} [\text{H}^+]$. For the acidic range (Hellmann, 1994) where the concentration of $[\text{H}^+]$ is higher, assuming that $K_{a2} \ll K_{a1} \ll [\text{H}^+]$ can help simplifying the equation even further to Eq. 3.5.

Figure 3 depicts the variation of pH with respect to changes in pressure, for $T=50^\circ\text{C}$, and changes in temperature, for $P=100$ bar, in plots (a) and (b), respectively. Three different levels of salinity, $m=0, 1$ and 3 , are considered. As a function of pressure, pH drops rapidly when the pressure, P , increases from 1 bar to around 100 bar for all values of m , as shown in Fig. 3(a). For $P > 100$ bar, pH decays relatively slowly and at a constant rate. Values of pH based on different activity coefficients are found to be quite similar for both cases of $m=1$ and $m=3$. As a function of temperature, pH increases at a relatively constant rate, as shown in Fig. 3(b). The difference in pH based on different models of the activity coefficient is small for $m=1$ but increases for $m=3$, particularly at smaller values of the temperature. The pH variation shown in Fig. 3 generally follows the trend of the underlying solubility behavior observed in Figure 2, i.e., an increase in the mole fraction with pressure and a decrease in the mole fraction with temperature. In the same range of pressure, larger values of temperature and salinity tend to lower the solubility of CO_2 in brine, which limits the pH reduction.

Figure 3(a) also compares the computed values of pH with those measured experimentally for the $\text{H}_2\text{O}-\text{CO}_2$ system by Toews et al. (1995). The experimentally determined values of pH at 50°C vary from 3.03 to 3.16 for the pressure range of about 70-200 bar. A comparison with calculated pH values in Fig. 3(a) indicates a

close similarity. Though a slight deviation is observed to set in for larger values of the pressure. This small discrepancy is due perhaps to different CO_2 mole fractions and ionic strengths used in the experiment. The $[\text{H}^+]$ generated by dissolution of CO_2 will enhance dissolution of mineral compositions to consume available $[\text{H}^+]$ in the aqueous phase which may buffers the pH of the system. Due to the generation of cation- HCO_3^- complexation, the capacity of the brine will also increase to contain dissolved CO_2 . Additionally, direct measurement of K_{a1} and K_{a2} itself may involve errors. For example, Ellis (1959a) cites errors up to 20% in conductivity measurements used in the determination of K_{a1} and K_{a2} values. Nevertheless, this comparison with experimental measurements of pH is encouraging and helps build confidence in the application of the model to $m>0$ cases.

Bibliography

- Aagaard, P. and Helgeson, H. (1977). Thermodynamic and kinetic constraints on the dissolution of feldspars. *Geol. Soc. Am., Abstr. Programs;(United States)*, 9(7).
- Aagaard, P. and Helgeson, H. (1982). Thermodynamic and kinetic constraints on reaction rates among minerals and aqueous solutions; I, theoretical considerations. *American journal of Science*, 282(3):237.
- Akinfiev, N. N. and Diamond, L. W. (2010). Thermodynamic model of aqueous $\text{CO}_2 - \text{H}_2\text{O} - \text{NaCl}$ solutions from -22 to 100°C and from 0.1 to 100MPa. *Fluid Phase Equilibria*, 295(1):104–124.
- Alkan, H., Cinar, Y., and Ülker, E. (2010). Impact of capillary pressure, salinity and in situ conditions on CO_2 injection into saline aquifers. *Transport in porous media*, pages 1–21.
- Allen, D., Strazisar, B., Soong, Y., and Hedges, S. (2005). Modeling carbon dioxide sequestration in saline aquifers: Significance of elevated pressures and salinities. *Fuel processing technology*, 86(14):1569–1580.
- Bachu, S., Gunter, W., and Perkins, E. (1994). Aquifer disposal of CO_2 : Hydrodynamic and mineral trapping. *Energy Conversion and Management*, 35(4):269–279.
- Bando, S., Takemura, F., Nishio, M., Hihara, E., and Akai, M. (2004). Viscosity of aqueous NaCl solutions with dissolved CO_2 at (30 to 60) C and (10 to 20) MPa. *Journal of Chemical & Engineering Data*, 49(5):1328–1332.
- Barta, L. and Bradley, D. (1985). Extension of the specific interaction model to include gas solubilities in high temperature brines. *Geochimica et cosmochimica Acta*, 49(1):195–203.
- Berner, R. A., Lasaga, A. C., and Garrels, R. M. (1983). The carbonate-silicate geochemical cycle and its effect on atmospheric carbon dioxide over the past 100 million years. *Am. J. Sci*, 283(7):641–683.
- Bernstein, L., Bosch, P., Canziani, O., Chen, Z., Christ, R., Davidson, O., Hare, W., Huq, S., Karoly, D., Kattsov, V., et al. (2008). Climate change 2007: Synthesis report: An assessment of the intergovernmental panel on climate change.
- Bethke, C. (2008). *Geochemical and biogeochemical reaction modeling*, volume 543. Cambridge University Press Cambridge, UK.
- Black, J. R. and Haese, R. R. (2014). Chlorite dissolution rates under CO_2 saturated conditions from 50 to 120°C and 120 to 200 bar CO_2 . *Geochimica et Cosmochimica Acta*, 125:225–240.

- Blencoe, J. G., Naney, M. T., and Anovitz, L. M. (2001). The CO₂-H₂O system: III. a new experimental method for determining liquid-vapor equilibria at high subcritical temperatures. *American Mineralogist*, 86(9):1100–1111.
- Bodnar, R. J., Steele-MacInnis, M., Capobianco, R. M., Rimstidt, J. D., Dilmore, R., Goodman, A., and Guthrie, G. (2013). PVTX properties of H₂O-CO₂-salt at PTX conditions applicable to carbon sequestration in saline formations. *Reviews in Mineralogy and Geochemistry*, 77(1):123–152.
- Bolourinejad, P., Shoeibi Omrani, P., and Herber, R. (2014). Effect of reactive surface area of minerals on mineralization and carbon dioxide trapping in a depleted gas reservoir. *International Journal of Greenhouse Gas Control*, 21:11–22.
- Bragg, W. (1914). The analysis of crystals by the X-ray spectrometer. *Proceedings of the Royal Society of London. Series A*, 89(613):468–489.
- Brezonik, P. and Arnold, W. (2011). *Water chemistry: an introduction to the chemistry of natural and engineered aquatic systems*. Oxford University Press.
- Brown, A. M. (2001). A step-by-step guide to non-linear regression analysis of experimental data using a microsoft excel spreadsheet. *Computer methods and programs in Biomedicine*, 65(3):191–200.
- Brown, I. and Shannon, R. (1973). Empirical bond-strength-bond-length curves for oxides. *Acta Crystallographica Section A: Crystal Physics, Diffraction, Theoretical and General Crystallography*, 29(3):266–282.
- Busch, A., Amann-Hildenbrand, A., Bertier, P., Waschbuesch, M., and Krooss, B. (2010). The significance of caprock sealing integrity for CO₂ storage. In *SPE International Conference on CO₂ Capture, Storage, and Utilization*.
- Carroll, S. A. and Knauss, K. G. (2005). Dependence of labradorite dissolution kinetics on CO₂(aq), Al(aq), and temperature. *Chemical Geology*, 217(3):213–225.
- Chou, L., Garrels, R., and Wollast, R. (1989). Comparative study of the kinetics and mechanisms of dissolution of carbonate minerals. *Chemical Geology*, 78(3-4):269–282.
- Cramer, S. (1982). The solubility of methane, carbon dioxide, and oxygen in brines from 0 to 300 p0 sc.
- Crovetto, R. and Wood, R. (1992). Solubility of CO₂ in water and density of aqueous CO₂ near the solvent critical temperature. *Fluid phase equilibria*, 74:271–288.
- Dalkhaa, C., Shevalier, M., Nightingale, M., and Mayer, B. (2013). 2-D reactive transport modeling of the fate of CO₂ injected into a saline aquifer in the wabamun lake area, alberta, canada. *Applied Geochemistry*, 38:10–23.

- Daniel, D., Tilton, N., and Riaz, A. (2013). Optimal perturbations of gravitationally unstable, transient boundary layers in porous media. *Journal of Fluid Mechanics*, 727:456–487.
- Daval, D., Martinez, I., Corvisier, J., Findling, N., Goffé, B., and Guyot, F. (2009). Carbonation of ca-bearing silicates, the case of wollastonite: Experimental investigations and kinetic modeling. *Chemical Geology*, 265(1):63–78.
- Drummond, S. (1981). *Boiling and mixing of hydrothermal fluids: chemical effects on mineral precipitation*. Pennsylvania State University.
- Duan, Z., Hu, J., Li, D., and Mao, S. (2008). Densities of the CO₂-H₂O and CO₂-H₂O-NaCl systems up to 647 K and 100 MPa. *Energy & Fuels*, 22(3):1666–1674.
- Duan, Z., Møller, N., and Weare, J. H. (1992). An equation of state for the CH₄ – CO₂ – H₂O system: II. mixtures from 50 to 1000°C and 0 to 1000 bar. *Geochimica et Cosmochimica Acta*, 56(7):2619–2631.
- Duan, Z. and Sun, R. (2003). An improved model calculating CO₂ solubility in pure water and aqueous nacl solutions from 273 to 533 K and from 0 to 2000 bar. *Chemical Geology*, 193(3):257–271.
- Dufaud, F., Martinez, I., and Shilobreeva, S. (2009). Experimental study of mg-rich silicates carbonation at 400 and 500 C and 1 kbar. *Chemical Geology*, 265(1):79–87.
- Ellis, A. (1959a). 750. The effect of pressure on the first dissociation constant of carbonic acid. *J. Chem. Soc.*, pages 3689–3699.
- Ellis, A. (1959b). The solubility of carbon dioxide in water at high temperatures. *American Journal of Science*, 257(3):217–234.
- Ellis, A. and Golding, R. (1963). The solubility of carbon dioxide above 100 degrees C in water and in sodium chloride solutions. *American Journal of Science*, 261(1):47.
- Enick, R. M. and Klara, S. M. (1990). CO₂ solubility in water and brine under reservoir conditions. *Chemical Engineering Communications*, 90(1):23–33.
- Ennis-King, J., Preston, I., and Paterson, L. (2003). Onset of convection in anisotropic porous media subject to a rapid change in boundary conditions. *Phys. Fluids*, 17:Article no. 084107.
- Escobedo-Alvarado, G. N., Sandler, S. I., and Scurto, A. M. (2001). Modeling of solid–supercritical fluid phase equilibria with a cubic equation of state G_{ex} model. *The Journal of Supercritical Fluids*, 21(2):123–134.
- Fei, Y. (1995). Thermal expansion. *Mineral physics and crystallography: a handbook of physical constants*, 2:29–44.

- Fenghour, A., Wakeham, W., and Watson, J. (1996). Densities of (water+ carbon dioxide) in the temperature range 415 K to 700 K and pressures up to 35 MPa. *The Journal of Chemical Thermodynamics*, 28(4):433–446.
- Flaathen, T., Oelkers, E., Gislason, S., Aagaard, P., et al. (2011). The effect of dissolved sulphate on calcite precipitation kinetics and consequences for subsurface CO₂ storage. *Energy Procedia*, 4:5037–5043.
- Fournier, R. (1985). Carbonate transport and deposition in the epithermal environment. *Reviews in economic geology*, 2:63–72.
- Gaus, I. (2010). Role and impact of CO₂–rock interactions during CO₂ storage in sedimentary rocks. *International Journal of Greenhouse Gas Control*, 4(1):73–89.
- Gaus, I., Azaroual, M., and Czernichowski-Lauriol, I. (2005). Reactive transport modelling of the impact of CO₂ injection on the clayey cap rock at sleipner (north sea). *Chemical Geology*, 217(3):319–337.
- Giammar, D. E., Bruant Jr, R. G., and Peters, C. A. (2005). Forsterite dissolution and magnesite precipitation at conditions relevant for deep saline aquifer storage and sequestration of carbon dioxide. *Chemical Geology*, 217(3):257–276.
- Gislason, S., Wolff-Boenisch, D., Stefansson, A., Oelkers, E., Gunnlaugsson, E., Sigurdardottir, H., Sigfusson, B., Broecker, W., Matter, J., Stute, M., et al. (2010). Mineral sequestration of carbon dioxide in basalt: A pre-injection overview of the carbfix project. *International Journal of Greenhouse Gas Control*, 4(3):537–545.
- Green, C. P. and Ennis-King, J. (2010). Effect of vertical heterogeneity on long-term migration of CO₂ in saline formations. *Transport in porous media*, 82(1):31–47.
- Gunter, W., Wiwehar, B., and Perkins, E. (1997). Aquifer disposal of CO₂-rich greenhouse gases: extension of the time scale of experiment for CO₂-sequestering reactions by geochemical modelling. *Mineralogy and Petrology*, 59(1):121–140.
- Guyot, F., Daval, D., Dupraz, S., Martinez, I., Ménez, B., and Sissmann, O. (2011). CO₂ geological storage: The environmental mineralogy perspective. *Comptes Rendus Geoscience*, 343(2):246–259.
- Hänchen, M., Prigiobbe, V., Storti, G., Seward, T., and Mazzotti, M. (2006). Dissolution kinetics of forsteritic olivine at 90–150°C including effects of the presence of CO₂. *Geochimica et Cosmochimica Acta*, 70(17):4403–4416.
- Hangx, S. J. and Spiers, C. J. (2009). Reaction of plagioclase feldspars with CO₂ under hydrothermal conditions. *Chemical Geology*, 265(1):88–98.
- Harlow, F. H. and Welch, J. E. (1965). Numerical calculation of time-dependent viscous incompressible flow of fluid with free surface. *Physics of fluids*, 8:2182.

- Haszeldine, R., Quinn, O., England, G., Wilkinson, M., Shipton, Z., Evans, J. P., Heath, J., Crossey, L., Ballentine, C., and Graham, C. (2005). Natural geochemical analogues for carbon dioxide storage in deep geological porous reservoirs, a united kingdom perspective. *Oil & gas science and technology*, 60(1):33–49.
- Haugan, P. and Drange, H. (1992). Sequestration of CO₂ in the deep ocean by shallow injection.
- Hawthorne, S., Miller, D., Holubnyak, Y., Harju, J., Kutchko, B., and Strazisar, B. (2011). Experimental investigations of the effects of acid gas (H₂S/CO₂) exposure under geological sequestration conditions. *Energy Procedia*, 4:5259–5266.
- He, S. and Morse, J. (1993). The carbonic acid system and calcite solubility in aqueous Na-K-Ca-Mg-Cl-SO₄ solutions from 0 to 90°C. *Geochimica et Cosmochimica Acta*, 57(15):3533–3554.
- Helgeson, H. (1969). Thermodynamics of hydrothermal systems at elevated temperatures and pressures. *American Journal of Science*, 267(7):729.
- Hellevang, H. and Aagaard, P. (2010). Can carbonate precipitation rates be derived from dissolution rate data? *Geochimica et Cosmochimica Acta*, 74(11 Suppl 1):A396.
- Hellmann, R. (1994). The albite-water system: Part i. the kinetics of dissolution as a function of pH at 100, 200 and 300C. *Geochimica et Cosmochimica Acta*, 58(2):595–611.
- Hitchon, B. (1996). Aquifer disposal of carbon dioxide. *Sherwood Park, Alberta, Canada, Geoscience Publishing Limited*.
- Hu, J., Duan, Z., Zhu, C., Chou, I., et al. (2007). Pvtx properties of the CO₂-H₂O and CO₂-H₂O-NACL systems below 647K: assessment of experimental data and thermodynamic models. *Chemical geology*, 238(3):249–267.
- Icenhower, J. and Dove, P. (2000). The dissolution kinetics of amorphous silica into sodium chloride solutions: effects of temperature and ionic strength. *Geochimica et Cosmochimica Acta*, 64(24):4193–4203.
- IEA (2008). Aquifer storage - development issues, IEA greenhouse gas R&D programme (IEAGHG). *Report No. 2008/12*.
- Iwano, M. and Einstein, H. H. (1993). Stochastic analysis of surface roughness, aperture and flow in a single fracture. In *ISRM International Symposium-EUROCK 93*.
- Jacobson, R. and Langmuir, D. (1974). Dissociation constants of calcite and CaHCO₃⁺ from 0 to 50 C. *Geochimica et Cosmochimica Acta*, 38(2):301–318.

- Javaheri, M., Abedi, J., and Hassanzadeh, H. (2010). Linear stability analysis of double-diffusive convection in porous media, with application to geological storage of CO₂. *Transport in porous media*, 84(2):441–456.
- Johnson, J. W., Nitao, J. J., and Morris, J. P. (2005). Reactive transport modeling of cap rock integrity during natural and engineered CO₂ storage. *Carbon dioxide capture for storage in deep geologic formations*, 2:787–813.
- Kell, G. (1975). Density, thermal expansivity, and compressibility of liquid water from 0. deg. to 150. deg.. correlations and tables for atmospheric pressure and saturation reviewed and expressed on 1968 temperature scale. *Journal of Chemical and Engineering Data*, 20(1):97–105.
- Ketzer, J., Iglesias, R., Einloft, S., Dullius, J., Ligabue, R., and De Lima, V. (2009). Water–rock–CO₂ interactions in saline aquifers aimed for carbon dioxide storage: Experimental and numerical modeling studies of the rio bonito formation (permian), southern brazil. *Applied geochemistry*, 24(5):760–767.
- King, M., Mubarak, A., Kim, J., and Bott, T. (1992). The mutual solubilities of water with supercritical and liquid carbon dioxides. *The Journal of Supercritical Fluids*, 5(4):296–302.
- Kissinger, H. (1957). Reaction kinetics in differential thermal analysis. *Analytical chemistry*, 29(11):1702–1706.
- Knauss, K. G., Johnson, J. W., and Steefel, C. I. (2005). Evaluation of the impact of CO₂, co-contaminant gas, aqueous fluid and reservoir rock interactions on the geologic sequestration of CO₂. *Chemical geology*, 217(3):339–350.
- Koschel, D., Coxam, J., Rodier, L., and Majer, V. (2006). Enthalpy and solubility data of CO₂ in water and NaCl_(aq) at conditions of interest for geological sequestration. *Fluid phase equilibria*, 247(1-2):107–120.
- Krauskopf, K. and Bird, D. (1995). Surface chemistry: the solution-mineral interface. *Introduction to geochemistry (Ed MG-HI Editions) Mc Graw-Hill International Editions edn, Earth Sciences and Geology Series*, pages 135–163.
- Kumar, A., Noh, M., Pope, G., Sepehrnoori, K., Bryant, S., and Lake, L. (2004). Reservoir simulation of CO₂ storage in deep saline aquifers: Tulsa, oklahoma, usa, 17-21 april 2004. In *Proceedings presented at the SPE/DOE 14th Symposium on Improved Oil Recovery, Paper SPE-89343*.
- Kumar, A., Yuan, X., Sahu, A., Dewulf, J., Ergas, S., and Van Langenhove, H. (2010). A hollow fiber membrane photo-bioreactor for CO₂ sequestration from combustion gas coupled with wastewater treatment: a process engineering approach. *Journal of Chemical Technology and Biotechnology*, 85(3):387–394.
- Laidler, K. J. and King, M. C. (1983). Development of transition-state theory. *The Journal of physical chemistry*, 87(15):2657–2664.

- Lasaga, A. (1998). *Kinetic theory in the earth sciences*. Princeton Univ Pr.
- Lasaga, A. C. (1981). Transition state theory. *Rev. Mineral.:(United States)*, 8.
- Lasaga, A. C. (1992). Ab initio methods in mineral surface reactions. *Reviews of Geophysics*, 30(4):269–303.
- Lasaga, A. C. (1995). Fundamental approaches in describing mineral dissolution and precipitation rates. *Reviews in Mineralogy and Geochemistry*, 31(1):23–86.
- Lasdon, L. S., Waren, A. D., Jain, A., and Ratner, M. (1978). Design and testing of a generalized reduced gradient code for nonlinear programming. *ACM Transactions on Mathematical Software (TOMS)*, 4(1):34–50.
- Laubach, S. (2003). Practical approaches to identifying sealed and open fractures. *AAPG bulletin*, 87(4):561–579.
- Laubach, S., Marrett, R., and Olson, J. (2000). New directions in fracture characterization. *The Leading Edge*, 19(7):704–711.
- Lemmon, E., McLinden, M., Friend, D., Linstrom, P., and Mallard, W. (2003). NIST chemistry webbook. *NIST Standard Reference Database*, (69).
- Li, D. and Duan, Z. (2007). The speciation equilibrium coupling with phase equilibrium in the H₂O – CO₂ – NaCl system from 0 to 250°C, from 0 to 1000 bar, and from 0 to 5 molality of nacl. *Chemical Geology*, 244(3):730–751.
- Li, D., Graupner, B. J., and Bauer, S. (2011). A method for calculating the liquid density for the CO₂-H₂O-NaCl system under CO₂ storage condition. *Energy Procedia*, 4:3817–3824.
- Li, Z., Dong, M., Li, S., and Dai, L. (2004). Densities and solubilities for binary systems of carbon dioxide+ water and carbon dioxide+ brine at 59C and pressures to 29 MPa. *Journal of Chemical & Engineering Data*, 49(4):1026–1031.
- Liu, F., Lu, P., Zhu, C., and Xiao, Y. (2011). Coupled reactive flow and transport modeling of CO₂ sequestration in the mt. simon sandstone formation, midwest usa. *International Journal of Greenhouse Gas Control*, 5(2):294–307.
- Liu, Q. and Maroto-Valer, M. M. (2013). Experimental studies on mineral sequestration of CO₂ with buffer solution and fly ash in brines. *Energy Procedia*, 37:5870–5874.
- Luo, S., Xu, R., and Jiang, P. (2012). Effect of reactive surface area of minerals on mineralization trapping of CO₂ in saline aquifers. *Petroleum Science*, 9(3):400–407.
- Ma, J. and Yoon, R.-H. (2013). Use of reactive species in water for CO₂ mineralization. *Energy & Fuels*.

- Marini, L. (2007). *Geological sequestration of carbon dioxide: thermodynamics, kinetics, and reaction path modeling*, volume 11. Elsevier Science.
- Markgraf, S. A. and Reeder, R. J. (1985). High-temperature structure refinements of calcite and magnesite. *American Mineralogist*, 70(5-6):590–600.
- Marshall, W. and Franck, E. (1981). *Ion Product of Water Substance, 0-1000C, 1-10,000 bars: New International Formulation and Its Background*. American Chemical Society and the American Institute of Physics for the National Bureau of Standards.
- Mehrbach, C., Culberson, C., Hawley, J., and Pytkowicz, R. (1973). Measurement of the apparent dissociation constants of carbonic acid in seawater at atmospheric pressure. *Limnology and Oceanography*, pages 897–907.
- Metz, B., Davidson, O., De Coninck, H., Loos, M., and Meyer, L. (2005). IPCC special report on carbon dioxide capture and storage: Prepared by working group III of the intergovernmental panel on climate change. *IPCC, Cambridge University Press: Cambridge, United Kingdom and New York, USA*, 2.
- Meybodi, H. E. and Hassanzadeh, H. (2013). Stability analysis of two-phase buoyancy-driven flow in the presence of a capillary transition zone. *Physical Review E*, 87(3):033009.
- Meysami, B., Balaban, M. O., and Teixeira, A. A. (1992). Prediction of pH in model systems pressurized with carbon dioxide. *Biotechnology progress*, 8(2):149–154.
- Mitiku, A. B., Li, D., Bauer, S., and Beyer, C. (2013). Geochemical modelling of CO₂–water–rock interactions in a potential storage formation of the north german sedimentary basin. *Applied Geochemistry*, 36:168–186.
- Molins, S., Trebotich, D., Steefel, C. I., and Shen, C. (2012). An investigation of the effect of pore scale flow on average geochemical reaction rates using direct numerical simulation. *Water Resources Research*, 48(3).
- Moore, J. C., Battino, R., Rettich, T. R., Handa, Y. P., and Wilhelm, E. (1982). Partial molar volumes of gases at infinite dilution in water at 298.15 k. *Journal of Chemical and Engineering Data*, 27(1):22–24.
- Mucci, A. (1983). The solubility of calcite and aragonite in seawater at various salinities, temperatures, and one atmosphere total pressure. *American Journal of Science*, 283(7):780.
- Myint, P. C. and Firoozabadi, A. (2013). Onset of convection with fluid compressibility and interface movement. *Physics of Fluids (1994-present)*, 25(9):094105.
- Nesbitt, H. (1984). Calculation of the solubility of CO₂ in nacl-rich hydrothermal solutions using regular solution equations. *Chemical geology*, 43(3):319–330.

- Neufeld, J., Hesse, M., Riaz, A., Hallworth, M., Tchelepi, H., and Huppert, H. (2010). Convective dissolution of carbon dioxide in saline aquifers. *Geophysical Research Letters*, 37(22):L22404.
- Ngoc, T. T., Lefebvre, R., Konstantinovskaya, E., and Malo, M. (2014). Characterization of deep saline aquifers in the bécancour area, st. lawrence lowlands, québec, canada: implications for CO₂ geological storage. *Environmental Earth Sciences*, pages 1–28.
- Nielsen, A. E. (1964). *Kinetics of precipitation*. Pergamon Press;[distributed in the Western Hemisphere by Macmillan, New York].
- Nighswander, J., Kalogerakis, N., and Mehrotra, A. (1989). Solubilities of carbon dioxide in water and 1 wt. % sodium chloride solution at pressures up to 10 mpa and temperatures from 80 to 200. degree. c. *Journal of Chemical and Engineering Data*, 34(3):355–360.
- Noh, M. (2003). Reactive transport modeling in fractures and two-phase flow.
- Nomeli, M. A. and Riaz, A. (2014). Effect of CO₂ solubility on dissolution and precipitation rates of minerals in saline aquifers.
- Oelkers, E. H. and Cole, D. R. (2008). Carbon dioxide sequestration a solution to a global problem. *Elements*, 4(5):305–310.
- Oelkers, E. H. and Schott, J. (2005). Geochemical aspects of CO₂ sequestration. *Chemical Geology*, 217(3):183–186.
- Oelkers, E. H., Schott, J., and Devidal, J.-L. (1994). The effect of aluminum, pH, and chemical affinity on the rates of aluminosilicate dissolution reactions. *Geochimica et Cosmochimica Acta*, 58(9):2011–2024.
- Ohsumi, T., Nakashiki, N., Shitashima, K., and Hiramama, K. (1992). Density change of water due to dissolution of carbon dioxide and near-field behavior of CO₂ from a source on deep-sea floor. *Energy Conversion and Management*, 33(5-8):685–690.
- Orr, F. M. (2009). Onshore geologic storage of CO₂. *Science*, 325:1656–1658.
- Ozah, R. C., Lakshminarasimhan, S., Pope, G. A., Sepehrnoori, K., Bryant, S. L., et al. (2005). Numerical simulation of the storage of pure CO₂ and CO₂-H₂S gas mixtures in deep saline aquifers. In *SPE Annual Technical Conference and Exhibition*. Society of Petroleum Engineers.
- Palandri, J. (2004). A compilation of rate parameters of water-mineral interaction kinetics for application to geochemical modeling. Technical report, DTIC Document.
- Palandri, J. L. and Kharaka, Y. K. (2004). A compilation of rate parameters of water-mineral interaction kinetics for application to geochemical modeling. Technical report, DTIC Document.

- Pandit, S., Nayak, B., and Das, D. (2011). Microbial carbon capture cell using cyanobacteria for simultaneous power generation, carbon dioxide sequestration and wastewater treatment. *Bioresource Technology*.
- Panton, R. L. (2006). *Incompressible flow*. John Wiley & Sons.
- Parkhurst, D. L. (1995). User's guide to PHREEQC: A computer program for speciation, reaction-path, advective-transport, and inverse geochemical calculations.
- Parkinson, W. and De Nevers, N. (1969). Partial molal volume of carbon dioxide in water solutions. *Industrial & Engineering Chemistry Fundamentals*, 8(4):709–713.
- Patel, M. and Eubank, P. (1988). Experimental densities and derived thermodynamic properties for carbon dioxide-water mixtures. *Journal of Chemical and Engineering Data*, 33(2):185–193.
- Patel, M. R., Holste, J. C., Hall, K. R., and Eubank, P. T. (1987). Thermophysical properties of gaseous carbon dioxide-water mixtures. *Fluid phase equilibria*, 36:279–299.
- Pauling, L. (1988). *General chemistry*. Dover Pubns.
- Pechukas, P. (1981). Transition state theory. *Annual Review of Physical Chemistry*, 32(1):159–177.
- Pham, V., Lu, P., Aagaard, P., Zhu, C., and Hellevang, H. (2011). On the potential of CO₂-water-rock interactions for CO₂ storage using a modified kinetic model. *International Journal of Greenhouse Gas Control*, 5(4):1002–1015.
- Pineda, J. and Schwartz, S. (2006). Protein dynamics and catalysis: the problems of transition state theory and the subtlety of dynamic control. *Philosophical Transactions of the Royal Society B: Biological Sciences*, 361(1472):1433–1438.
- Pitzer, K. and Mayorga, G. (1973). Thermodynamics of electrolytes. II. activity and osmotic coefficients for strong electrolytes with one or both ions univalent. *The Journal of Physical Chemistry*, 77(19):2300–2308.
- Pitzer, K. S. (1991). *Activity coefficients in electrolyte solutions*. CRC press.
- Prigiobbe, V., Hänchen, M., Werner, M., Baciocchi, R., and Mazzotti, M. (2009). Mineral carbonation process for CO₂ sequestration. *Energy Procedia*, 1(1):4885–4890.
- Pruess, K. and García, J. (2002). Multiphase flow dynamics during CO₂ disposal into saline aquifers. *Environmental Geology*, 42(2):282–295.
- Pruess, K. and Spycher, N. (2007). ECO2N—A fluid property module for the TOUGH2 code for studies of CO₂ storage in saline aquifers. *Energy Conversion and Management*, 48(6):1761–1767.

- Prutton, C. and Savage, R. (1945). The solubility of carbon dioxide in calcium chloride-water solutions at 75, 100, 120 and high pressures¹. *Journal of the American Chemical Society*, 67(9):1550–1554.
- Quist, A. (1970). Ionization constant of water to 800. deg. and 4000 bars. *The Journal of Physical Chemistry*, 74(18):3396–3402.
- Rapaka, S., Chen, S., Pawar, R. J., Stauffer, P. H., and Zhang, D. (2008). Non-modal growth of perturbations in density-driven convection in porous media. *J. Fluid Mech.*, 609:285–303.
- Read, A. (1975). The first ionization constant of carbonic acid from 25 to 250° C and to 2000 bar. *Journal of Solution Chemistry*, 4(1):53–70.
- Reddy, M. and Gaillard, W. (1981). Kinetics of calcium carbonate (calcite)-seeded crystallization: Influence of solid/solution ratio on the reaction rate constant. *Journal of colloid and interface science*, 80(1):171–178.
- Riaz, A. and Cinar, Y. (2013). Carbon dioxide sequestration in saline formations: Part I - Review of solubility modeling studies. Under review. *Journal of Petroleum Science and Technology*.
- Riaz, A., Hesse, M., Tchelepi, H., and Orr, F. (2006). Onset of convection in a gravitationally unstable diffusive boundary layer in porous media. *Journal of Fluid Mechanics*, 548(1):87–111.
- Riaz, A. and Tchelepi, H. (2006). Numerical simulation of immiscible two-phase flow in porous media. *Physics of Fluids*, 18:014104.
- Rickard, D. and Sjöberg, E. (1983). Mixed kinetic control of calcite dissolution rates. *American Journal of Science*, 283(8):815–830.
- Rochelle, C., Pearce, J., and Holloway, S. (1999). The underground sequestration of carbon dioxide: containment by chemical reactions in the deep geosphere. *Geological Society, London, Special Publications*, 157(1):117–129.
- Rodriguez-Blanco, J. D., Shaw, S., and Benning, L. G. (2011). The kinetics and mechanisms of amorphous calcium carbonate (ACC) crystallization to calcite, via vaterite. *Nanoscale*, 3(1):265–271.
- Rogers, P. and Pitzer, K. (1982). Volumetric properties of aqueous sodium chloride solutions. *Journal of Physical and Chemical Reference Data*, 11:15.
- Rumpf, B., Nicolaisen, H., Öcal, C., and Maurer, G. (1994). Solubility of carbon dioxide in aqueous solutions of sodium chloride: Experimental results and correlation. *Journal of solution chemistry*, 23(3):431–448.
- Saadatpoor, E., Bryant, S. L., and Sepehrnoori, K. (2007). Effect of heterogeneity in capillary pressure on buoyancy driven flow of CO₂. In *DOE/NETL Sixth Annual Conference on Carbon Capture and Sequestration, Pittsburgh, PA*.

- Saldi, G. D., Schott, J., Pokrovsky, O. S., Gautier, Q., and Oelkers, E. H. (2012). An experimental study of magnesite precipitation rates at neutral to alkaline conditions and 100–200°C as a function of pH, aqueous solution composition and chemical affinity. *Geochimica et Cosmochimica Acta*, 83:93–109.
- Sass, R., Vidale, R., and Donohue, J. (1957). Interatomic distances and thermal anisotropy in sodium nitrate and calcite. *Acta Crystallographica*, 10(9):567–570.
- Schmidt, C. and Bodnar, R. (2000). Synthetic fluid inclusions: XVI. PVTX properties in the system H₂O-NaCl-CO₂ at elevated temperatures, pressures, and salinities. *Geochimica et Cosmochimica Acta*, 64(22):3853–3869.
- Schott, J., Pokrovsky, O. S., and Oelkers, E. H. (2009). The link between mineral dissolution/precipitation kinetics and solution chemistry. *Reviews in mineralogy and geochemistry*, 70(1):207–258.
- Seitz, J. and Blencoe, J. (1997). Experimental determination of the volumetric properties and solvus relations of H₂O–CO₂ mixtures at 300–400 C and 75–1000 bars. In *Proceedings of the Fifth International Symposium on Hydrothermal Reactions*, pages 109–112.
- Shaw, J., Bachu, S., et al. (2002). Screening, evaluation, and ranking of oil reservoirs suitable for CO₂ flood EOR and carbon dioxide sequestration. *Journal of Canadian Petroleum Technology*, 41(9):51–61.
- Shiraki, R., Rock, P., and Casey, W. (2000). Dissolution kinetics of calcite in 0.1 M NaCl solution at room temperature: An atomic force microscopic (afm) study. *Aquatic Geochemistry*, 6(1):87–108.
- Shogenova, A., Šliaupa, S., Shogenov, K., Šliaupiene, R., Pomeranceva, R., Vaher, R., Uibu, M., and Kuusik, R. (2009). Possibilities for geological storage and mineral trapping of industrial CO₂ emissions in the baltic region. *Energy Procedia*, 1(1):2753–2760.
- Sjöberg, E. (1978). *Kinetics and mechanism of calcite dissolution in aqueous solutions at low temperatures*. Almqvist & Wiksell.
- Smith, J. V. (1994). *Feldspars and Their Reactions*, 421(14).
- Smith, M., Campbell, D., Mackay, E., and Polson, D. (2011). CO₂ aquifer storage site evaluation and monitoring. *Heriot Watt University, Edinburgh, ISBN*, pages 978–0.
- Song, Y., Chen, B., Nishio, M., and Akai, M. (2005). The study on density change of carbon dioxide seawater solution at high pressure and low temperature. *Energy*, 30(11):2298–2307.

- Song, Y., Chen, B., and Shen, S. (2003a). Density and state function of CO₂ salt water solution in underground condition. *J. Therm. Sci. Technol.(China)*, 2(4):358–364.
- Song, Y., Nishio, M., Chen, B., Someya, S., and Ohsumi, T. (2003b). Measurement on CO₂ solution density by optical technology. *Journal of Visualization*, 6(1):41–51.
- Song, Y., Zhan, Y., Zhang, Y., Liu, S., Jian, W., Liu, Y., and Wang, D. (2013). Measurements of CO₂–H₂O–NaCl solution densities over a wide range of temperatures, pressures, and NaCl concentrations. *Journal of Chemical & Engineering Data*, 58(12):3342–3350.
- Sorai, M., Ohsumi, T., Ishikawa, M., and Tsukamoto, K. (2007). Feldspar dissolution rates measured using phase-shift interferometry: Implications to CO₂ underground sequestration. *Applied Geochemistry*, 22(12):2795–2809.
- Spycher, N. and Pruess, K. (2005). CO₂-H₂O mixtures in the geological sequestration of CO₂. II. partitioning in chloride brines at 12-100 C and up to 600 bar. *Geochimica et Cosmochimica Acta*, 69(13):3309–3320.
- Spycher, N. and Pruess, K. (2010a). The correcting factors are obtained from the private communication with Dr. Nicolas Spycher which is slightly different from his paper "a phase-partitioning model for CO₂-brine mixtures at elevated temperatures and pressures: Application to CO₂-enhanced geothermal systems". *Transport in porous media*, 82(1):173–196.
- Spycher, N. and Pruess, K. (2010b). A phase-partitioning model for CO₂-brine mixtures at elevated temperatures and pressures: Application to CO₂-enhanced geothermal systems. *Transport in porous media*, 82(1):173–196.
- Spycher, N., Pruess, K., and Ennis-King, J. (2003). CO₂-H₂O mixtures in the geological sequestration of CO₂. i. assessment and calculation of mutual solubilities from 12 to 100C and up to 600 bar. *Geochimica et cosmochimica acta*, 67(16):3015–3031.
- Steeffel, C., DePaolo, D., and Lichtner, P. (2005). Reactive transport modeling: An essential tool and a new research approach for the earth sciences. *Earth and Planetary Science Letters*, 240(3-4):539–558.
- Steeffel, C. I. and MacQuarrie, K. T. (1996). Approaches to modeling of reactive transport in porous media. *Reviews in Mineralogy and Geochemistry*, 34(1):85–129.
- Steeffel, C. I. and Maher, K. (2009). Fluid-rock interaction: A reactive transport approach. *Reviews in Mineralogy and Geochemistry*, 70(1):485–532.

- Sterner, S. M. and Bodnar, R. J. (1991). Synthetic fluid inclusions; X, experimental determination of PVTX properties in the CO₂ – H₂O system to 6 kb and 700 degrees C. *American Journal of Science*, 291(1):1–54.
- Stumm, W. (1970). *Aquatic Chemistry; An Introduction Emphasizing Chemical Equilibria in Natural Waters by Werner Stumm and James J. Morgan*. New York, Wiley-Interscience.
- Stumm, W. et al. (1992). *Chemistry of the solid-water interface: processes at the mineral-water and particle-water interface in natural systems*. John Wiley & Son Inc.
- Takenouchi, S. and Kennedy, G. (1965). The solubility of carbon dioxide in NaCl solutions at high temperatures and pressures. *American journal of science*, 263(5):445.
- Teng, H. and Yamasaki, A. (1998). Solubility of liquid CO₂ in synthetic sea water at temperatures from 278 K to 293 K and pressures from 6.44 MPa to 29.49 MPa, and densities of the corresponding aqueous solutions. *Journal of chemical & engineering data*, 43(1):2–5.
- Teng, H., Yamasaki, A., Chun, M., and Lee, H. (1997). Solubility of liquid CO₂ in water at temperatures from 278 K to 293 K and pressures from 6.44 MPa to 29.49 MPa and densities of the corresponding aqueous solutions. *The Journal of Chemical Thermodynamics*, 29(11):1301–1310.
- Commission of the European Communities (2007). Communication from the commission to the council, the european parliament, the european economic and social committee and the committee of the regions - limiting global climatic change to 2 degrees celcius: the way ahead for 2020 and beyond.
- Thomas, M. W., Stewart, M., Trotz, M., and Cunningham, J. A. (2012). Geochemical modeling of CO₂ sequestration in deep, saline, dolomitic-limestone aquifers: Critical evaluation of thermodynamic sub-models. *Chemical Geology*, 306:29–39.
- Tilton, N., Daniel, D., and Riaz, A. (2013). The initial transient period of gravitationally unstable diffusive boundary layers developing in porous media. *Physics of Fluids (1994-present)*, 25(9):092107.
- Tilton, N. and Riaz, A. (2014). Nonlinear stability of gravitationally unstable, transient, diffusive boundary layers in porous media. *Journal of Fluid Mechanics*, 745:251–278.
- Toews, K., Shroll, R., Wai, C., and Smart, N. (1995). pH-defining equilibrium between water and supercritical CO₂. influence on SFE of organics and metal chelates. *Analytical Chemistry*, 67(22):4040–4043.
- Truhlar, D. G., Garrett, B. C., and Klippenstein, S. J. (1996). Current status of transition-state theory. *The Journal of physical chemistry*, 100(31):12771–12800.

- Visconti, F., De Paz, J., and Rubio, J. (2010). Calcite and gypsum solubility products in water-saturated salt-affected soil samples at 25°C and at least up to 14 dS m⁻¹. *European Journal of Soil Science*, 61(2):255–270.
- Wagner, W. and Pruss, A. (2002). The iapws formulation 1995 for the thermodynamic properties of ordinary water substance for general and scientific use. *Journal of Physical and Chemical Reference Data*, 31(2):387–536.
- Weibel, R., Bateman, K., Laier, T., Nielsen, L., Frykman, P., Springer, N., et al. (2011). Geochemical impacts of CO₂ storage in saline aquifers with various mineralogy—results from laboratory experiments and reactive geochemical modelling. *Energy Procedia*, 4:4724–4731.
- Wigand, M., Carey, J., Schütt, H., Spangenberg, E., and Erzinger, J. (2008). Geochemical effects of CO₂ sequestration in sandstones under simulated in situ conditions of deep saline aquifers. *Applied Geochemistry*, 23(9):2735–2745.
- Wood, R., Majer, V., et al. (1996). Volumes of aqueous solutions of CH₄, CO₂, H₂S and NH₃ at temperatures from 298.15 K to 705 K and pressures to 35 MPa. *The Journal of Chemical Thermodynamics*, 28(2):125–142.
- Work, S. (2013). *A Study of Surface Treatments on Carbonate Core Material for Application to Mineral Precipitation and Dissolution during Geologic Carbon Storage*. PhD thesis, Doctoral Thesis, Rice University.
- Wormald, C., Lancaster, N., and Sellars, A. (1986). The excess molar enthalpies of $x\text{H}_2\text{O} + (1 - x)\text{CO}(\text{g})$ and $x\text{H}_2\text{O} + (1 - x)\text{CO}_2(\text{g})$ at high temperatures and pressures. *The Journal of Chemical Thermodynamics*, 18(2):135–147.
- Xu, T., Apps, J., and Pruess, K. (2001). Analysis of mineral trapping for CO₂ disposal in deep aquifers.
- Xu, T., Apps, J., and Pruess, K. (2002). Reactive geochemical transport simulation to study mineral trapping for CO₂ disposal in deep saline arenaceous aquifers.
- Xu, T., Apps, J., and Pruess, K. (2004). Numerical simulation of CO₂ disposal by mineral trapping in deep aquifers. *Applied geochemistry*, 19(6):917–936.
- Xu, T. and Pruess, K. (2001). Modeling multiphase non-isothermal fluid flow and reactive geochemical transport in variably saturated fractured rocks: 1. methodology. *American Journal of Science*, 301(1):16.
- Xu, T., Pruess, K., and Brimhall, G. (1999). An improved equilibrium-kinetics speciation algorithm for redox reactions in variably saturated subsurface flow systems. *Computers & Geosciences*, 25(6):655–666.
- Xu, T., Sonnenthal, E., Spycher, N., and Pruess, K. (2006). TOUGHREACT? A simulation program for non-isothermal multiphase reactive geochemical transport in variably saturated geologic media: Applications to geothermal injectivity and CO₂ geological sequestration. *Computers & Geosciences*, 32(2):145–165.

- Yan, W., Huang, S., and Stenby, E. H. (2011). Measurement and modeling of CO₂ solubility in NaCl brine and CO₂-saturated NaCl brine density. *International Journal of Greenhouse Gas Control*, 5(6):1460–1477.
- Yu, H., Shen, P., Shi, Y., Yang, Y., and Wang, J. (2011). Study on the safety geology sequestration after CO₂ displacement in low permeability oil reservoir. In *SPE Enhanced Oil Recovery Conference*.
- Zakirov, I. (1984). The PVT relations in the H₂O-CO₂ system at 300 and 400 C up to 1000 bar. *Geochem. Intl*, 21(6):13–20.
- Zhang, J., Zhang, X., Han, B., He, J., Liu, Z., and Yang, G. (2002). Study on intermolecular interactions in supercritical fluids by partial molar volume and isothermal compressibility. *The Journal of supercritical fluids*, 22(1):15–19.
- Zhang, W., Li, Y., Xu, T., Cheng, H., Zheng, Y., and Xiong, P. (2009). Long-term variations of CO₂ trapped in different mechanisms in deep saline formations: A case study of the songliao basin, china. *International journal of greenhouse gas control*, 3(2):161–180.
- Zhang, Y.-G. and Frantz, J. D. (1992). Hydrothermal reactions involving equilibrium between minerals and mixed volatiles: 2. investigations of fluid properties in the CO₂-CH₄-H₂O system using synthetic fluid inclusions. *Chemical geology*, 100(1):51–72.
- Zhu, H., Newton, R., and Kleppa, O. (1994). Enthalpy of formation of wollastonite (CaSiO₃) and anorthite (CaAl₂Si₂O₈) by experimental phase equilibrium measurements and high-temperature solution colorimetry. *American Mineralogist*, 79(1-2):134–144.
- Zhu, N., Song, Y., Zhang, Y., Liu, W., and Chang, F. (2011). Progress in measurement and model on solubility of CO₂ under geological sequestration conditions. *Environmental Science & Technology*, page 03.
- Zsakó, J. and Arz, H. (1974). Kinetic analysis of thermogravimetric data. *Journal of Thermal Analysis and Calorimetry*, 6(6):651–656.
- Zweigel, P., Arts, R., Lothe, A. E., and Lindeberg, E. B. (2004). Reservoir geology of the utsira formation at the first industrial-scale underground CO₂ storage site (sleipner area, north sea). *Geological Society, London, Special Publications*, 233(1):165–180.